#99

MODELING THE THERMAL PLUME IN THE MERRIMACK RIVER FROM THE MERRIMACK STATION DISCHARGE

ASA Project 2010-011

PREPARED FOR:
Public Service of New Hampshire
Bow, NH

PREPARED BY:
Deborah Crowley
Craig Swanson
Daniel Mendelsohn
Nicholas Cohn

DATE SUBMITTED
21 December 2010

Applied Science Associates, Inc.
55 Village Square Drive
South Kingstown, RI 02879 USA
phone: +1 401 789-6224
fax: +1 401 789-1932

ASA Offices:
São Paulo, Brazil
Shanghai, China
Gold Coast, Australia
Perth, Australia

www.asascience.com

EXECUTIVE SUMMARY

Merrimack Station, owned and operated by Public Service New Hampshire (PSNH), is a coal fired power plant that uses Merrimack River water to condense steam in the power generation process. During this process the river water absorbs heat and is discharged back in to the River at a higher temperature than upstream of the condenser. The use of River water in this manner results in a thermal plume created in the River from the Station discharge. The thermal plume is an ever changing volume of water which has elevated temperature. The magnitude and extent of the increased water temperature varies as a function of River flow, Station operations and meteorological conditions. In order to understand the characteristics of the plume PSNH contracted with Normandeau Associates Inc. (NAI) and Applied Science Associates, Inc. (ASA) to perform field and modeling studies, respectively.

The Station is located along the Hooksett Pool and is approximately 8 km (5 mi) long and runs from Garvins Falls Dam to the Hooksett Dam, receiving tributary inputs from the Soucook and Suncook tributaries both confluences located on the east side of the River. The River extends 45 km (28 mi) upstream of Garvins Falls where it is ultimately fed by regulated Lake Winnipesaukee discharges and groundwater discharge. All of the hydropower plants along the river are run-of-the-river that do not allow significant pooling of water.

The Station draws in between 5 – 15 m^3/s (180 – 530 cfs) of River water and after cooling the condensers discharges the heated water to a canal with anywhere from ~ 200 – 800 MWt (thermal) of rejected heat with maximum temperature rise of plant water typically less than 15°C (27°F). The heated water cools somewhat within the discharge canal. The level of cooling can be enhanced approximately 1-2°C (1.8 – 3.6°F) during critical time periods by use of the installed Power Spray Modules (PSMs) located within the canal.

The Station has historically monitored surface water temperatures for the non winter months at three different locations, one upstream of the intake, one within the discharge canal, and the other downstream of the Station. In addition a short term intensive monitoring program was conducted which included a network of fixed thermistor strings that monitored the top, middle and bottom water temperatures at west, center and east locations at various transects (stations) along the River. The stations included one just south of Garvins Falls Dam, one near the plant intake, one at the confluence of the discharge canal and the River, and three south of the canal along the River, including one just before the Hooksett Dam. These stations were located in an effort to provide information on the ambient conditions upstream, the conditions near the canal and the Pool south to the Hooksett Dam. An additional component of the monitoring program included four days of mobile observations which recorded River currents at transects corresponding to the fixed thermistor station locations. The observations were intended to provide insight as to the magnitude of River currents and their variability at these locations

The fixed instrumentation was deployed from early spring until fall in 2009. An analysis of this data showed that thermal plume was most often observed on the west side of the River close to the discharge canal as expected. In this area the observed elevated temperatures were primarily contained between the west and center of the River in the top to middle of the water column and not observed on the bottom. The most consistent location of observed thermal plume was at S0 West Top which was the surface thermistor located on the west side of the River at S0 which is adjacent to the discharge canal, however there were some episodes where the signal observed at S0 West Top was not significant. These episodes did not have any significant environmental or Station forcing that would cause these differences and therefore were concluded to have been caused by unknown forcing mechanisms. Similarly, there were episodes of relatively significant thermal plume response at S0 Center Top, S0 West Middle and S4 West Top, however their occurrence was not always consistent under similar conditions, again leading to the conclusion that there were some forcing mechanisms not completely understood or monitored. It was consistently observed however that the thermal plume was well mixed in both the vertical and lateral dimensions at stations S16 and A0.

The modeling study included the calibration and validation of a three dimensional hydrothermal model of the study area. The model was set up to reflect the physical characteristics of the domain including geometry, river bathymetry, and appropriate boundaries located where model forcing could be applied. The model forcing driving the circulation included river flow, water surface elevation, temperature and winds while solar radiation and auxiliary parameters, such as air and dew point temperature, relative humidity and pressure, as well as Station thermal discharge and flow properties play an important role in determining the thermal field.

The calibration and validation timeframes were selected for periods within the summer season as this is typically a time of most interest. During the summer there is less cooling capacity in the environment to absorb the heat from the thermal plume and therefore typically the largest plant impacts occur during summer months. The calibration and validation time periods were similar in that they both had low river flows, high water and air temperatures along with fairly consistent solar radiation. They differed mainly in that during the calibration time period only one boiler was operational and the overall heat rejection to the water was low where as during the validation timeframe both boilers were operational as sell as the PSMs for enhanced cooling.

The model was calibrated and validated successfully. The model was able to recreate the trend and general magnitude of observed currents. Furthermore the model was able to recreate the observed upstream water temperatures, forced only by the environmental meteorological condition as well as capture the strong signal of the thermal plume at station S0, in particular the strong signal at the top and weaker signal at the bottom. Additionally the model was able to simulate the observed vertically mixed plume well at locations south of S0 as well as the vertical structure of the water column which matched the observations in that on a regular basis there is little vertical variability in temperature with the exception of S0-West Top. The

model was able to simulate the enhanced cooling of the PSMs which was validated using historical temperature observations in the canal during both PSM on and off time periods. All of the guidance criteria for adequate model calibration and validation based on quantitative statistical measures were observed.

Subsequent to calibration and validation the model was used to simulate an extreme case scenario. The scenario time period was reflective of conditions that would result in the greatest impact of the Station, meaning a time where the combination of environmental (low river flow, high air and water temperatures) and Station forcing (maximum heat rejection of 800 MWt) were such that the River would see the highest increase in temperature. The scenario timeframe selected was 24 July through 3 August 2007. The scenario was run both with and without the plant thermal impacts, and then subsequently the results of these two cases were post processed to determine the temperature differential in these cases, thus isolating the temperature rise due to Station loading.

This set of runs and analysis showed that under this extreme condition the thermal plume behaves similarly in distribution as during the calibration and validation timeframes however that the overall temperature rise is much greater due to the high heat rejection and low thermal capacity of the environment. Temperature rise above background conditions due to the plant operation ranged from 7°C (12.6°F) at station S0 West down to approximately 2°C (3.6°F) of well mixed waters down at station A0, close to the Hooksett Dam. It should be noted that this process of isolating the temperature rise due to the plant was also applied to the validation timeframe, as it was a more stringent (higher heat refection) timeframe than the calibration time frame. The processing of those cases showed that again the trend of the location of the plume most significant at S0 West and the downstream vertically mixed plume was again achieved, however these summertime past conditions only resulted in a temperature rise of less than 1.5°C (2.7°F) at station A0, close to the Hooksett Dam.

TABLE OF CONTENTS

LIST OF FIGURES

LIST OF TABLES

1 INTRODUCTION

Merrimack Station (the Station) is a coal fired power plant owned and operated by Public Service New Hampshire (PSNH), a subsidiary of Northeast Utilities, which is the largest electric utility provider in the state of New Hampshire. The plant is located along the western side of the Merrimack River (the River) in Bow, New Hampshire as shown in Figure 1-1.

Merrimack Station has two generators which in combination have a capacity of 433 MWe (electrical); Unit 1 (MK1) is rated at 113 MWe and Unit 2 (MK2) is rated at 320 MWe. The plant takes in ambient River water which is used to condense steam in the power generation process. This heated water is subsequently discharged into a manmade canal which discharges to the River at a location downstream of the plant and intake structure. Furthermore the cooling canal has 56 sets of four power spray modules (PSMs) which provide enhanced cooling by pumping and spraying the water into the atmosphere above the canal; while the sprayed water falls back in to the canal, this operation provides increased heat exchange with the environment, meaning increased evaporative cooling.

In order to understand the thermal impacts on the River from the Station, in 2009 PSNH contracted with Normandeau Associates, Inc. (NAI) to carry out a field plan that monitored River water temperatures at various locations. PSNH subsequently contracted with Applied Science Associates, Inc. (ASA) to analyze the field data and use it to develop a hydrothermal model of the River which incorporated environmental and plant characteristics. ASA calibrated and validated the hydrothermal model to the 2009 field observations after which the model was used to simulate other plant and environmental conditions.

A description of the study area is presented in Section 2, the different data sources used in the study are described in Section 3, data analysis is summarized in Section 4, the hydrothermal model is presented in Section 5, the model application to the study area is described in Section 6, model calibration and validation are described in Section 7, a description of a scenario with a large, but realistic, thermal impact is outlined in Section 8 and the conclusions are provided in Section 9.

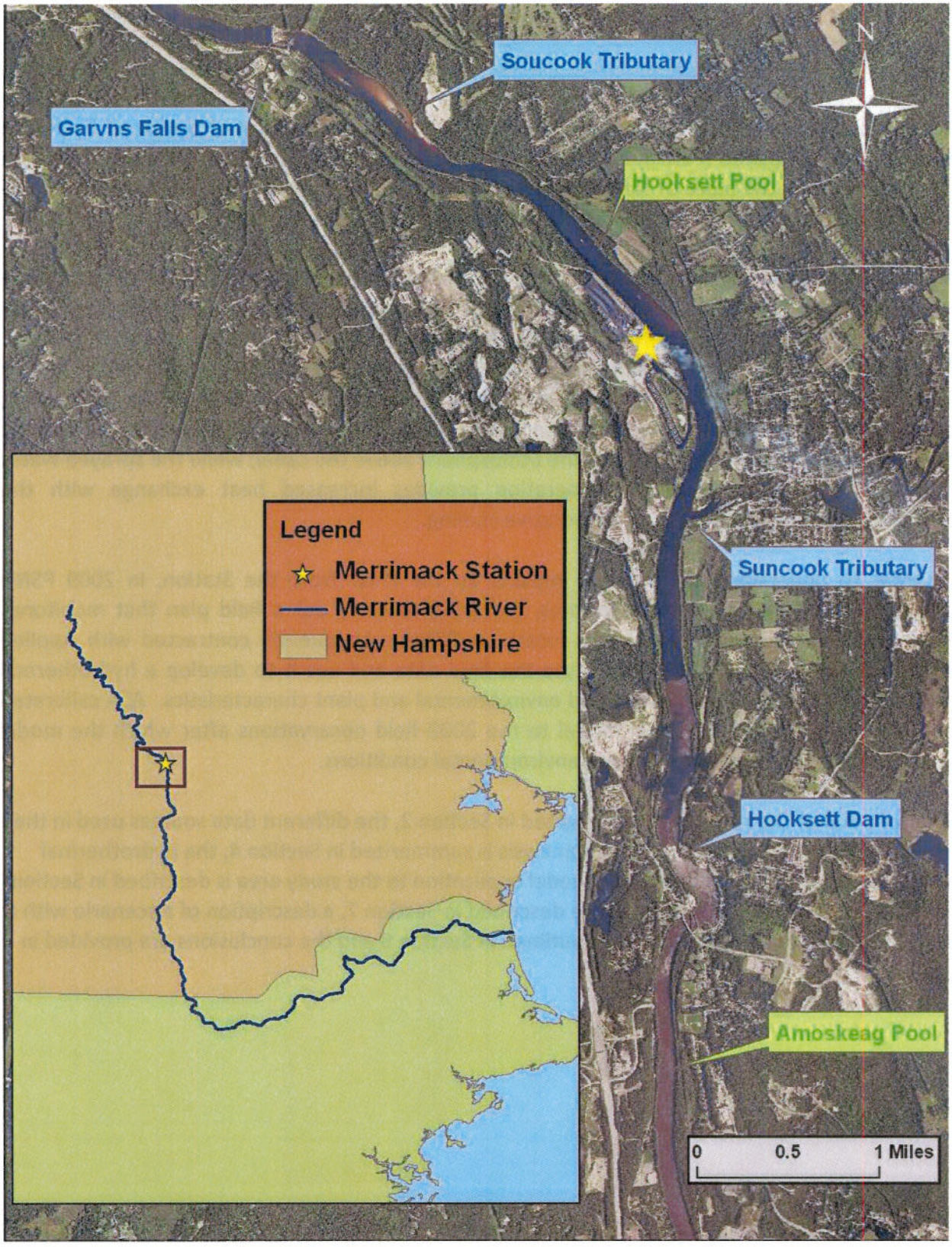

Figure 1-1. Merrimack River study area.

2 STUDY AREA

The Station is located along the River in Bow, New Hampshire. The River begins at the confluence of the Winnipesaukee River and the Pemigewasset River in Franklin, NH, approximately 48 km (30 mi) north of the Station and extends 177 km (110 mi) to its mouth in the Gulf of Maine. The River is relatively narrow, widths typically less than 150 m (490 ft), and shallow in most places with depths generally less than 4 m (13 ft). River flow is a function of groundwater discharge and outflow from Lake Winnipesaukee, which is regulated to have a minimum flow of approximately 7 m^3/s (250 cfs) however the flow can be greater when the goal is to lower lake levels in anticipation of flooding. There are multiple dams and hydroelectric power plants along the River, north and south of the Station. PSNH operates the Merrimack River Project in a Run of River mode by maintaining outflows from the three hydro developments that essentially equal the inflow to each development, meaning there is no significant ponding of water.

The Station is located on the Hooksett Pool (the Pool) which is the area of interest of the present modeling study. The Pool begins at the Garvins Falls Hydro Station and associated Garvins Falls Dam located approximately 4.8 km (3 mi) north of the plant, and ends at the Hooksett Hydro Station and associated Hooksett Dam located approximately 4 km (2.5 mi) south of the Station. Within the Pool, the River width ranges from 70 to 250 m (230 – 820 ft) and the River depths range from 0.8 to 4 m (2.6 to 13 ft). In 2009 pool elevations fluctuated between 0.3 to 1.7 m (1 to 5.6 ft) in response to River flow and station operations. Two tributaries enter the Pool, the Soucook located approximately 4 km (2.5 mi) upstream of the Station on the eastern shore and the Suncook, located approximately 1.1 km (0.7 mi) downstream of the Station on the eastern shore. Both tributary flow rates are a fraction of that at Garvins Falls Dam.

3 DATA SOURCES

Multiple data sources were used to assess the River and plant operations including fixed and mobile River observations as well as statistical estimates of River flow based on proxy station observations. Each of these data types will be described in detail in the sections below.

3.1 RIVER WATER ELEVATION

Observations of water elevations were recorded by PSNH at an hourly interval at the Hooksett Dam. Elevations were provided referenced to an elevation datum of 58.52 m (192 ft). During 2009 the Pool elevation ranged from 0.3 – 1.7 m (1 - 5.6 ft) above the reference datum.

3.2 USGS DATA

River flow estimates were based on relationships developed between flow at gauged U. S. Geological Survey's (USGS) stations and various other locations of interest per a recent watershed study (NAI, 2007). The developed relationship for Garvins Falls Dam, located approximately 5.6 km (3.5 mi) upstream from the plant, was used to estimate flow in the River near the Station.

The study are is also fed by the un-gauged Suncook River. The following method was used to estimate the Suncook discharge. The watershed study (NAI, 2007) related flow at different locations based on statistically developed relationships; the study utilized real time waterflow measurements at the Soucook (USGS 01089100) and Soughegan (USGS 01094000) gauges at a 15-minute interval to develop average hourly flow estimates. These flow estimates were then used for development of flow estimates at many different ungauged locations. The NAI analysis did not include the Suncook tributary, which is within the area of interest. There is a gauge, however, at the Suncook River (USGS 01089500). Using daily flows measured at the Suncook and Soucook, ASA developed a relationship between these stations that was used to make hourly estimates of flow at the Suncook based on hourly observations at the Soucook. Figure 3-1 illustrates the observed Suncook daily flow versus the NAI estimated Soucook flow and the trendline with corresponding relationship that best fits the data. This relationship was subsequently used to estimate hourly Suncook flow as a function of NAI estimated hourly Soucook flow.

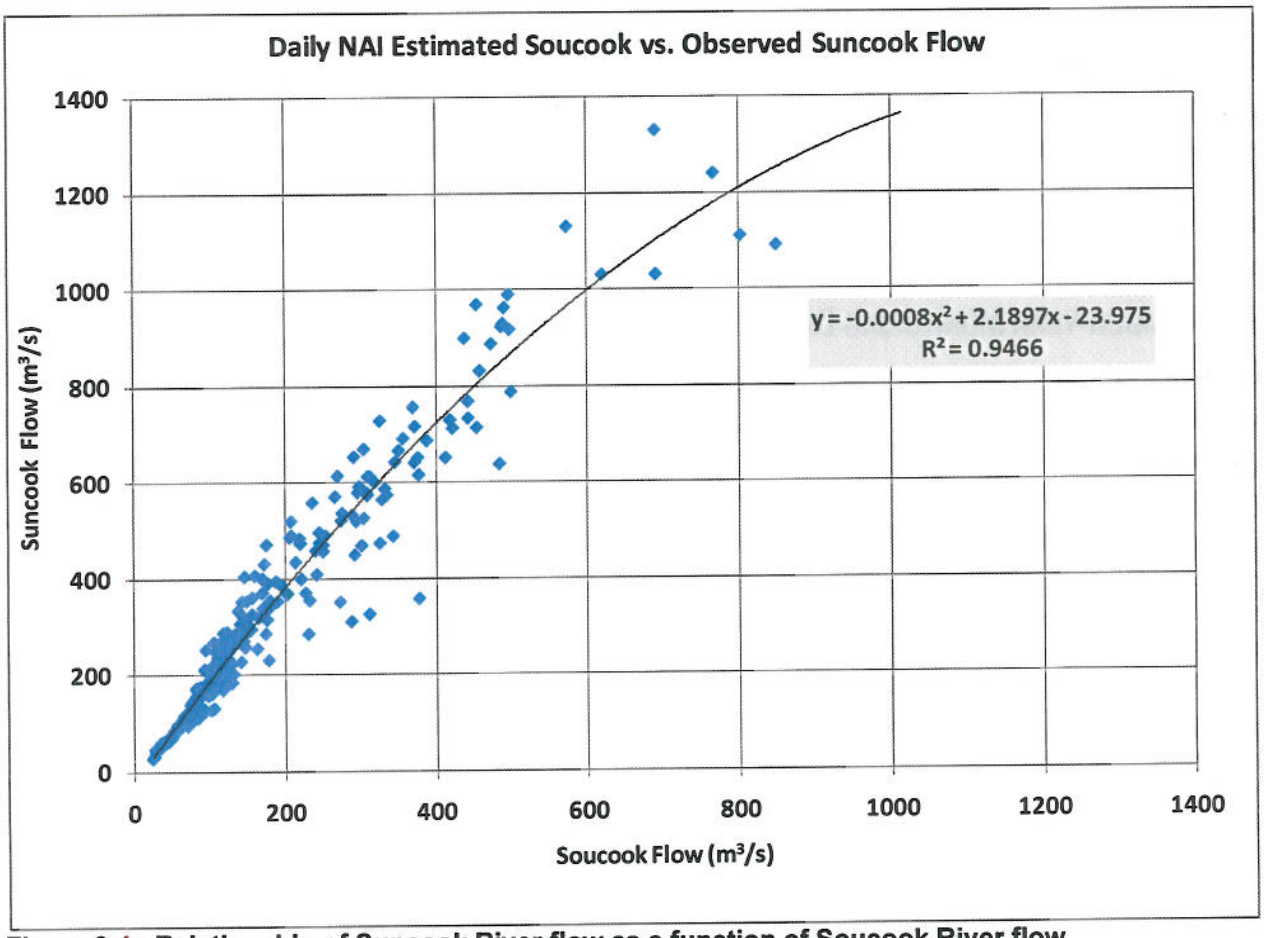

Figure 3-1. Relationship of Suncook River flow as a function of Soucook River flow.

3.3 NRCC/NWS DATA

The Northeast Regional Climate Center (NRCC) database includes historical climate data for the northeastern United States as well as continually updated National Weather Service (NWS) weather observations and forecasts. NRCC has also developed models that estimate variables such as solar radiation and evapotranspiration that are not typically observed. The closest NWS station to the study area is the Concord Airport (CON) located approximately 7.2 km (4.5 mi) north northeast of the Station at Lat 43°12'10.15", Long 71°30'9.61". A suite of meteorological observations are recorded including air temperature, dew point, wet bulb temperature, pressure, relative humidity, wind speed and direction and solar radiation. The airport location is shown in Figure 2-1.

3.4 HOOKSET POOL MONITORING PROGRAM

A long term monitoring program and an intensive short term River monitoring program were conducted in the River. The long term program is a multi-year program which monitors surface River temperatures at three different locations. The intensive short term program conducted in 2009 included the long term observation stations as well as additional observation stations

monitoring surface, middle and bottom River temperatures at quarter River width intervals for the period from April through November. In addition, during the short term monitoring program, River currents were measured on four different occasions at transects concurrent with the short term monitoring stations. Figure 3-2 illustrates the locations of both long and short term observations stations which will be described in more detail in the following sections.

3.4.1 Multi-year Monitoring Data

Multiyear water surface temperature data was available for use in this study at three different locations, N10 Historical (N10H), S0 Historical (S0H) and S4 Historical (S4H). These stations are located as shown in Figure 3-2. The record provided for this study for each of these stations covers a period from late March/early April 2002 through 2010; however these stations continue to record data. The temporal resolution of this data is fifteen minutes. N10H represents the upstream ambient temperatures, S0H represents the canal discharge temperatures and S4H represents the downstream plume temperatures. Table 3-1 summarizes the coordinates of these historical stations.

Table 3-1. Historical station summary.

Station	Latitude	Longitude	Depth
N10H	43 09.123 N	71 28.782 W	0.3 m (1 ft)
S0H	43 08.156 N	71 27.842 W	0.3 m (1 ft)
S4H	43 07.851 N	71 27.818 W	0.3 m (1 ft)

3.4.2 2009 Monitoring Data

As described above an intensive River monitoring program was carried out in 2009. This program consisted of an eight-month fixed River water temperature monitoring program at multiple locations as well as mobile survey observations of River flow at multiple transects on four different days.

3.4.2.1 Moored Thermistor Array

The fixed River temperature observations from 2009 were obtained from moored thermistors located in the Pool at various locations. These stations were located on cross River (¼ across [West], ½ across [Center] and ¾ across [East]) transects and were equipped to monitor top, middle and bottom water column temperatures. Five transects (N10, N5, S0, S4, S16) were deployed, spanning the Hooksett Pool, and one additional location (A0) monitoring only middle and bottom water column temperatures at the River center close to the Hooksett Dam. For each station the top measurement was approximately 0.3 m (1 ft) below the surface, the middle is the middle of the water column and the bottom measurement was approximately 0.3 m (1 ft) above the bottom. Figure 3-2 illustrates the locations of these observation stations.

The specific period of record varied for each station however a complete synoptic set of observations was available from May 10, 2009 through October 27, 2009. Table 3-2 summarizes the period of record for each station. All stations recorded River temperatures at 15-minute intervals.

Table 3-2. 2009 Monitoring station summary.

Station	Location Description	Latitude	Longitude	Begin	End
N10	Center	43.15163	-71.47864	5/5/2009	10/27/2009
N10	East	43.15185	-71.47824	5/5/2009	10/27/2009
N10	West	43.15141	-71.47905	5/5/2009	10/27/2009
N5	Center	43.14270	-71.46701	5/5/2009	10/27/2009
N5	East	43.14299	-71.46649	5/5/2009	10/27/2009
N5	West	43.14242	-71.46752	5/5/2009	10/27/2009
S0	Center	43.13631	-71.46258	5/5/2009	10/27/2009
S0	East	43.13641	-71.46210	5/5/2009	10/27/2009
S0	West	43.13622	-71.46302	5/5/2009	10/27/2009
S16	Center	43.11355	-71.46521	5/4/2009	11/4/2009
S16	East	43.11357	-71.46454	5/4/2009	11/4/2009
S16	West	43.11352	-71.46590	5/4/2009	11/4/2009
S4	Center	43.13070	-71.46358	5/4/2009	10/28/2009
S4	East	43.13062	-71.46323	5/4/2009	10/28/2009
S4	West	43.13078	-71.46392	5/4/2009	10/28/2009
A0	Center	43.10080	-71.46480	5/10/2009	11/6/2009

3.4.2.2 TRANSECTS

In addition to the moored thermistors, the 2009 short term one day intensive River monitoring program included four days (1 July, 6 August, 9 September, 12 October) of mobile surveys. On each day cross sectional profiles of River currents, using a boat mounted Acoustic Doppler Current Profiler (ADCP), were obtained at transects corresponding to each of the moored equipment locations (N10, N5, S0, S4 & S16). The relevant data obtained through these surveys were River speed and direction observations at various depths in the water column across the River. Each transect took less than ten minutes to transverse and all five were typically completed in less than three hours. Given that the River flow does not typically vary significantly during a dry day, the small differences in time can be considered synoptic to give an indication of how the River velocities vary spatially for a given River flow.

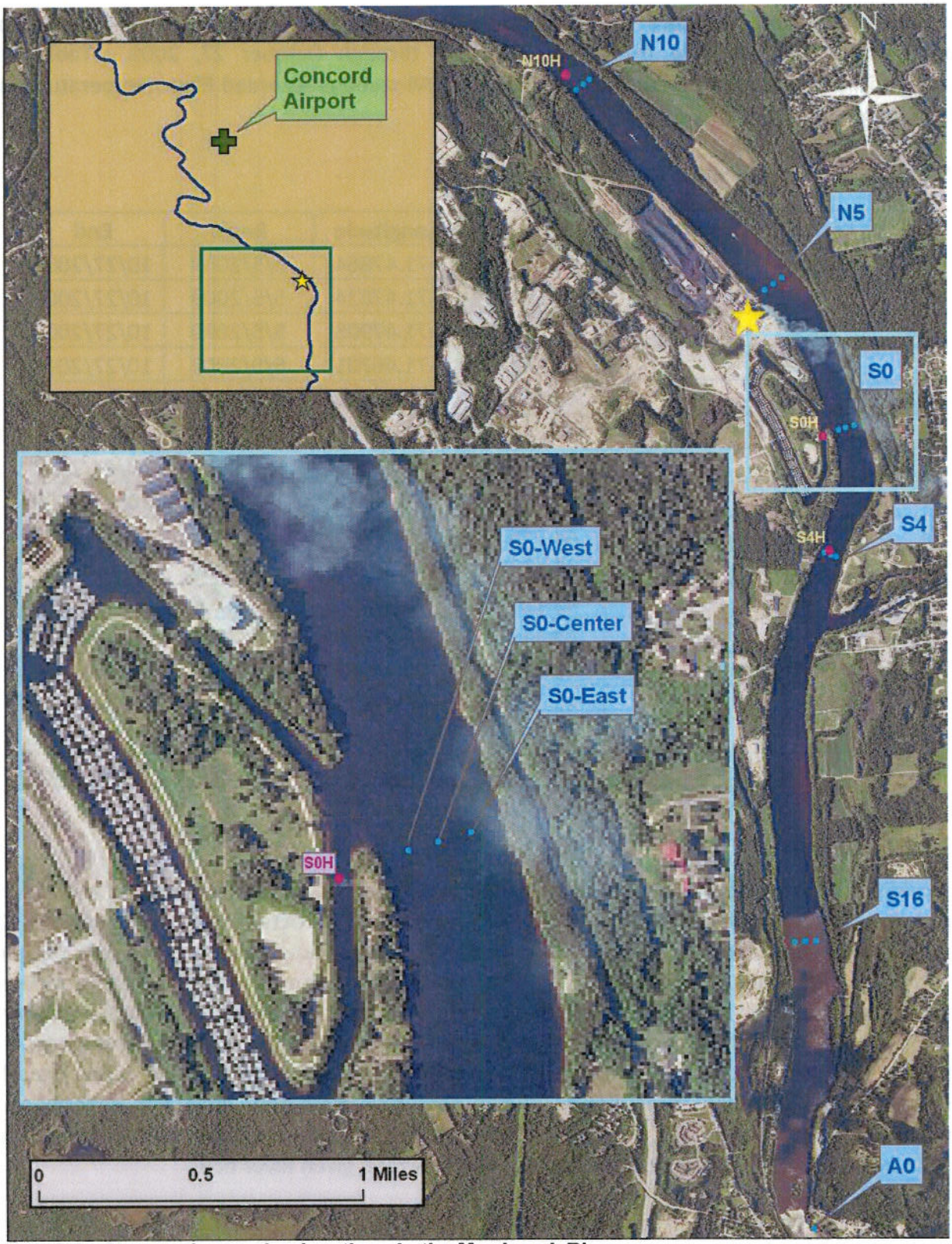

Figure 3-2. Observation station locations in the Merrimack River.

4 DATA ANALYSIS

Data analysis was performed as a preliminary step in this study to assess the extent of the thermal plume from the Station. River flow, meteorological observations and River temperature observations were analyzed.

4.1 RIVER ELEVATION AND FLOW

River elevations were observed as described in Section 3.1 and River flow in the study area was developed as described in Section 3.2. The 2009 record of Hooksett Pool elevations and estimated flow over the Hooksett Dam were plotted as shown in Figure 4-1. This plot shows that River flow and pool elevation follow the same pattern. For the months of January through September of 2009 the flow ranged between 50 – 750 m^3/s (1,750 – 26,500 cfs) and the pool elevation ranged from approximately 0.3 to 1.7 m (1 to 5.6 ft).

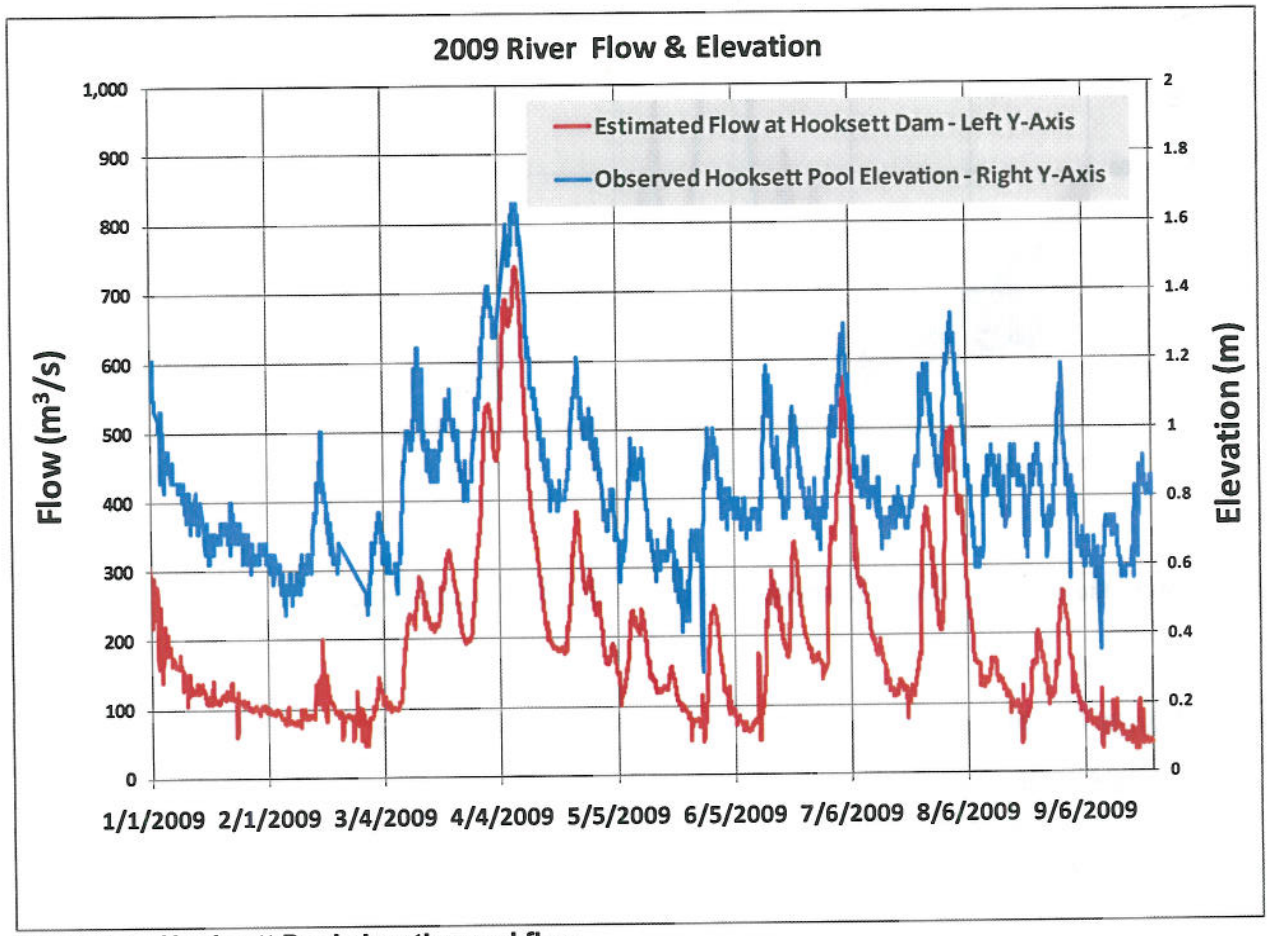

Figure 4-1. Hooksett Pool elevation and flow.

The 2009 estimated or observed flow at the different points in the study area are shown in Figure 4-2. This plot shows that the flow in the Pool ranges from 50 – 750 m^3/s (1,750 – 26,500 cfs). The Soucook and Suncook tributaries have relatively low flow compared to the main River flow, which is evident in the small increase in flow between Garvins Falls and the Hooksett Dam.

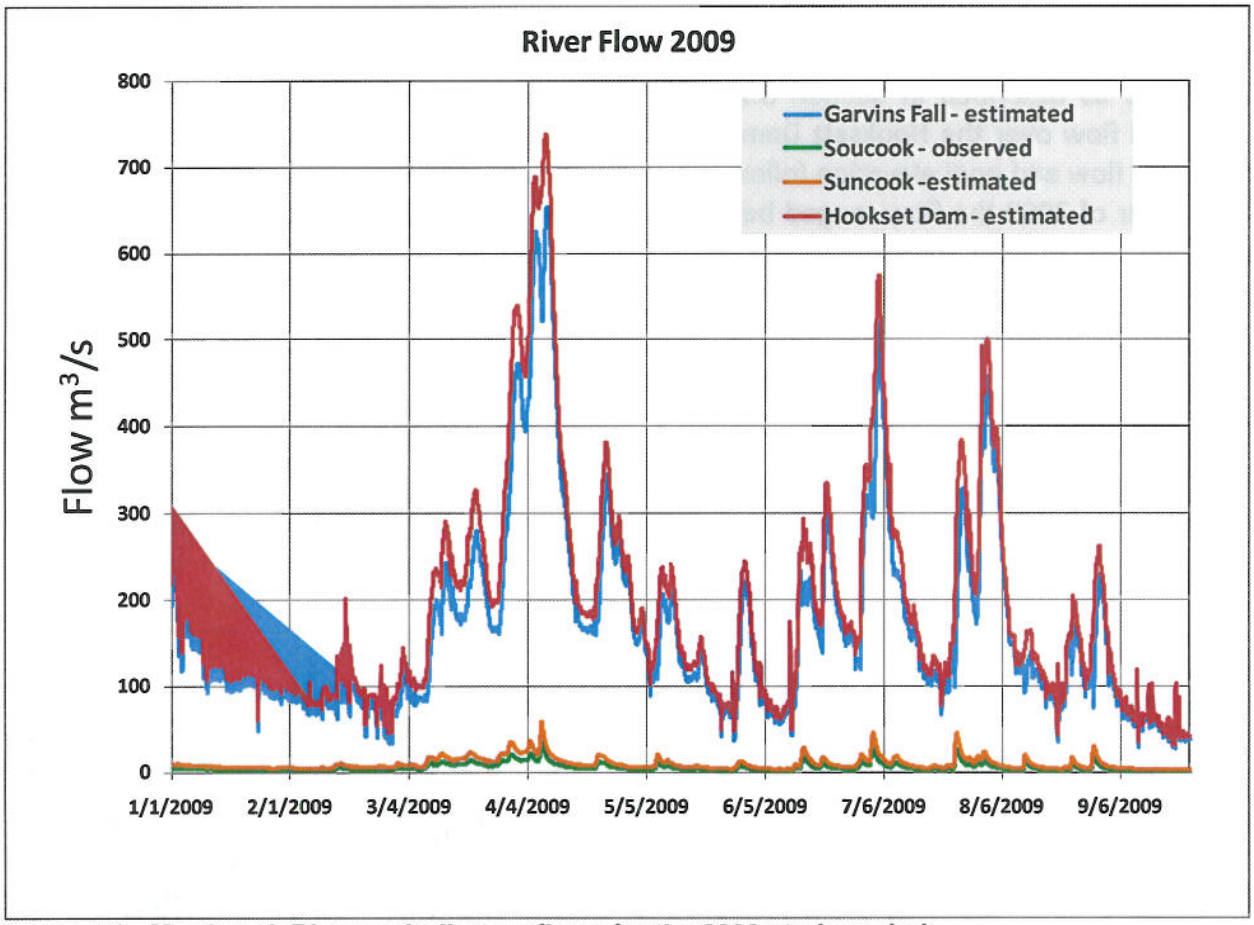

Figure 4-2. Merrimack River and tributary flows for the 2009 study period.

4.2 River Temperatures

As described in the previous sections there are both long term and short term monitoring programs that gathered water temperature observations. The locations of the long term monitoring stations and short term monitoring stations are as shown in Figure 3-2. Table 4-1 summarizes the position of each of these stations with respect to Garvins Falls Dam as well as the Station. Furthermore Table 4-1 summarizes the River width at each of these stations. Note that historical stations and short term stations with the same name (minus the H suffix on the short term stations) are in the same approximate location however station S0H is within the Stations discharge canal while station S0 is in the River and observations indicate that the water

has mixed with cooler River water, thus S0 is always cooler than S0H. Figure 4-3 through Figure 4-8 show the top, middle and bottom water temperatures at the west, center, and east locations of N10, N5, S0, S4, S16 and A0, respectively.

These plots show that the water column north of the plant, at stations N10 and N5, is vertically mixed as evident in negligible temperature differentials among the top, middle and bottom observations. There are multiple shallows, rapids and dams or spillways upstream of the observation station which would promote vertical mixing in the water column. S0 is the next transect south of N5, and is also within close proximity of the confluence of the Station discharge canal and the River. This transect shows a significant response in S0-West Top station, which is the westernmost surface thermistor in the S0 transect, clearly due the thermal effluent from the canal. While the signal at S0-West Top can be seen to respond to the plant thermal forcing, the response is not entirely consistent with the Station effluent record indicating that the thermal plume in the River is sometimes, but not always, wide enough to be observed at SO-West. The plume is occasionally wide enough however, to be observed at not only SO-Center Top but also at S0-East Top, and therefore covers practically the entire River width.

Further south downstream at station S4 the response to the Station discharge is further attenuated and only observed on an episodic basis. Transect S4 west, center and east surface station locations are observed to be slightly higher than the middle or bottom water temperatures at times, however at other times the water column appears to be vertically mixed. Further south downstream at both stations S16 and A0 the water column is fully vertically mixed with no discernable difference in temperature at different depths.

Table 4-1. Station position locations.

Station	Distance South of Garvins Falls	Distance from the Station	Direction From Merrimack Station	Width of River at Station
	m	m	m	m
N10	2,900	775	North	150
N5	4,300	2200	North	190
S0	5,100	0	-	130
S4	5,800	680	South	124
S16	7,800	2700	South	230
A0	9,300	4200	South	134

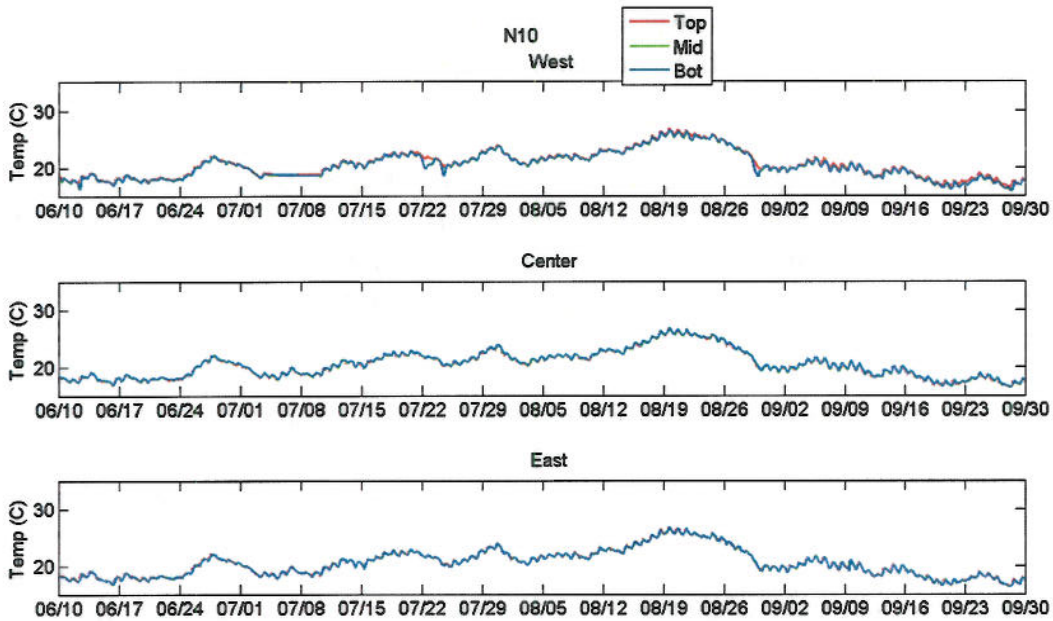

Figure 4-3. Observed temperatures at N10.

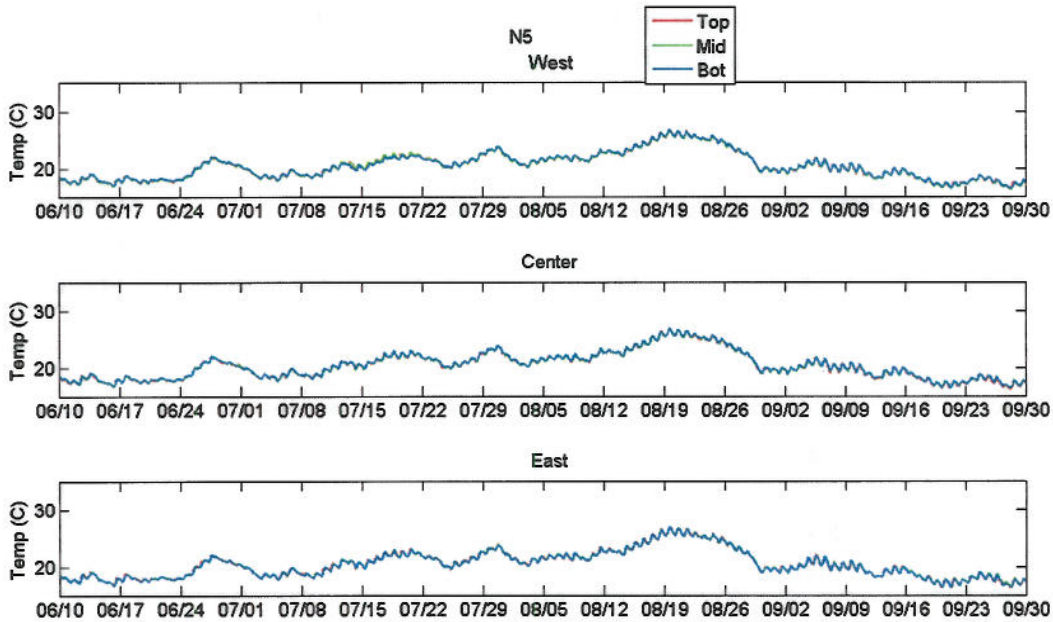

Figure 4-4. Observed temperatures at N5.

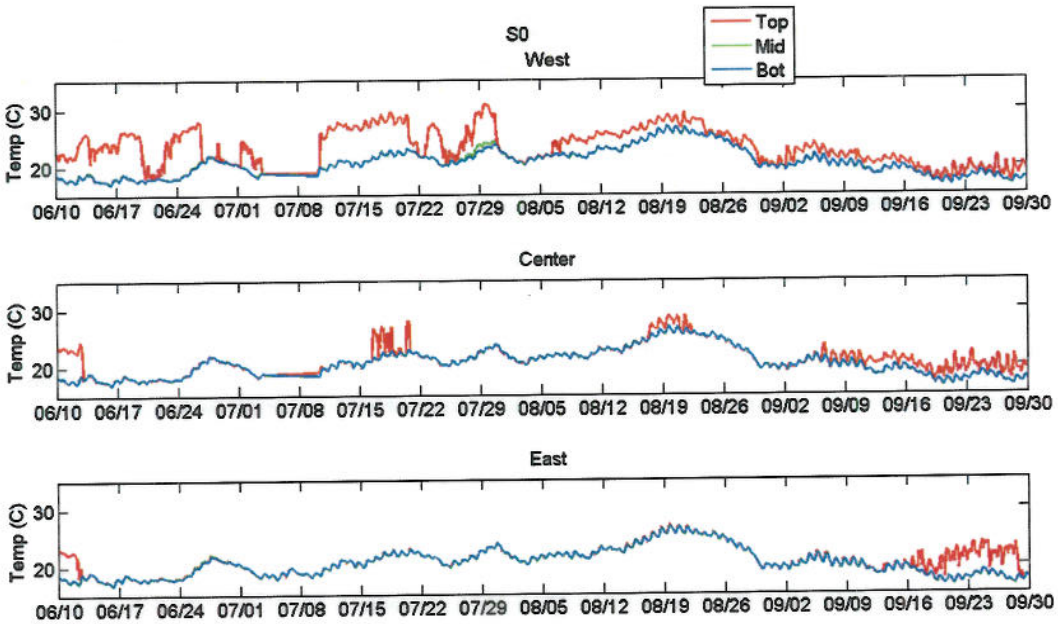

Figure 4-5. Observed temperatures at S0.

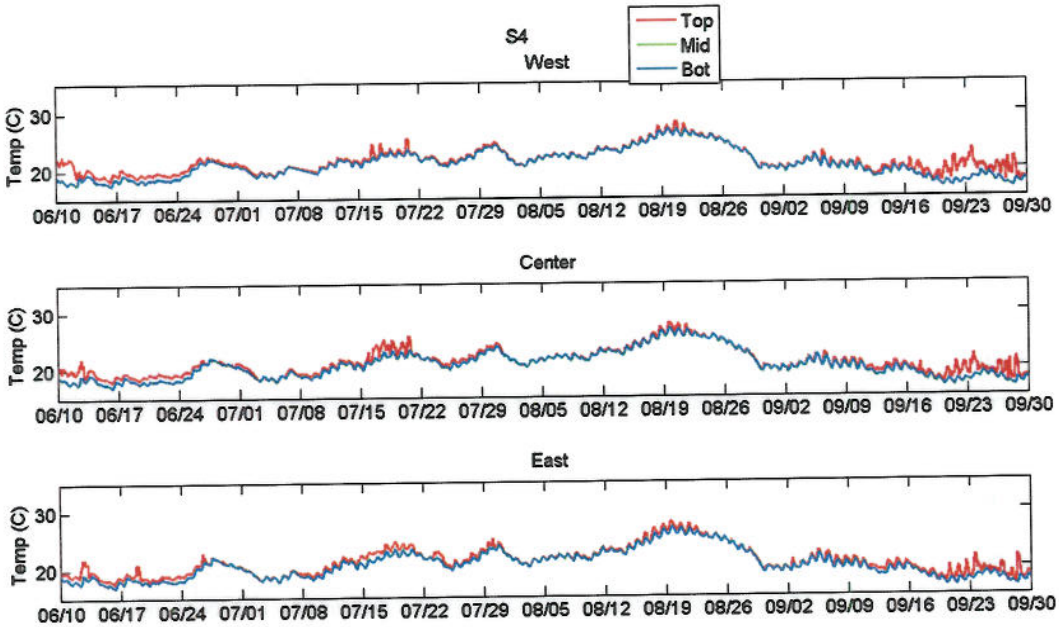

Figure 4-6. Observed temperatures at S4.

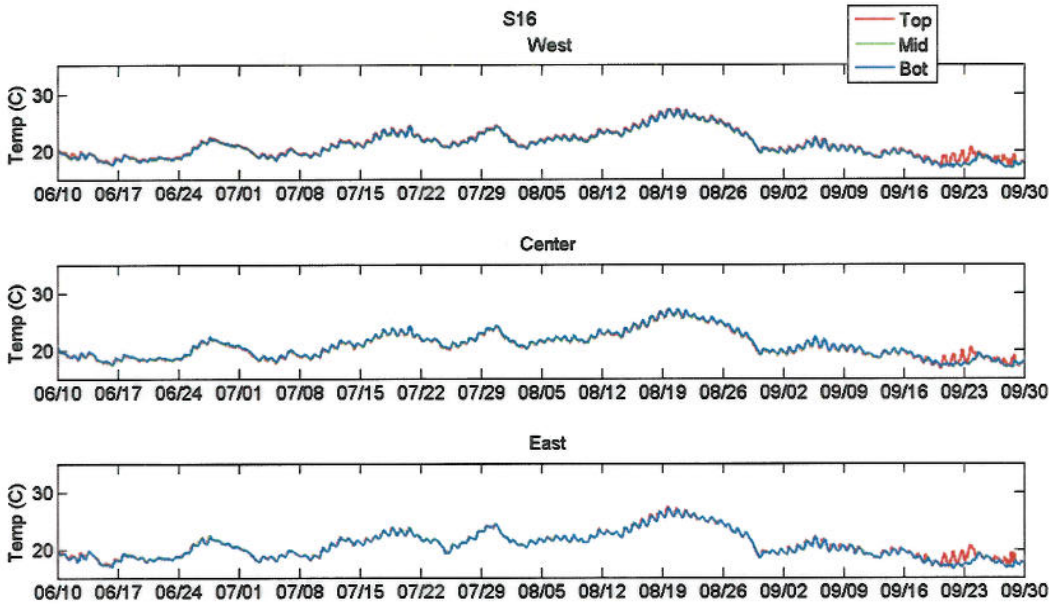

Figure 4-7. Observed temperatures at S16.

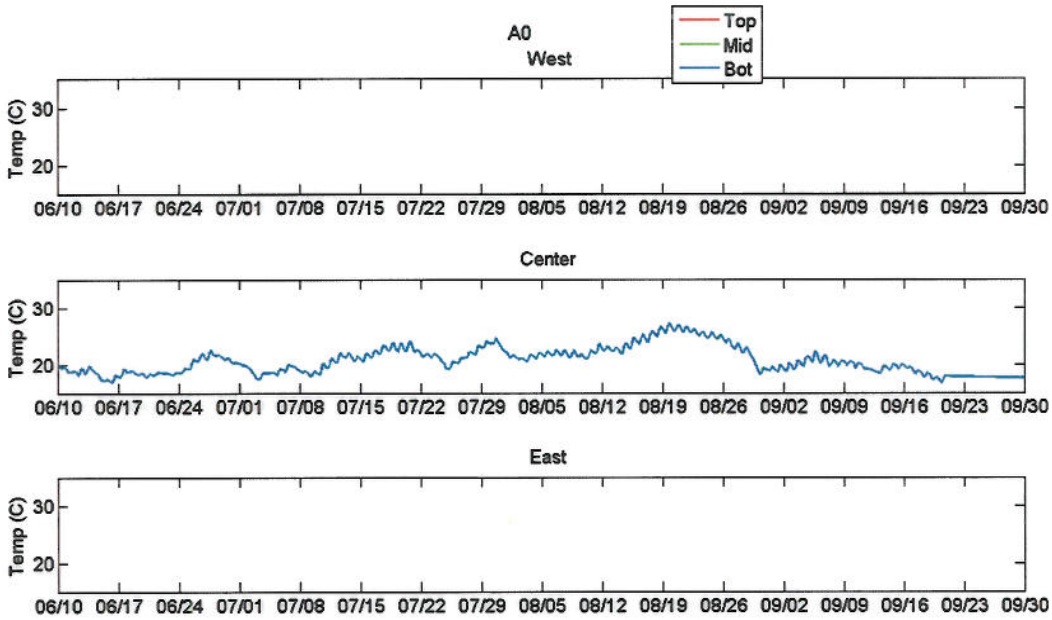

Figure 4-8. Observed temperatures at A0.

4.3 TRANSECTS

The 2009 ADCP transect data was acquired on 1 July, 6 August, 9 September, 12 October along each of the moored instrument transects. As an example of the flow distribution in the River, Figure 4-9 through Figure 4-13 show the contours of the observed River speeds on 6 August 2009 at each of the transects, respectively. On this day the River flow ranged from 215 - 270 m^3/s (7,600 – 9,500 cfs) in the Pool and correspondingly the River velocities observed ranged from 0.3 to 0.7 m/s (0.98 – 2.3 ft/s) in most areas with some smaller areas of lower velocity observed near the bottom and River banks. At transect S0 (Figure 4-11) it can be seen that the velocities on the western shore close to the canal discharge are relatively low from 0.2 – 0.4 m/s (0.65 – 1.3 ft/s) as compared to those closer to the eastern shore which range from 0.5 – 0.6 m/s (1.6 – 1.9 ft/s).

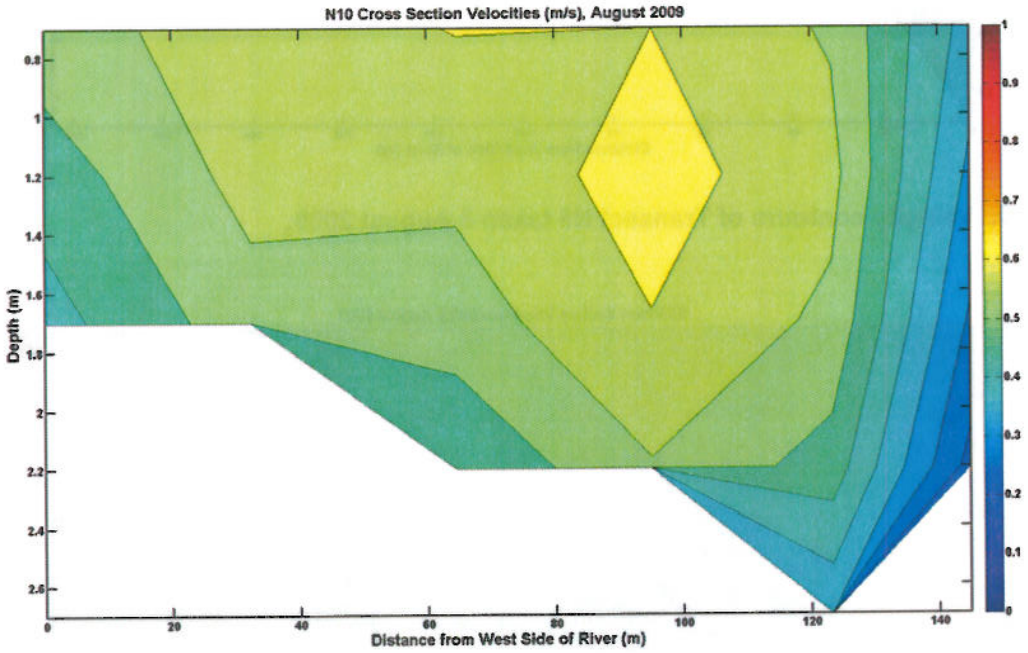

Figure 4-9. Velocity contours of Transect N10 taken 6 August 2009.

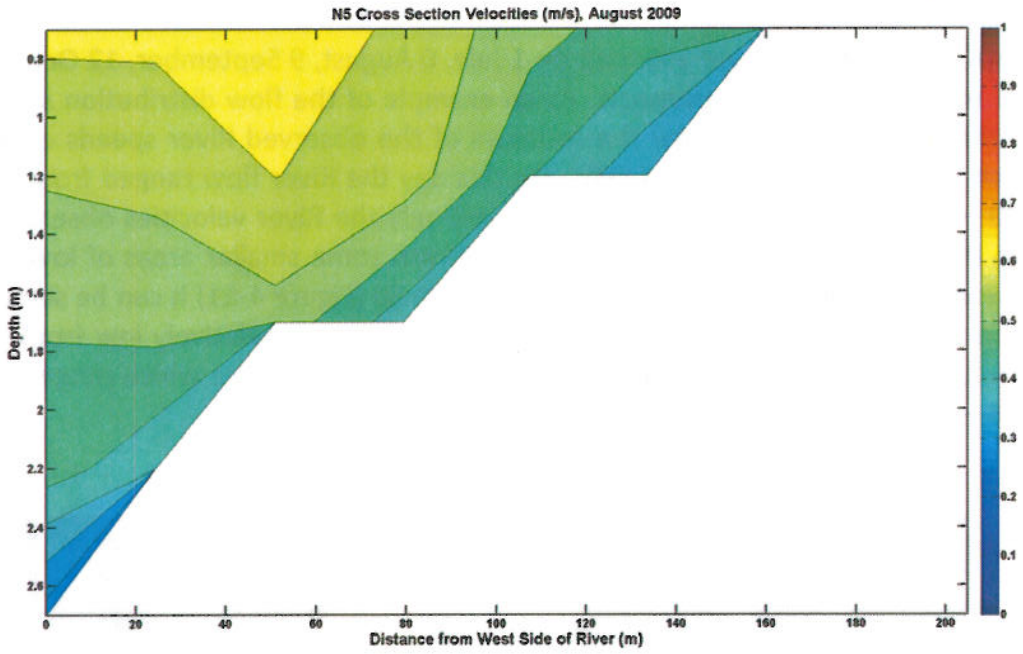

Figure 4-10. Velocity contours of Transect N5 taken 6 August 2009.

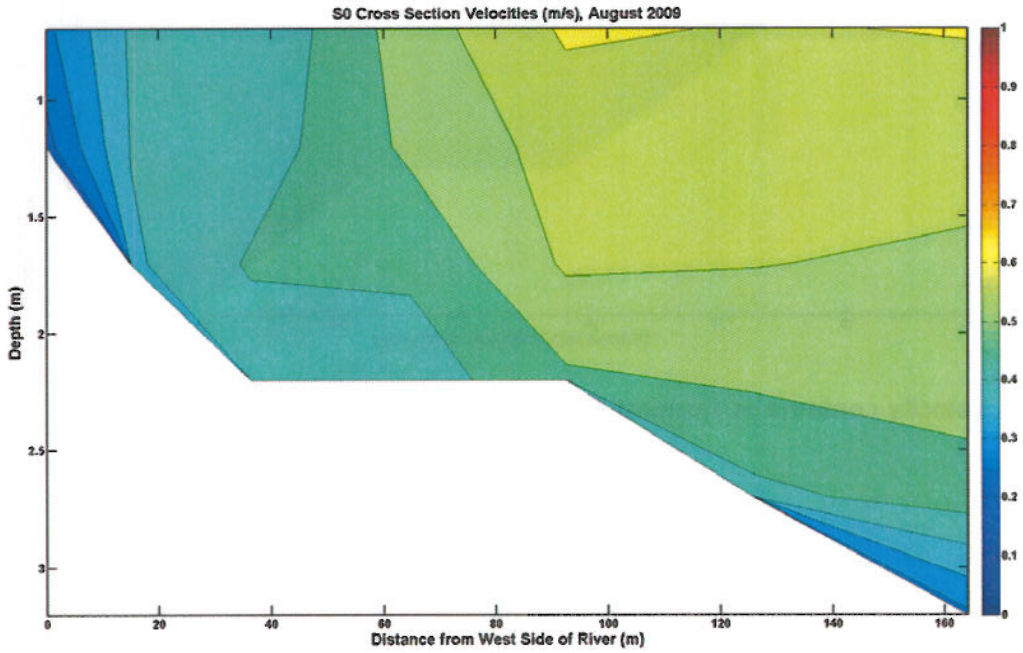

Figure 4-11. Velocity contours of Transect S0 taken 6 August 2009.

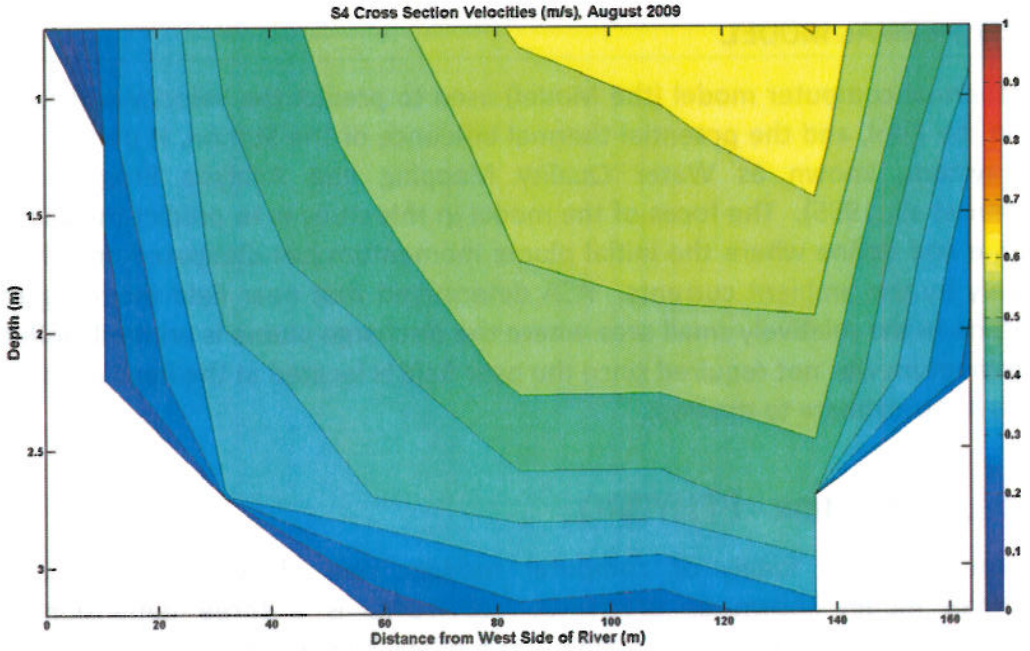

Figure 4-12. Velocity contours of Transect S4 taken 6 August 2009.

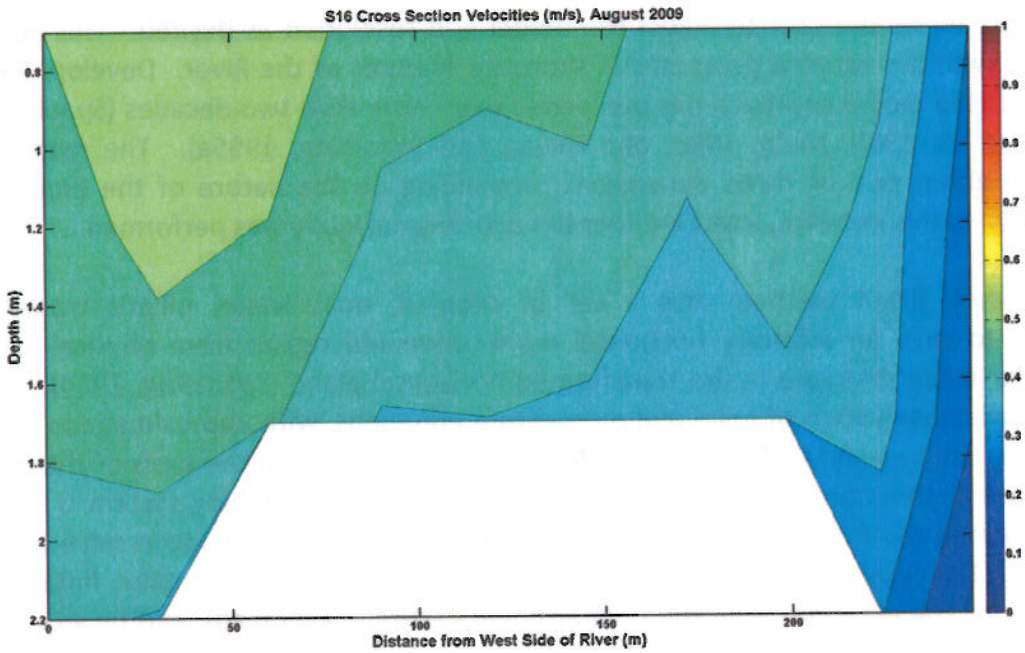

Figure 4-13. Velocity contours of Transect S16 taken 6 August 2009.

5 HYDROTHERMAL MODEL

The hydrothermal computer model (the Model) used to predict the velocity and temperature structure in the Pool, and the potential thermal influence of the Station, is part of a PC-based modeling system, known as Water Quality Mapping and Analysis Program (WQMAP) (Mendelsohn et al., 1995). The focus of the model in this study is to predict the spatial extent of the plume and define where the initial plume momentum has dissipated and the plume is affected only by the ambient currents. ASA determined that near field modeling to predict plume dilution in the relatively small area where the discharge plume is primarily influenced by its own momentum was not required since the near field is located at the head of the discharge canal and is not proximate to the Pool.

5.1 MODEL DESCRIPTION – BFHYDRO

WQMAP consists of a family of computer models, one of which is a hydrodynamic (hydrothermal) model known as BFHYDRO. BFHYDRO is a three dimensional, general curvilinear coordinate, boundary-fitted computer model (Muin and Spaulding, 1997; Huang and Spaulding, 1995b; Swanson et al, 1989) and was used to predict elevations, velocities, salinities and temperatures in the River. The boundary-fitted model matches the model coordinates with the shoreline boundaries of the water body, accurately representing the study area. This system also allows the user to adjust the model grid resolution as desired. This approach is consistent with the variable geometry of shoreline features of the River. Development of the boundary fitted model approach has proceeded over more than two decades (Spaulding, 1984; Swanson et al., 1989; Muin, 1993; and Huang and Spaulding, 1995a). The model may be applied in either two or three dimensions, depending on the nature of the inquiry and its complexity. In this instance, a three-dimensional or triaxial study was performed.

The boundary fitted method uses a set of coupled, quasi-linear, elliptic transformation equations to map an arbitrary horizontal multi-connected region from physical space to a rectangular mesh structure in the transformed horizontal plane (Spaulding, 1984). The three dimensional conservation of mass and momentum equations, with approximations suitable for lakes, rivers, and estuaries (Swanson, 1986; Muin, 1993) that form the basis of the model, are then solved in this transformed space. In addition a sigma stretching system is used in the vertical to map the free surface and bottom onto coordinate surfaces to resolve bathymetric variations. The resulting equations are solved using an efficient semi-implicit finite difference algorithm for the exterior mode (two dimensional vertically averaged), and by an explicit finite difference leveled algorithm for the vertical structure of the interior mode (three dimensional) (Swanson, 1986). The velocities are represented in their contra-variant form.

A detailed description of the model, with associated test cases, is included as Appendix A (Muin and Spaulding, 1997). The publication was originally part of a Ph.D. dissertation (Muin, 1993), which extended the boundary fitted model capabilities developed by Swanson (1986), applying

a contra-variant velocity formulation to the transformed momentum equations. A brief description of the model follows.

The basic equations are written in spherical coordinates to allow for accurate representation of large modeled areas. The conservation equations for water mass, momentum (in three dimensions) and constituent mass (temperature [heat] and salinity) form the basis of the model, and are well established. It is assumed that the flow is incompressible, that the fluid is in hydrostatic balance, the horizontal friction is not significant and the Boussinesq approximation applies all customary assumptions.

The boundary conditions are as follows:

- At land, the normal component of velocity is zero.
- At open boundaries, the free surface elevation must be specified, and temperature (and salinity for estuarine and coastal applications) specified on inflow.
- On outflow, temperature (heat) (and salinity) is advected out of the model domain.
- A bottom stress or a no slip condition is applied at the bottom. No temperature (heat) is assumed to transfer to or from the bottom, a conservative assumption as some transfer of shear to the bottom is expected to occur.
- A wind stress, and appropriate heat transfer terms, are applied at the surface.
- The surface heat balance includes all of the primary heat transfer mechanisms for environmental interaction.

There are various options for specification of vertical eddy viscosity, Av, (for momentum) and vertical eddy diffusivity, Dv, (for constituent mass [temperature and salinity]). The simplest formulation is that both are constant, Avo and Dvo, throughout the water column. They can also be functions of the local Richardson number, which, in turn, is a function of the vertical density gradient and vertical gradient of horizontal velocity. This application used spatially variant constant eddy viscosity and eddy diffusivity, where large upstream values were chosen to represent the turbulent waters and enhanced mixing through multiple dams.

The set of governing equations with dependent and independent variables transformed from spherical to curvilinear coordinates, in concert with the boundary conditions, is solved by a semi-implicit, split mode finite difference procedure (Swanson, 1986). The equations of motion are vertically integrated and, through simple algebraic manipulation, are recast in terms of a single Helmholtz equation in surface elevation. This equation is solved using a sparse matrix solution technique to predict the spatial distribution of surface elevation for each grid.

The vertically averaged velocity is then determined explicitly using the momentum equation. This step constitutes the external or vertically averaged mode. Deviations of the velocity field from this vertically averaged value are then calculated, using a tridiagonal matrix technique. The deviations are added to the vertically averaged values to obtain the vertical profile of velocity at each grid cell thereby generating the complete current patterns. This constitutes the

internal mode. The methodology allows time steps based on the advective, rather than the gravity, wave speed as in conventional explicit finite difference methods, and therefore results in a computationally efficient solution procedure (Swanson, 1986; Swanson et al., 1989; Muin, 1993).

The environmental heat transfer model, (Mendelsohn, 1998) at the water surface contains a balance of the important terms governing the flow of heat, including:

- short wave solar radiation
- long wave atmospheric radiation
- long wave radiation emitted from the water surface
- convection (sensible) heat transfer between water and air
- evaporation (latent) heat transfer between water and air

A detailed description of the equations used for the environmental heat transfer model is given in Appendix B.

5.2 Power Spray Module Model

For periods of high temperatures the Station employs a power spray module system to cool the effluent plume in the discharge canal before emptying into the River. The power spray system consists of 56 floating spray modules, each containing 4 spray nozzles. The modules are deployed along the canal and pump the heated effluent through atomizing nozzles, creating droplets that are sprayed into the air to cool. The increased surface area enhances cooling. The spray module configuration in the effluent canal can be clearly seen in the Google Earth image presented in Figure 5-1.

Figure 5-1. Aerial over flight image showing the power spray configuration in the effluent canal.

In order to simulate the cooling effects of the spray modules, an analytical model of the module performance was implemented in the BFHYDRO model system. The module cooling performance is based on the work of Maulbetsch and Bartz, (1985), based in turn on work done by Porter et.al. (1976). The temperature change across a single module can be estimated as:

$$\frac{T_i - T_s}{T_i - T_{wb}} = 1 - exp\left(-NTU\ \frac{b_f}{C_{p,w}}\right)$$

where

T_i = inlet water temperature, (°C)
T_s = cooled spray temperature, (°C)
T_{wb} = wet bulb temperature, (°C)
NTU = Number of transfer units (an empirical constant back calculated from field data)
b_f = constant, (J / kg °C)
$C_{p,w}$ = specific heat of water , (J / kg °C)

The spray module equation can then be solved for the cooled spray temperature (T_s) as follows:

$$T_s = T_i - (T_i - T_{wb})\left[1 - exp\left(-NTU\ \frac{b_f}{C_{p,w}}\right)\right]$$

The heat constant b_f and $C_{p,w}$ are evaluated as a unit, and the values are given in Table 5-1. Literature values for NTU vary between 0.255 and 0.49 (Maulbetsch and Bartz, 1985); a value of 0.255 best matches the data for this application. The hydrothermal model is configured such that the spray module effects can be turned on or off at any time depending on the actual usage or test being performed. The implementation of the spray module system for the Merrimack application was tested during the model calibration assessment and proved to be robust, as will be discussed in the model calibration section below.

Table 5-1. Thermodynamic data for the spray module equation.

T (°F)	T (°C)	$b_f / C_{p,w}$
50	10	0.545
59	15	0.650
68	20	0.785
77	25	0.960
86	30	1.185
95	35	1.470
104	40	1.845

5.3 WQMAP System

ASA personnel have developed and applied many computer modeling tools. In conducting aquatic environmental analyses, ASA has developed a modeling system, which integrates geographic information (land use, watersheds, etc.), environmental data (water quality parameters, surface elevations and velocities, stream flows, bathymetry, etc.) and models (analytical and numerical, hydrodynamic, pollutant transport, etc.). The power of such a system, called WQMAP (Water Quality Mapping and Analysis Program) (Mendelsohn, et al., 1995), is that it allows the user to model and analyze many different scenarios efficiently. A graphical user interface simplifies user inputs and allows a graphical display of model output. In addition, the modeling components within ASA's WQMAP have been specifically developed for application to the study of thermal effluents in coastal waters, and widely used to undertake such analyses, by parties including utility owners and regulators.

The geographic information component of WQMAP holds user-specified layers of data appropriate for and available to be used to address a specific task. For instance, in this instance

such layers might include shorelines, intake locations, the discharge canal, monitoring data locations, etc. Each data layer can be easily input, either directly into WQMAP with a mouse and screen forms, or through import from existing geographic information system software. Data can be exported as well. Each layer can be displayed separately or in any combination. Graphics can be generated and displayed, either printed or stored for later use.

The environmental data component of WQMAP stores and displays actual environmental data, which are needed for analysis or used in model input or calibration. This component links to standard external programs, such as databases, spreadsheets, and data contouring packages. Importing to and exporting from other systems is also possible.

A suite of tools in WQMAP can be used to import, export and analyze environmental data. Time series of data at single or multiple stations can be imported, processed and displayed. Other measuring systems (e.g., moored current meters, sea surface radars, acoustic Doppler current profilers) can also be accessed and incorporated into the Model.

5.4 WQMAP System Applications

The BFHYDRO model in WQMAP has been successfully used in many hydrodynamic and hydrothermal studies both in the U.S. and worldwide with results accepted by a variety of federal and state government agencies, including the following:

- U. S. Environmental Protection Agency
- U. S. National Oceanic and Atmospheric Administration
- U. S. Army Corps of Engineers
- U.S. Naval Oceanographic Office
- Massachusetts Department of Environmental Protection,
- Massachusetts Coastal Zone Management
- Rhode Island Department of Environmental Management
- Rhode Island Coastal Resources Management Council
- Vermont Agency of Natural Resources
- Connecticut Department of Environmental Protection
- New York State Department of Environmental Conservation
- South Carolina Department of Health and Environmental Control
- The World Bank

Examples where the Model has been successfully applied to thermal plume applications include the following:

- Indian Point Energy Center, Buchanan, NY (Swanson et al., 2010)
- Fore River Station at Weymouth, MA (EAI et al., 1998)
- RESCO Facility at Lynn, MA (Swanson and Isaji, 2001)

- Vermont Yankee at Vernon, VT (Swanson et al., 2004)
- Brayton Point Station at Somerset, MA (Swanson et al., 2006; Swanson et al., 1998)
- Arabian Gulf (Shahriar et al., 2003)
- Ras Tanura Integrated Project, Ras Tanura, Saudi Arabia (Crowley and Mendelsohn, 2010).

ASA is also presently modeling the discharge canal for the Brayton Point Station in Somerset, MA and the Indian Point Energy Center in Buchanan, NY in support of permit renewals.

6 Model Application to the Merrimack River

The model application to the River included definition of the physical characteristics of the study area such as River geometry in the area of interest, bathymetry and appropriate boundary definition including identification of the forcing at the boundaries. The following sections further describe these aspects of the application.

6.1 Grid Generation

The first step in generating a boundary-fitted grid, using WQGRID, is to define the study area of interest, e.g., the Pool on which the Station is located. Experience with previous model applications indicates that the upstream boundaries should be sufficiently upstream in order to allow for the model to reach equilibrium between water temperatures and environmental forcing. To facilitate this need, a detailed model grid was developed for the Hooksett Pool, which extends from Garvins Falls upstream to the Hookset Dam downstream, to reflect the known shoreline features, while upstream of the Hooksett Pool was represented by a uniformly straight river, sized to approximate the average upstream River widths. The northern upstream boundary cells, upstream of Garvins Falls were represented as model river cells, which allow model forcing of time varying river flow and temperature at this location. The southern boundary cells at Hookset Dam were represented by open boundary cells which allow model forcing of time varying surface elevation and temperature. Additional river cells were added to represent the Suncook tributary inputs south of the plant; while the northern Soucook tributary flow was included in the upstream boundary cells. Based on the need to simulate the vertical structure in the River, the Model application used a three dimensional representation of the water column. This means that, for every grid cell defined by lateral and longitudinal coordinates, the vertical water column is divided into an equal number of layers, which for this application was 11 layers.

The WQGRID component of WQMAP consists of a set of tools to generate a boundary fitted grid. The grid is specified by locating grid points along shorelines and bathymetric features. Each point has assigned indices to keep track of how each grid point relates to its neighbors. The grid spacing in the domain is roughly determined by grid spacing at land boundaries. Finer grid resolution was specified for increased model resolution of the thermal discharge from the plant. Once the boundary grid points along the shoreline have been specified, and any interior bathymetric feature grid points located, the gridding model generates all the remaining interior points. These points are constrained to obey a Poisson equation, and their locations are solved iteratively by a Poisson solver. Technical details can be found in the WQMAP User's Manual (ASA, 1996).

In this application, the full grid covers the approximate 9.6 km (6 mi) span of the Pool as well as 48 km (30 mi) north of the upstream end of the Pool. Figure 6-1 shows the grid covering the Pool in general and Figure 6-2 shows the grid zoomed in on the area local to the plant discharge

canal. The Pool is represented by 10 cells across the River width with varying longitudinal sizes depending on the feature or modeling resolution need. In the upstream area north of Garvins Falls, longitudinal grid cell length varies from 800 – 1,200 m (2,600 – 3,900 ft); the grid in this region is represented by approximately 540 water cells in 11 layers totaling 5,940 grid cells. In the area of interest the longitudinal grid resolution varies from 15 m (49 ft) in the region where the canal discharges into the River to 150 m (492 ft) at locations further away from the canal. The Pool is represented in this area by approximately 1,520 water cells in 11 layers totaling 16,720 grid cells and the canal is represented by an additional 164 water cells in 11 layers totaling 1,804 grid cells. In total there are 2,224 water cells in 11 layers totaling 24,464 grid cells, of which a total of 18,524 cells represent the Pool and canal.

Larger grid cells were used further upstream and downstream from the Station in order to minimize the model computations required, while there was more resolution near the Station and in the canal, still providing accurate predictions. This number of grid cells and cell resolution is more than adequate for this application.

In general, the grid aspect ratio reflects a priori estimates of expected flows. This means that the longer grid dimension, if any, is oriented along the major axis of the flow. This approach is necessary because the hydrodynamic model has inherent advective time step restrictions based on the ratio of grid size to flow speed. Faster model runs are possible when the grid is optimized in this manner.

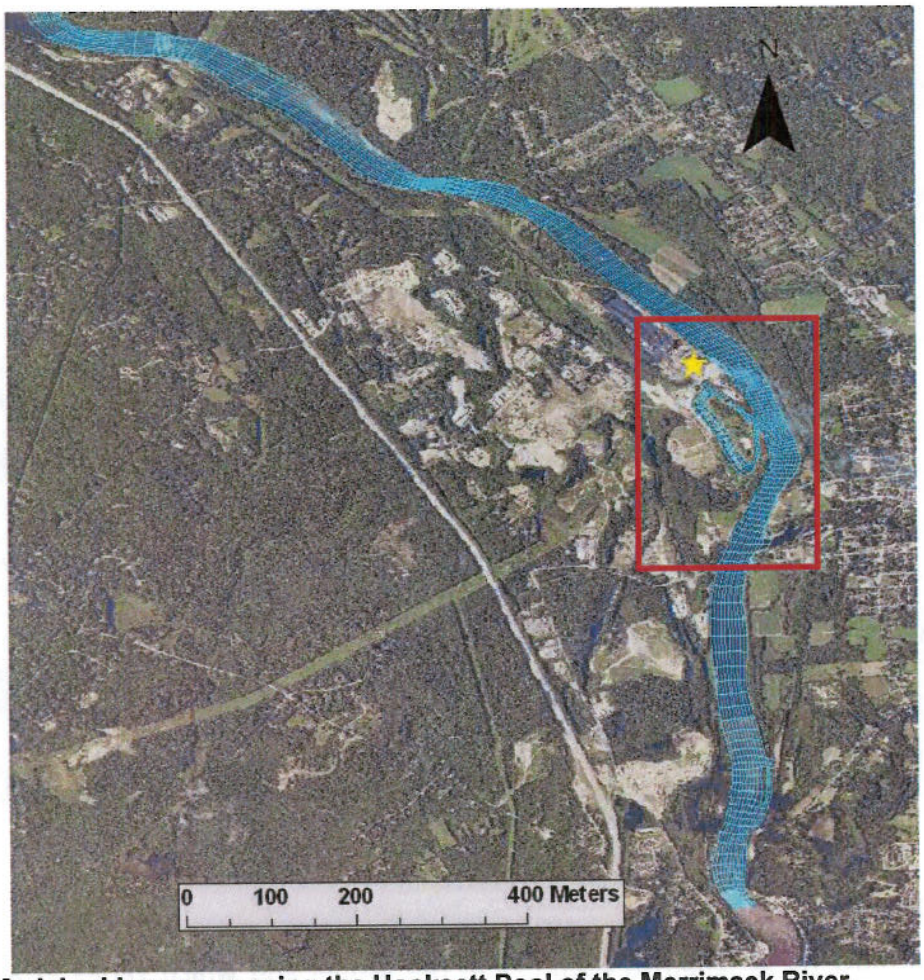

Figure 6-1. Model grid encompassing the Hooksett Pool of the Merrimack River.

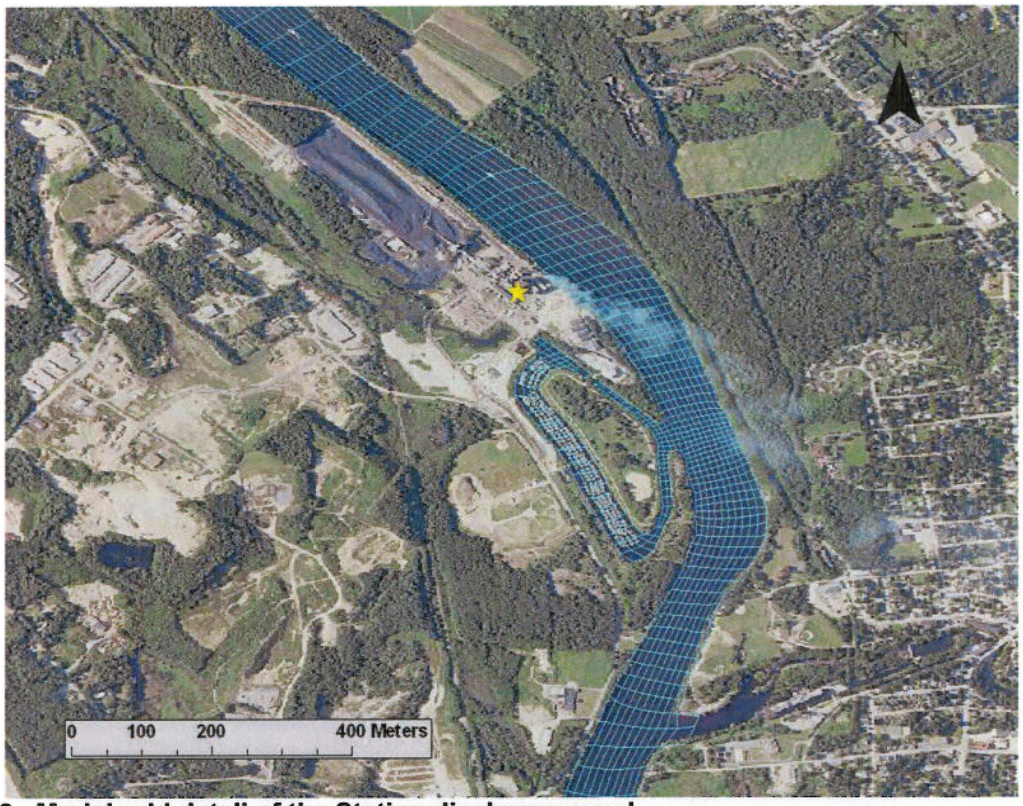

Figure 6-2. Model grid detail of the Station discharge canal.

6.2 BATHYMETRY

A depth value must be assigned to each cell in the Model grid which varies as a function of River flow and associated pool elevation. Pool elevation at the Hooksett Dam was recorded by at an hourly time interval by PSNH with values provided in reference to an elevation datum of 58.52 m (192 ft). During 2009 the Pool elevation ranged from 0.3 – 1.7 m (1 - 5.6 ft) above the reference datum. Model grid bathymetry was then derived from four individual surveys of River sounding measurements taken on different dates and their corresponding pool elevations. The survey dates and corresponding Pool surveys are summarized in Table 6-1. Since pool elevation varies with River flow, the soundings were set relative to a constant pool elevation of 0.94 m (3.1 ft) relative to the dam reference datum elevation. Each grid cell was automatically assigned a depth value by interpolation from the data, based on a distance-weighting algorithm for soundings close to each grid location. Figure 6-3 shows the model grid bathymetry for the Pool. It should be noted that model forcing includes river flows which can cause variations in water surface elevation; this is the mechanism for representing the time varying River depths.

Table 6-1. Bathymetric surveys.

Survey Focus Area	Date	Hookset Pond Elevation m (ft)
Hooksett	30-Apr-09	0.945 (3.10)
Canal	8-May-09	0.884 (2.90)
Hooksett	30-Jul-10	0.823 (2.70)
Hooksett	14-Aug-10	0.747 (2.45)

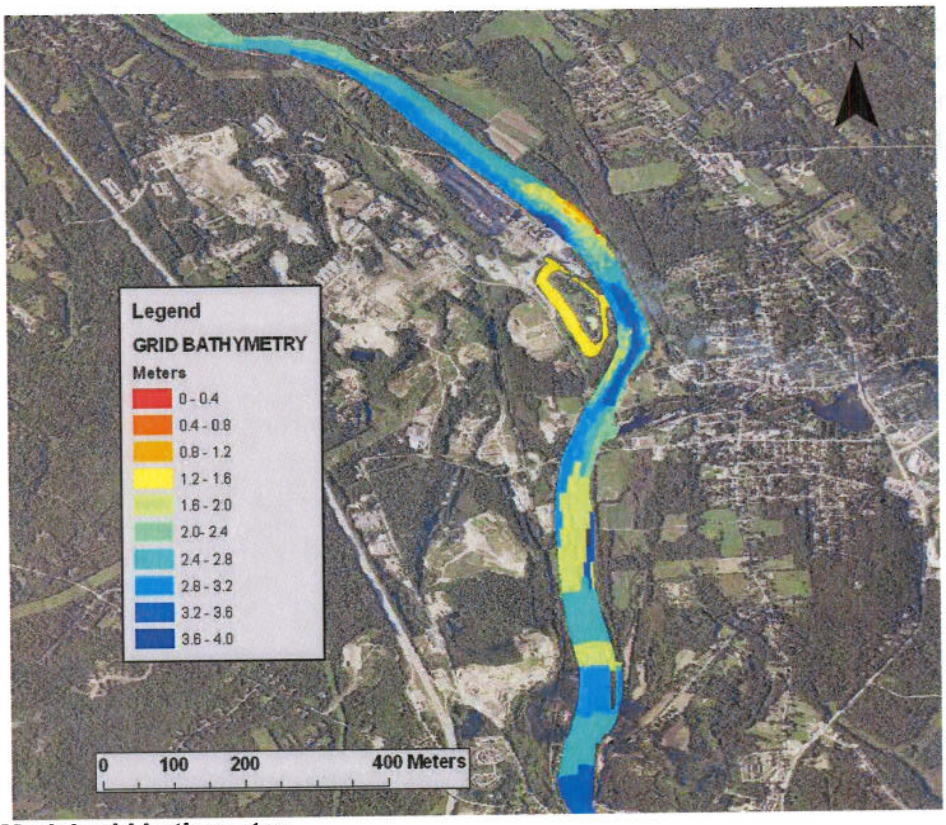

Figure 6-3. Model grid bathymetry.

6.3 Boundary Conditions

The 11-layer, 3-dimensional boundary fitted hydrodynamic Model (BFHYDRO) employed to determine the circulation and thermal distribution requires a set of boundary forcing conditions for each step. River flow, water surface elevation, temperature and winds are major forcing functions important in driving the circulation, while solar radiation and auxiliary parameters,

such as air and dew point temperature, relative humidity and pressure, play an important role in determining the thermal field.

The Model was forced at its open boundaries which include elevation at the lower River boundary at the Hooksett Dam, flow and temperature input at the upper River boundary representing the flow at Garvins Falls Dam plus the Soucook Tributary, flow at the Suncook tributary, energy exchange at the water-air boundary at the River surface, and necessarily the thermal discharges into the River from the Station. The model forcing changes with time, as the surface elevation, water temperature, river flows and meteorological conditions change. The upstream River boundary conditions were developed assuming the NAI estimated flow at Garvins Falls and the Soucook tributary while assuming water temperatures were the same as those observed at N10H. The tributary inputs of the Suncook were developed similar to the upstream river boundaries however the relationships describing the hourly flow at the Suncook were developed by ASA as a function of the estimated NAI Soucook flow. The water temperatures at the Soucook were assumed the same as those observed at N10H. The downstream water surface elevations were developed using the input supplied by PSNH describing the pool elevations with temperatures assumed equal to N10H. Meteorological forcing was developed based on observations at Concord Airport located approximately 7.2 km (4.5 mi) north northeast of the Station. The forcing for the combined calibration & validation and model scenario period are described separately in section 7.3 and 8.2 respectively.

7 Model Calibration and Validation

Modeling studies typically consist of model calibration and validation steps. Calibration is performed to determine the most appropriate modeling coefficients and forcing mechanisms, which are finalized when there is good agreement between observational data and model simulations. Model validation consists of running model simulations for a time period outside the calibration timeframe while not changing modeling coefficients and forcing mechanisms with the exception of accounting for temporal variations in model forcing characteristics, in order to validate the appropriateness of the modeling coefficients.

7.1 Selection of Time Periods

Modeling calibration and validation time periods are limited by data availability. Periods are chosen that best represent the conditions for which further use of the model is planned; in some instances a system may need to be calibrated differently for different sets of conditions (eg. summer vs. winter). In most cases of thermal discharge summer periods are of a primary interest since these correspond to lower River flows and higher air and water temperatures resulting in less capacity for environmental cooling of a thermal discharge, therefore the model was calibrated and validated for summer conditions. Figure 7-1 shows the environmental and plant operating conditions as well representative observed River temperatures gathered during the short term intensive 2009 monitoring program.

The calibration timeframe chosen was 5 - 15 August 2009. This timeframe was chosen because it falls during the summer season when River flows are low and water and air temperatures are high. Furthermore this period reflects a period of time of indicative summer environmental forcing with sunny days (consistent solar radiation) contributing to constant River flow and increasing River flow temperature (due to environmental forcing – as observed north of the Station). In addition, fairly constant Station output was recorded, with Unit 1 only operational and power spray modules were off for this entire timeframe. Furthermore the observed thermal plume is typically strongest at S0-West Top (See Figure 3-2); however at times at this location there is not always a significant, visible, response in temperature. The calibration period was chosen as it reflects a period of observed thermal plume in the River.

The validation timeframe chosen was 11 - 21 July 2009. This timeframe is similar to the calibration timeframe with the exception that both units, as well as the power spray modules, were operational. As with the calibration timeframe it falls during the summer season with sunny days, contributing to constant River flow and increasing ambient River temperature as well as fairly high Station output with both units operational. As mentioned above, during this period the power spray modules were operational. This time period also reflects a noticeable thermal response in the River as observed in short term fixed observation stations, most notable the S0-West Top thermistor (temperature observations denoted as S0-WT in Figure 7-1, station location as show in Figure 3-2).

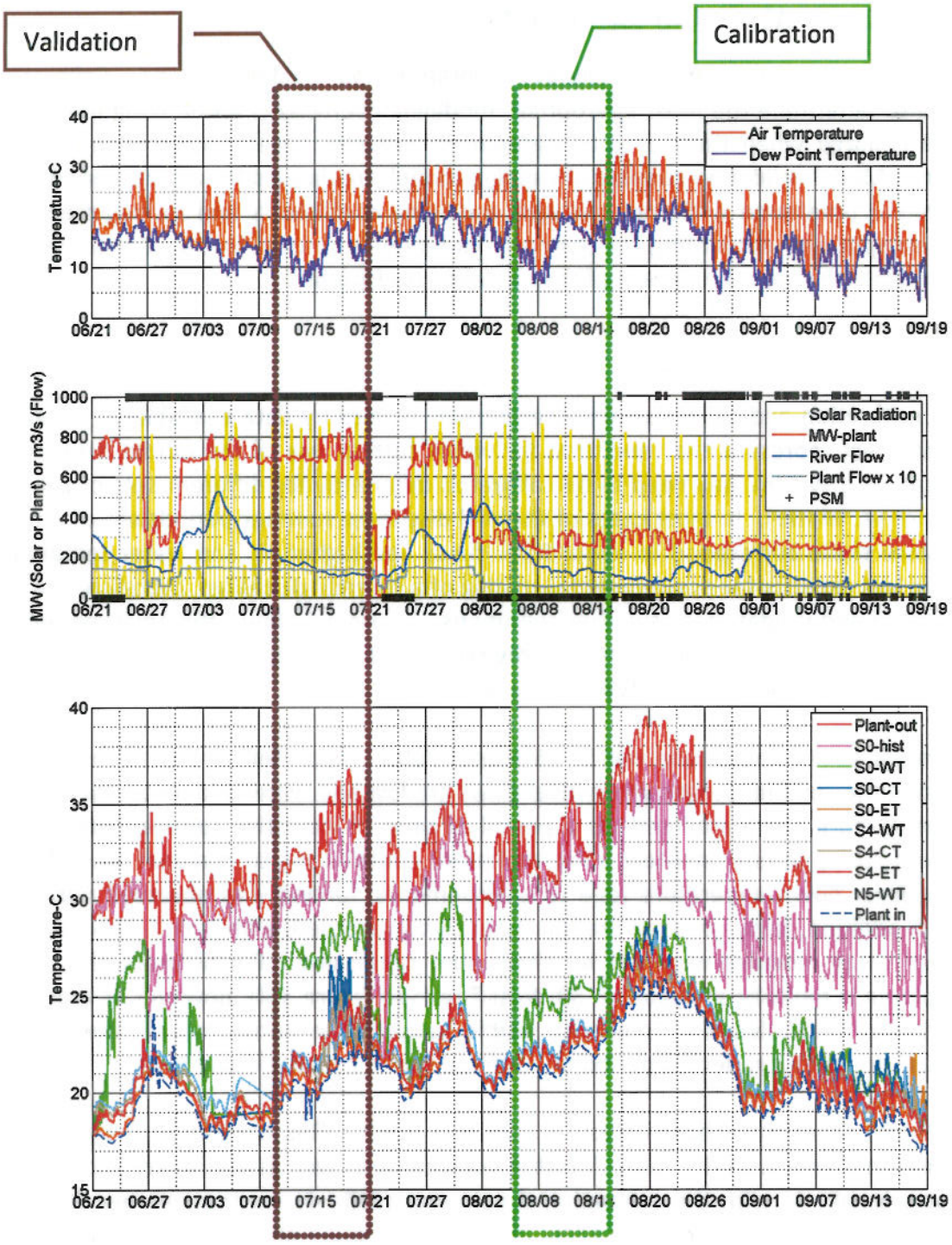

Figure 7-1. Summer environmental and plant characteristics.

7.2 Calibration / Validation Procedure

For the calibration effort, a total of over 100 model runs were executed to determine the sensitivity of the model to variations in the representation of upstream conditions, initial conditions and model parameters to find the set that gave the best model results in comparison with observations. The resulting hydrodynamic model parameters ultimately chosen included a Mannings n of 0.03 for the Chezy formulation of bottom friction, spatially variable vertical eddy viscosity and diffusivity with higher upstream values, 0.005 and 0.05 m^2/sec (0.054 ft^2/s and 0.54 ft^2/s) respectively, chosen to reflect the known turbulent characteristics of the rapids and increased mixing that occurs as the water travels over dams. A different set of values were applied to the water cells in Pool, 0.005 and 0.01 m^2/sec (0.054 ft^2/s and 0.011 ft^2/s), respectively, reflecting the conditions experienced within the Pool. The horizontal eddy diffusivity for temperature was selected as 1.000 m^2/sec (10.8 ft^2/s) to best match the data. The net surface heat fluxes were computed using observed solar radiation and other environmental parameters (air temperature, dew point temperature, winds and relative humidity).

These hydrodynamic and temperature parameters were selected to minimize the difference between model predictions and observations, using the qualitative and quantitative evaluation metrics that will be described in the section below. The purpose of the qualitative comparison is to evaluate how well the model performed from a visual, but subjective perspective using plots and animations. The purpose of the quantitative comparison is to evaluate model performance based on objective statistical measures. In both approaches the analysis involved a comparison of model predictions to the observations made at the moored thermistors strings measuring water temperature.

7.3 Model Forcing

7.3.1 Upstream River Boundary

The upstream boundary forcing consisted of time varying River flow and water temperature. The River flow estimates were based on observations of flow at USGS station 1089100: Soucook River, as well as statistical relationships developed by NAI (NAI 2007) of flow at Garvins Falls based on Soucook River flow. The original observational data at USGS station 1089100 was recorded in fifteen minute intervals; however the output of the NAI estimates of flow is in hourly intervals. The River temperature estimates were based on observations at N10 which were available in 15 minute intervals that were averaged on an hourly basis and then subsampled on the hour for an end result of an hourly interval of River water temperature. Also included in the upstream boundary River flow was a volume flow estimated for the Soucook River which was based on a relationship developed by ASA between the Soucook and Suncook tributaries by developing a correlation of USGS observed daily flows at the Suncook to daily Soucook River flows, this daily correlation was then used to develop the corresponding hourly estimates at the Soucook River. Observed Soucook water temperatures were not

available, and therefore the decision was made to include the flow in the upstream forcing with temperatures based on N10 temperatures; in lieu of additional information this approach was assumed to have the least amount of impact on improperly affecting model predicted River temperatures in the area of interest. It should be noted that the NAI developed relationships of flow at different tributaries and ungauged locations along the River assume the same temporal characteristics of the gauged site, meaning there is no account for travel time of flow, and adds some uncertainty to the model forcing.

River flow reflective of the combined Garvins Fall and the Soucook flow was applied to the northern boundary of the model domain, however given the offset in distance the record was offset in time by negative 15 hours in order to account for travel time of flow down the upstream portion of the River and have observed proper flow values at Garvins Falls at times corresponding with those anticipated based on the observation/statistical method described above. The time of travel and corresponding time offset of flow varies with overall flow magnitude, however a constant time offset of -15 hours was applied for average flow conditions. Figure 7-2 shows the upstream River boundary flow and temperature for a period that encompasses both the calibration and validation time frames, from 1 July through 15 August 2009, which encompasses both the calibration and validation time frame, which are identified in the figure.

During the calibration time frame of 5 August -15 August the River flow starts at approximately 350 m^3/sec (12,300 cfs) with diurnal temperature variability between 21 - 22°C (69.8 – 71.6°F), and decreases in flow from 5 to 10 August to approximately 100 m^3/s (3,500 cfs) while temperatures remain between 21 - 22°C (69.8 – 71.6°F). After this time the flow remains steady from the 10 through 15 August with increasing temperatures that vary through the day between 23°C - 24°C (73.4 – 75.2°F).

During the validation time frame of 11 July – 21 July the River flow starts at approximately 200 m^3/sec (7,100 cfs) with a daily diurnal temperature variability between 19.5 - 21°C (67.1 – 69.8°F) and decreases from 11 - 16 August to approximately 100 m^3/s (3,500 cfs) where it remains steady from 16 August through 21 August at temperatures that vary through the day between 21 - 23°C (69.8 – 73.4°F).

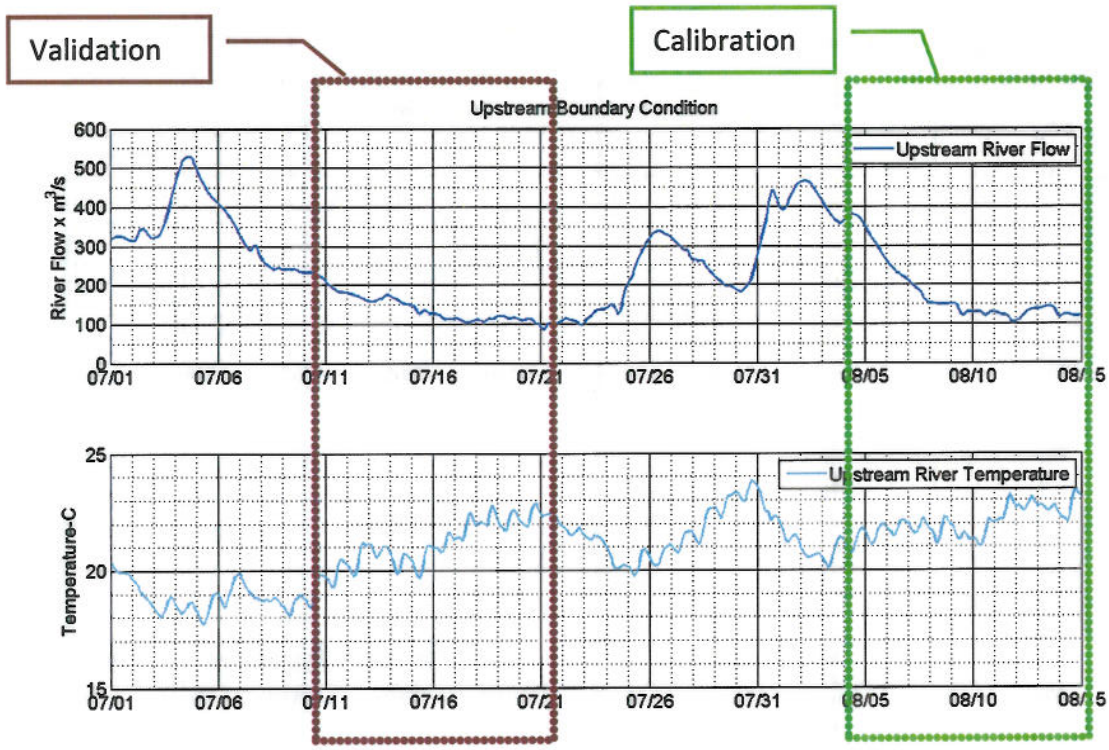

Figure 7-2. Upstream boundary forcing characteristics.

7.3.2 Downstream Hooksett Dam Boundary

The downstream boundary forcing at the Hooksett Dam consisted of water surface elevation and River temperature. Water surface elevation was provided by PSNH and was available in hourly intervals as a measurement of elevation with respect to a known datum of 58.52 m (192 ft). As the surface elevation in coordination with the bathymetry gives the total water column depth at any given time the boundary surface elevation data was adjusted relative to the same reference datum as the bathymetry. River temperatures at the Hooksett Dam were estimated based on N10 River temperatures; however since the water is always flowing downstream, these temperatures do not impact water cell temperatures calculated by the model. Figure 7-3 shows the time series of water surface elevation and temperature applied at the downstream boundary cells. During the calibration period the surface elevation varied between –0.3 m to 0.2 m (-1 to 0.66 ft), with daily variability approximately 0.1 m (0.32 ft.). During the validation period the surface elevation varied between –0.2 m to 0.1 m (-0.66 to -0.33 ft), again with daily variability approximately 0.1 m (0.32 ft.).

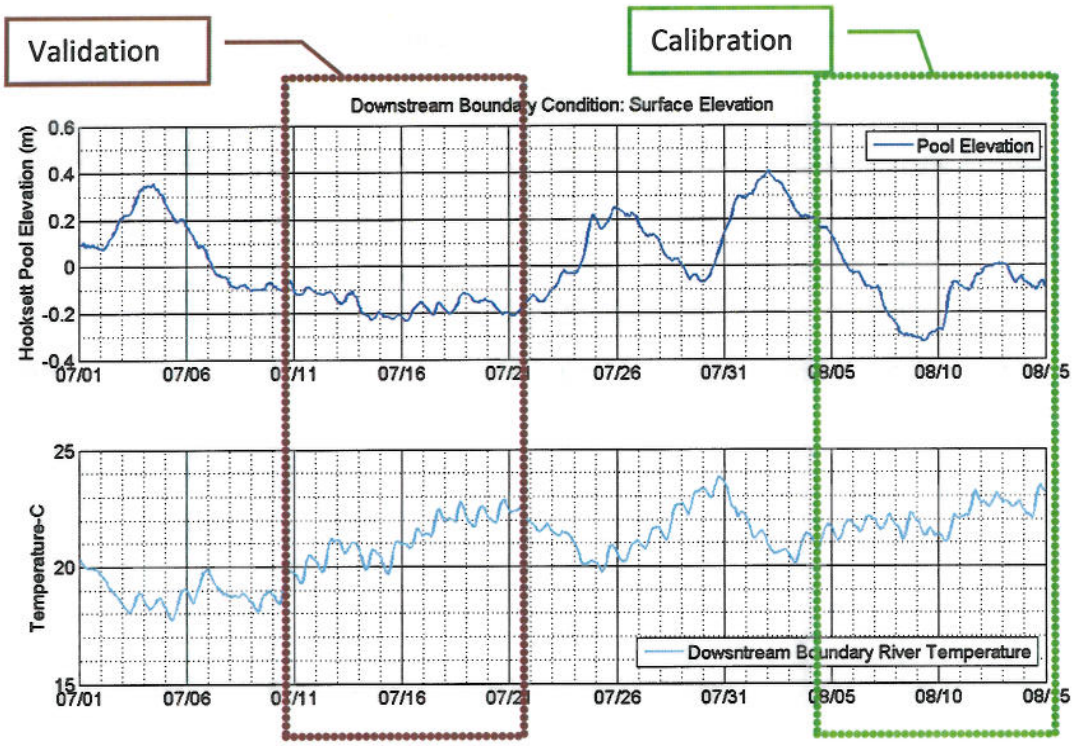

Figure 7-3. Downstream boundary forcing characteristics.

7.3.3 Suncook River Boundary Inputs

In addition to the upstream forcing which includes all River flow input north of the plant, there is a small amount of flow from the Suncook tributary which enters the main stem south of the plant on the eastern side approximately two miles above the Hooksett Dam. The flow from the Suncook was estimated in the same manner as the flow at Garvins Falls; a statistical relationship between flow at the Soughegan station and the Suncook was developed and observations at the Soughegan for the simulation period were used with these developed relationships to generate an estimated time series of flow at the Suncook. There were no observations of temperature available at the mouth of the Suncook and therefore temperatures were assumed equivalent to those observed at monitoring station N10. Figure 7-4 shows the time series of river flow and temperature inputs as applied at the Suncook River boundary cells.

During both the calibration and validation timeframe the Suncook River flow inputs are very small, less than 10% of the overall River flow. The flow range during the calibration time frame is generally less than 10 m^3/s (350 cfs), however a peak on the 12 July was observed at 20 m^3/s (700 cfs). The flow range during the validation time frame is fairly constantly between 10-15 m^3/s (350 – 529 cfs). As noted previously there are no measurements of tributary water temperatures during the simulation time periods and therefore the water temperatures were assumed equal to that at N10, ranging between 21 - 24°C (69.8 - 75.2°F) during the calibration

timeframe and between 19 - 23°C (66.2 – 73.4°F) during the validation time frame as described in the previous section.

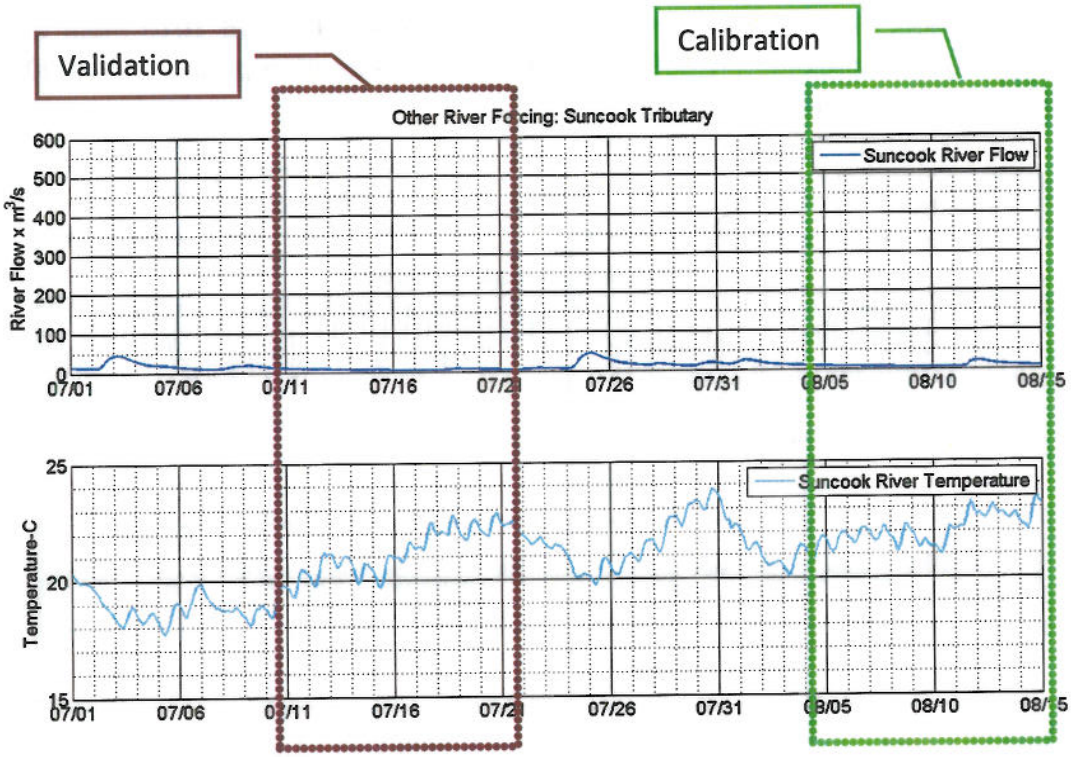

Figure 7-4. Other River forcing characteristics.

7.3.4 METEOROLOGICAL CONDITIONS

The meteorological variables used in the model were those from the Concord Airport (CON). The data consisted of air temperature, dew point, relative humidity, wind speed and direction, pressure and radiation. Figure 7-5 shows the time history of these variables during the period from 1 July to 16 August.

The air temperature was relatively constant during this period, typically with a diurnal variability of between 5-15°C (9 - 27°F) depending on weather conditions; peak air temperatures during the calibration time period ranged from 23-30°C (73.4 - 86°F) and ranged from 21 - 29°C (69.8 - 84.2°F) during the validation time frame. The dew point had a much smaller diurnal range though it followed the air temperature trends. The dew point temperature also had a signal that is the inverse of the air temperature, decreasing when the sun is shining (normal solar radiation) appears to track the seasonal trend of air temperatures. The relative humidity varied from 30 to 100%, tracking the signal of solar radiation closely where higher values occur when there is little or no solar radiation.

Figure 7-5 also shows the wind and is plotted as a vector with its length scaled to the speed and its direction pointing downwind (oceanographic convention). The wind during the calibration and validation timeframe was generally weak, between 3.9 - 9.7 knots (4.5 - 11.1 mph), and variable in direction. Atmospheric pressure varied between 990 and 1010 mbar and solar radiation peaked at approximately 800 W/m^2 during the calibration period and at 900 W/m^2 during the validation period.

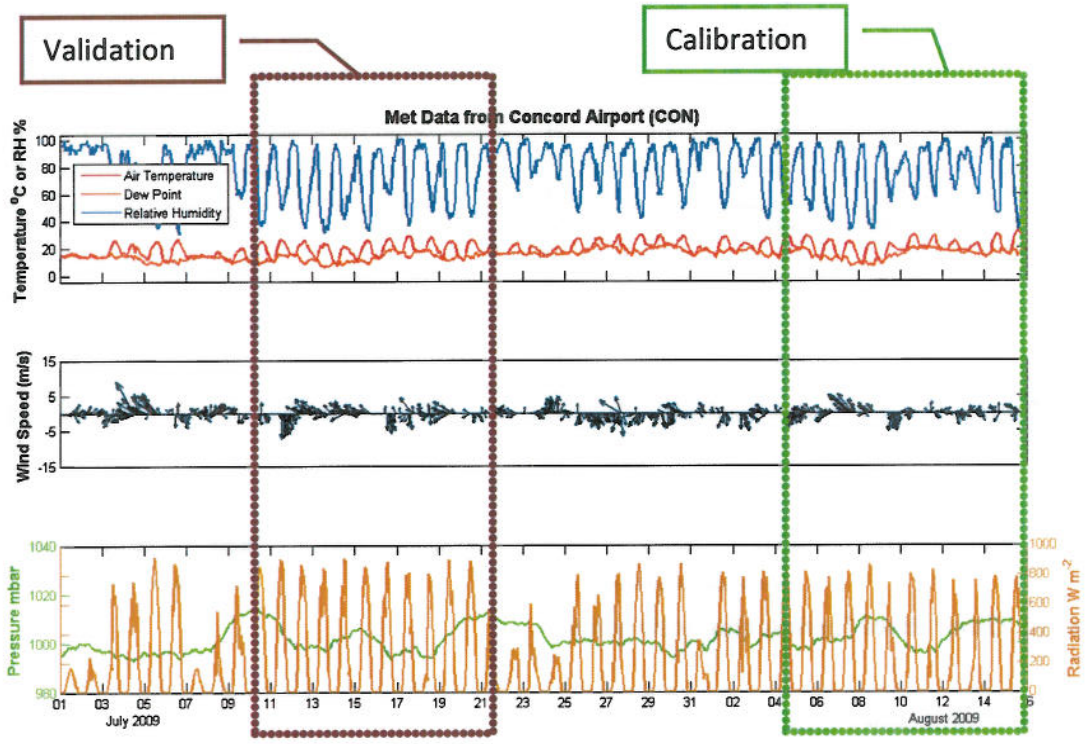

Figure 7-5. Meteorological observations.

7.3.5 Plant Thermal Discharge

Three sets of data were provided to ASA by PSNH through NAI, allowing the thermal discharge from the Station to be calculated; one describing the timing of operation of various Station features (boilers & pumps), one describing the temperatures at various points of interest, and the third describing the Hooksett Pool elevation which effects Station pump throughput.

The Station has two condensers (MK1 and MK2) and each condenser has two cooling water pumps. Documentation regarding the number of hours that each boiler and each set of pumps were in operation at the Station for 2009 was provided by PSNH along with supplementary text that explained how to generate an hourly record of plant output and pump flow from these daily records. Additionally, a record of temperatures observed on an hourly basis at the inlet and outlet locations for both MK1 and MK2 condensers was provided by PSNH. As there are

two inlet thermistors and two outlet thermistors for each unit, a total of eight hourly records were provided.

Lastly, an hourly record of observed water elevation at the Pool was provided by PSNH as previously noted. River elevation affects the pressure head at the pump intakes and therefore the flow through the cooling loop is dependent on the River stage (surface water elevation). Relating the stage to the pump flow is important in order to capture the real heat rejected from the Station to the cooling water. Table 7-1 outlines the empirical relationship between pond elevation in the Pool and the capacity of pump flow for each unit. Figure 7-6 displays the water levels as given before any processing, including a number of short data. The values presented in Figure 7-6 were used in conjunction with the empirical values in Table 7-1 to evaluate hourly water flow through the Station. Together these data sets were used to evaluate the energy discharged from the unit in an hourly time series. The following steps were taken for processing:

1. Periods with short records of missing data were filled in using linear interpolation. Longer periods where data was absent were not interpolated and these time periods were avoided during calibration of the model.
2. Statistical outliers were taken to be bad data and were removed and interpolated linearly with closest available data points.
3. Pairs of inlet and outlet flows were averaged to improve data quality.

In order to calculate heat flow from the Station, all records were converted into hourly time series for 2009. For each hour, the number of hours the water pumps were in operation was multiplied by the capacity as a function of the Pool elevation to define the hourly discharge from each water pump. A single flow weighted ΔT was determi ned from the boiler data MK1 and MK2. The megawatt load of the Station was determined simply by multiplying the flow weighted ΔT by the total discharge of the Station multiplied by a constant coefficient (dependent on the units of the two variables). Figure 7-7 shows the Station thermal discharge as calculated in this manner.

Table 7-1. Relationship between pond elevation at the Hooksett Pool to the operating capacity of each of the water pumps at Merrimack Station.

Pond Elevation (ft)	Unit 1		Unit 2	
	1 Operating Pump (GPM)	2 Operating Pumps (GPM)	1 Operating Pumps (GPM)	2 Operating Pumps (GPM)
188	21,400	17,000	63,500	61,500
190	25,800	24,000	67,000	65,000
192	28,000	27,000	70,000	68,000
194	29,800	29,000	73,000	71,500
196	31,400	30,800	76,000	74,000
198	32,000	32,000	78,000	77,000
200	32,600	32,600	81,000	79,500
202	32,600	32,600	83,000	82,000
204	-----	-----	85,000	85,000

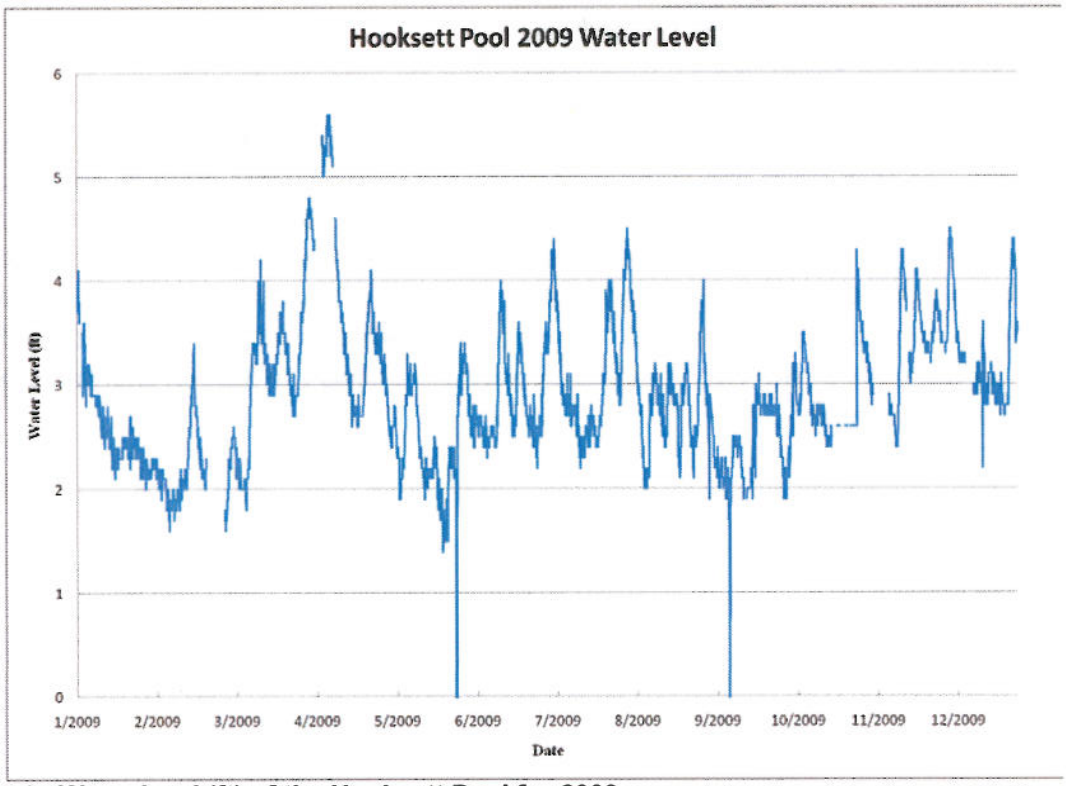

Figure 7-6. Water level (ft) of the Hooksett Pool for 2009.

7.3.5.1 POWER SPRAY MODULE OPERATION

In addition to the Station output, pump flow and temperature rise through the cooling loop, the Station also provided a history of on/off times in which the power spray modules (PSM) were utilized. The power spray modules provide enhanced cooling by pumping water from the bottom of the discharge canal and spraying the water into the air over the canal thereby increasing surface exchange with the environment and returning it to the canal cooler than it would be had it not been sprayed. Figure 7-7, which shows the Station operation characteristics, also shows the times when PSM operation is on (denoted by a heavy black line indicator on the top of the y axis) or off (denoted by the indicator on the bottom of the y axis).

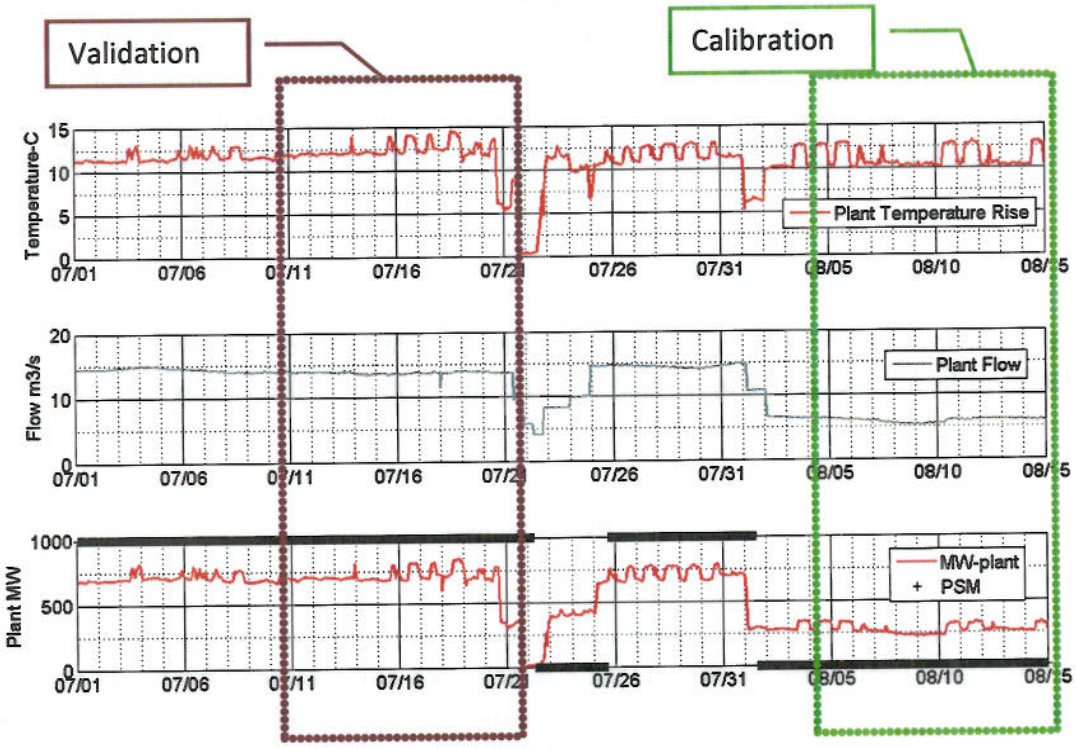

Figure 7-7. Plant operations.

7.3.6 QUALITATIVE COMPARISONS

The comparison of model results and observations depends on data dimensionality. For example, a time series of data collected at a particular site can be plotted together with model output to provide a visual comparison. This comparison can provide information on the suitability of the model to simulate the range of variability evident in the observations.

The most direct way to provide a qualitative comparison is to plot the model predictions and

the observed data for each variable over the time of the simulation. This can be done with time series plots of the variables of interest or contour plots when looking at spatially varying patterns.

7.3.7 Quantitative Comparisons

Quantitative comparisons are statistical measures that can be applied to the model predictions and field data sets that provide a numerical assessment of the comparison. These statistical measures can be grouped into two major components: those measures that describe an individual set of data (e.g., a time series of one variable), and those that relate the degree of difference (error) between two data sets (e.g. time series of model predictions and field observations). Individual statistical measures include the mean, standard deviation, percentiles, minimum, and maximum. The independent variable can be time, depth or distance in these data. The quantitative comparisons between data sets include relative error, root mean square error, linear regression, comparison of means and correlation coefficient. McCutcheon et al (1990) describes these quantitative comparisons in detail, and provides guidance on acceptable values. Each statistical measure used in this analysis is briefly discussed below.

7.3.7.1 Relative Mean Error (RME)

The relative error measures the difference between calculated and observed mean values and can be defined in a variety of ways. The relative mean error is the relative difference of the means

$$rme = \frac{\bar{x} - \bar{c}}{\bar{x}}$$

where $\bar{x}$ is the mean of the observation values and $\bar{c}$ is the mean of the model-predicted or calculated values. Evaluation of this statistic over space and time can be made to provide a cumulative frequency of error (median error, percentile exceedances). The relative error is expressed as a percentage. This statistic can be unreliable for small values of the mean, and does not provide information on the variability in the data, but can be a useful indicator for general model performance.

7.3.7.2 Error Coefficient of Variation (ECV)

The error coefficient of variation is the ratio of the root mean square error to the mean. It is defined as:

$$ecv = \frac{1}{\bar{x}}\sqrt{\frac{\sum(x_i - c_i)^2}{N}}$$

and is expressed as a percentage.

7.3.7.3 SQUARE OF CORRELATION COEFFICIENT (R^2)

The correlation coefficient (r) evaluates the linear interdependence of the predictions to observations. It is defined as the ratio of the covariance and the standard deviations of predicted and observed values.

$$r_{xy} = \frac{\sum_{i=1}^{n}(x_i - \bar{x})(y_i - \bar{y})}{(n-1)s_x s_y},$$

where x and y are the sample means of X and Y, sx and sy are the sample standard deviations of X, the observations, and Y, the predictions. The squared correlation coefficient is the square of r, and lies between 0 and 1. A value of zero indicates no correlation between two observations and predictions, 1 represents perfect positive correlation and -1 implies perfect negative correlation.

The USEPA has published guidance on the acceptable statistical measure values for model calibration/confirmation (McCutcheon et al., 1990). Table 7-2 shows a summary of the guidance for different measures and properties. The statistical measures have been defined above, and the properties include flow and temperature. There is a unique value presented for each property. McCutcheon, et al. (1990) state that these guidance values are representative of a mean level of calibration/confirmation among multiple comparisons, and are not to be considered an upper limit (RME, ECV) or lower limit (r^2) for individual comparisons.

Table 7-2 Model calibration guidance (McCutcheon et al., 1990).

Error Measure	Property	Value
Relative Mean Error, RME	Temperature	± 25%
Error Coefficient of Variation, ECV	Temperature	± 45%
Squared Correlation Coefficient, r^2	Temperature	0.84

7.3.7.4 SKILL

Another measure of the quantitative comparison between model predictions and observations is skill (Wilmott, 1981)

$$Skill = 1 - \frac{\sum |X_{model} - X_{obs}|^2}{\sum (|X_{model} - \overline{X_{obs}}| + |X_{model} - \overline{X_{obs}}|)^2}$$

A skill value of 1 indicates perfect agreement, and 0 indicates complete disagreement. This measure was recently used in a ROMS model application to the Hudson by Warner et al. (2005) that assessed the performance of the model in resolving the temporal variations from an extensive field data set. They report a skill level of 0.85 to 0.95 for water level, 0.92 for velocity (depth averaged), and 0.85 for salinity (taken here as a proxy for temperature). The approach was used more recently by Ralston et al. (2008) to evaluate salinity stratification and residual velocity in the River.

7.4 Model Calibration / Validation Results

7.4.1 Calibration

The primary focus of the calibration process is to adjust appropriate model parameters to optimize the comparison to a data set of observations. The parameters, as discussed in the previous sections, include bottom friction, horizontal and vertical dispersion, and atmospheric exchange rates. The observed data used for the model calibration are time series of water temperatures taken during the short term intensive field program.

Due to limited River speed observations, the calibration process only considered speeds in a qualitative process, to determine if the model could capture within reason the trend and magnitude of River currents. Figure 7-8 illustrates the current pattern on 6 August. The relative pattern is indicative of the average flow pattern. Figure 7-9 through Figure 7-16 show the modeled and observed contours at transects N5, S0, S4, and S16 respectively. As can be seen from these images, the model was able to capture the trend of speeds at N5 as well as the overall distribution of speeds with the peak velocities occurring on the western surface. At N5 the model predicted peak speeds were approximately 0.65 m/s (2.13 ft/s) while the observed peak speeds were approximately 0.6 m/s (1.97 ft/s). Similarly, the model was able to capture the trend at S0 with smaller velocities at the western shore and peaks in the center towards the east of the channel. Peak speeds at the surface of 0.5 - 0.6 m/s (1.64 – 1.97 ft/s) were simulated as compared to 0.55 - 0.65 m/s (1.88 – 2.13 ft/s) observed on the surface at S0. At S4 the model recreated the trend of smaller western shore currents with maximum speeds found between the center and eastern shore; the model peak surface speeds were between 0.6 – 0.7 m/s (1.97 – 2.30 ft/s) while the observed surface speeds were between 0.55 – 0.65 m/s (1.88 – 2.13 ft/s). At transect S16 the model again was able to capture the trend with peak speeds located on the eastern surface in both modeled and observed. At S16 the model predicted speeds are higher and more uniform than observed, potentially due to differences in the assumed bathymetric features in this area versus the actual.

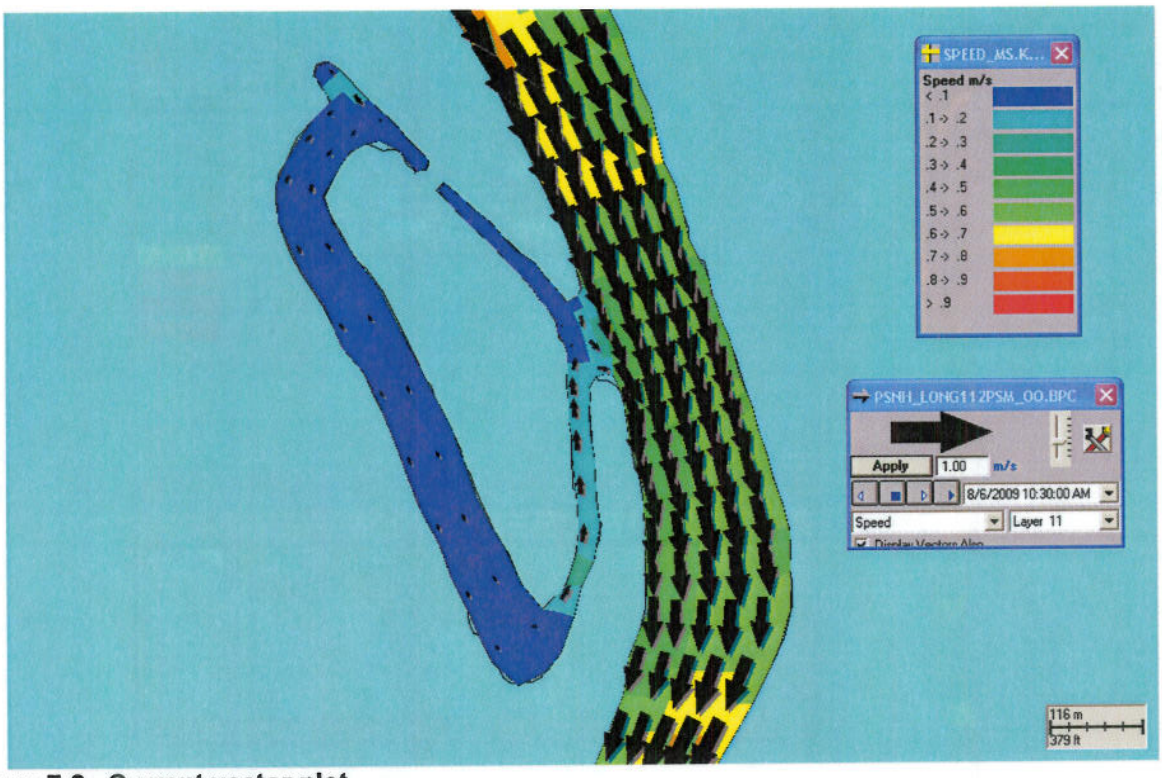

Figure 7-8. Current vector plot.

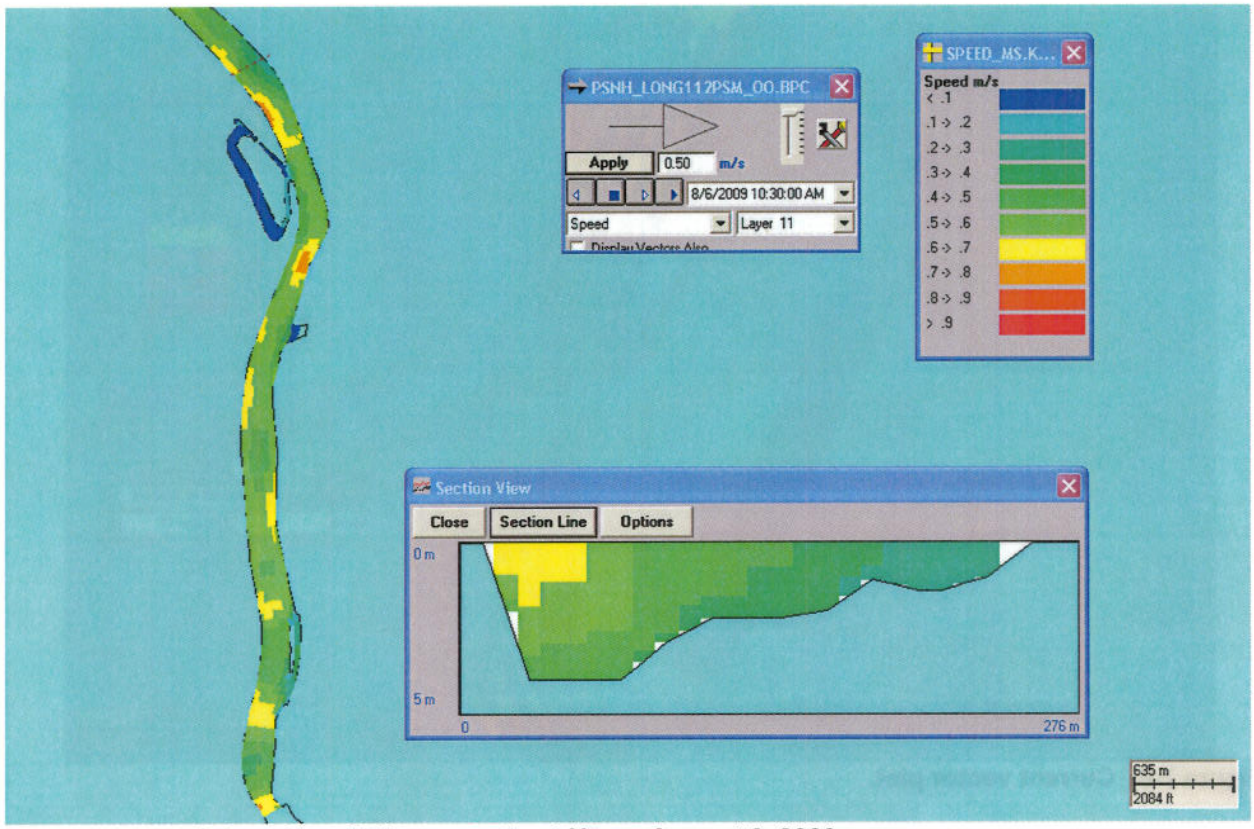

Figure 7-9. Model predicted River speeds at N5 on August 6, 2009.

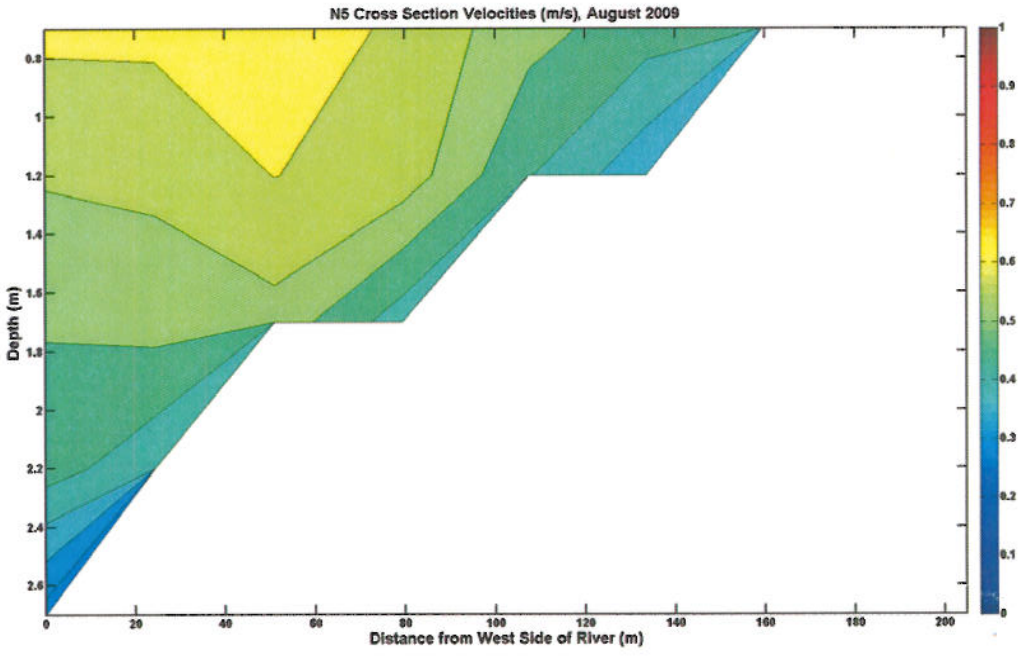

Figure 7-10. Observed River speeds at N5 on August 6, 2009.

Figure 7-11. Model predicted River speeds at S0 on August 6, 2009.

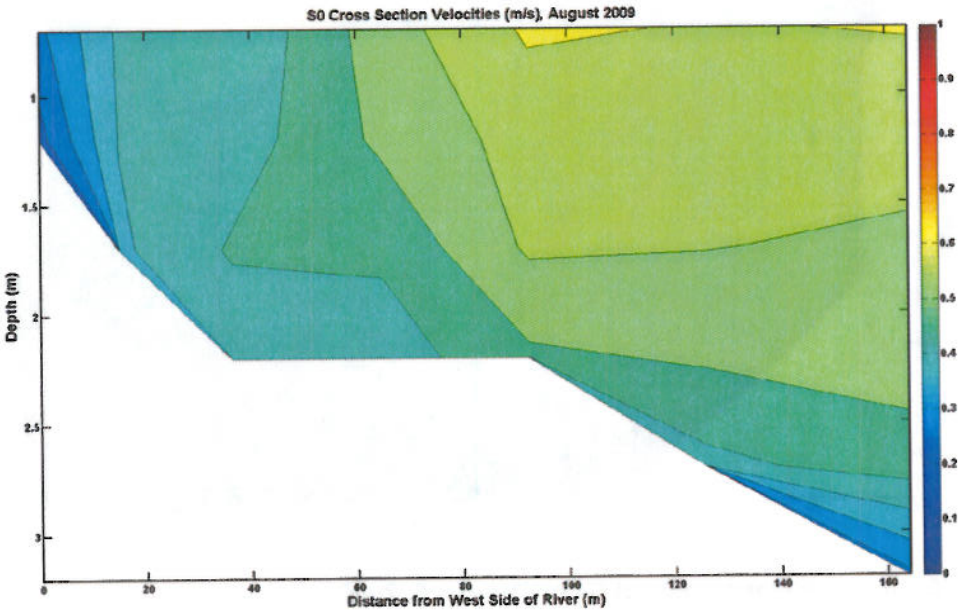

Figure 7-12. Observed River speeds at S0 on August 6, 2009.

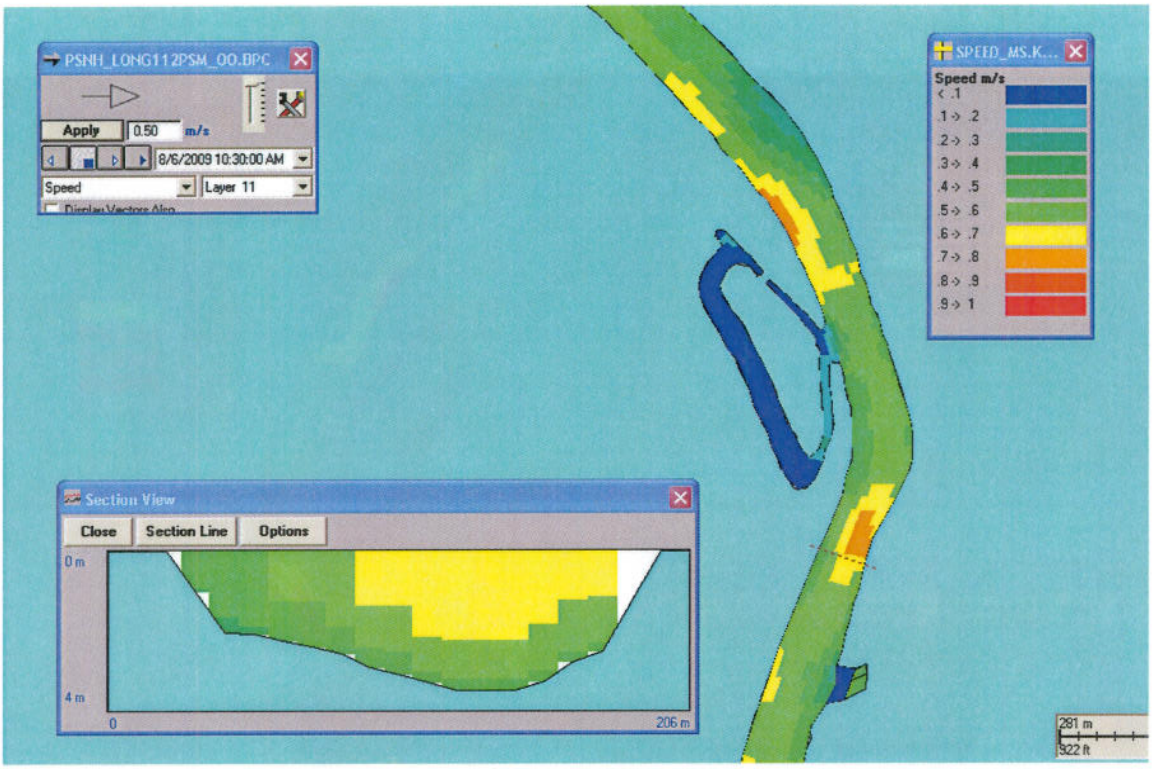

Figure 7-13. Model predicted River speeds at S4 on August 6, 2009.

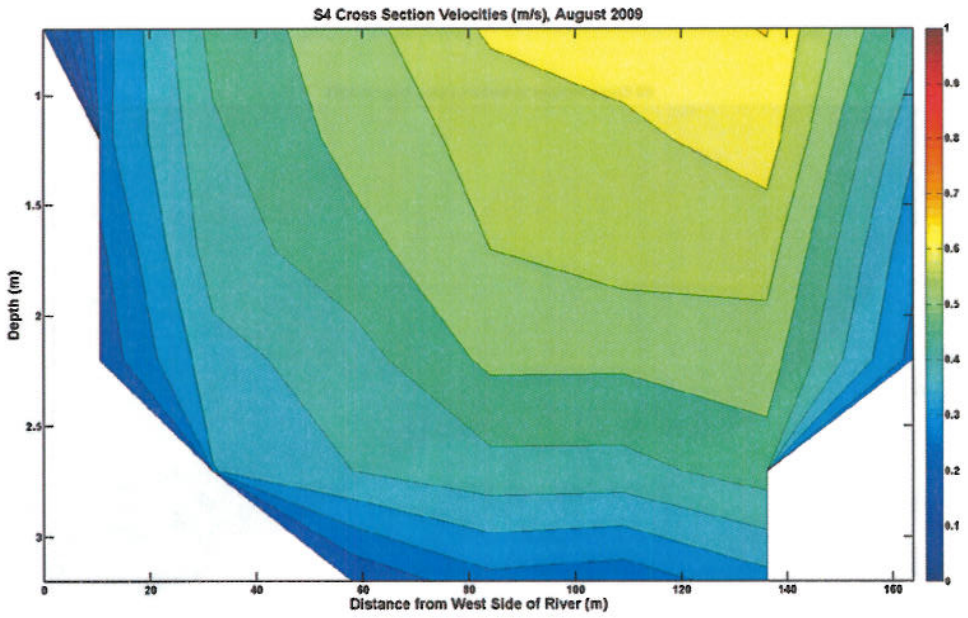

Figure 7-14. Observed River speeds at S4 on August 6, 2009.

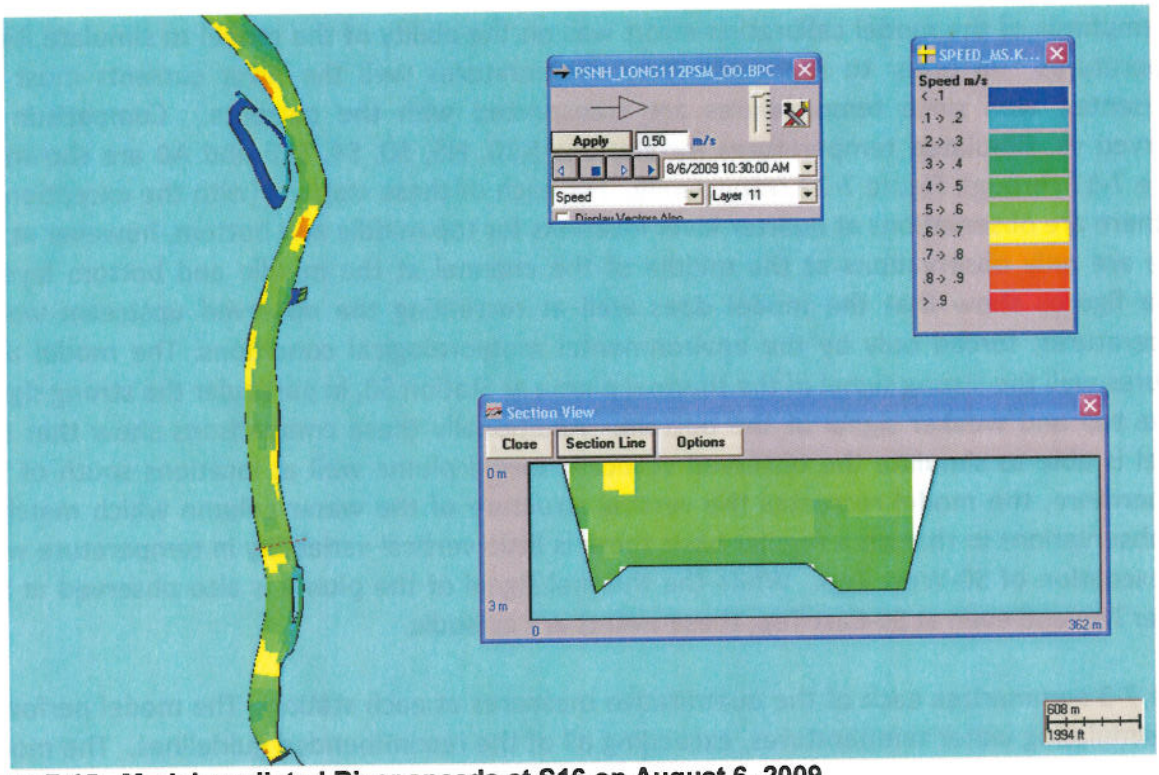

Figure 7-15. Model predicted River speeds at S16 on August 6, 2009.

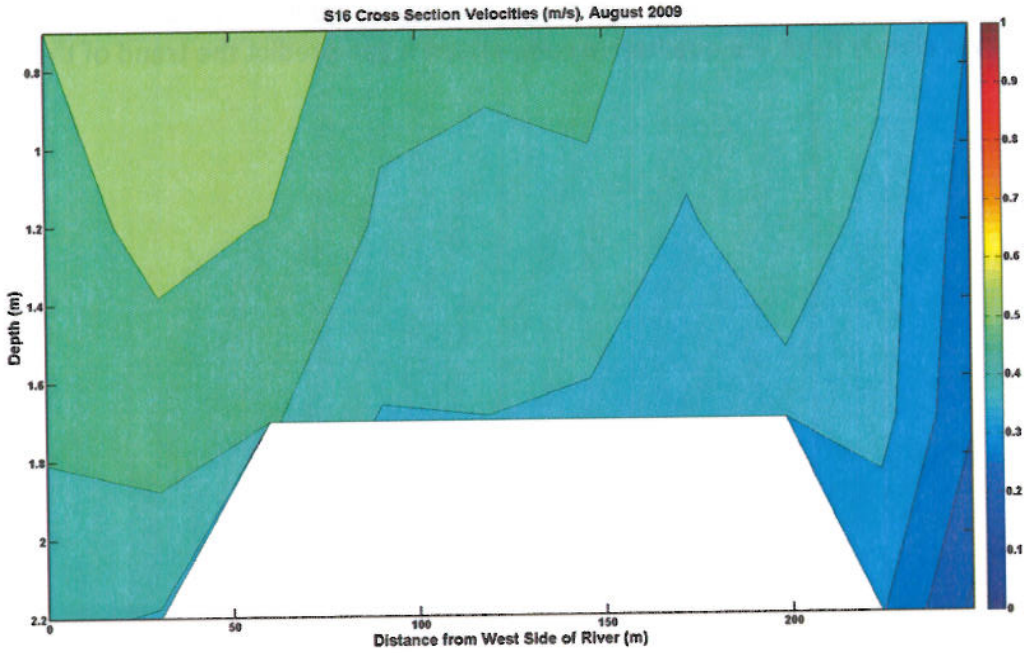

Figure 7-16. Observed River speeds at S16 on August 6, 2009.

The emphasis of the model calibration effort was on the ability of the model to simulate River temperatures. In order to represent River temperatures well the River currents must be represented well since temperatures are transported with the currents. Comparison of observed vs. simulated temperatures for stations N10, N5, S0, S4, S16 and A0 are shown in Figure 7-17 through Figure 7-22 respectively. For each of these stations (with the exception of A0) there are observations at quarter River locations for top middle and bottom, however at A0 there are only observations at the middle of the channel at the middle and bottom layers. These figures show that the model does well at recreating the observed upstream water temperatures, forced only by the environmental meteorological conditions. The model also captures well the strong signal of the thermal plume at Station S0, in particular the strong signal at the top and weaker signal at the bottom. Additionally these comparisons show that the model is able to simulate the observed vertically mixed plume well at locations south of S0. Furthermore, the model recreates the vertical structure of the water column which matches the observations in that on a regular basis there is little vertical variability in temperature with the exception of S0-West Top. While the thermal signal of the plume is also observed at S0-Center Top and even at S0-East Top, these events are episodic.

Table 7-3 summarizes each of the quantitative measures at each station. The model performs well simulating water temperatures, exceeding all of the recommended guidelines. The model performance is stronger at individual stations further away from the canal where the temperatures are influenced primarily by environmental forcing and mixing in the River; at station S0 West closest to the canal discharge the model qualitative performance is slightly lower however clearly from the qualitative comparison it can predict the trend of the plume.

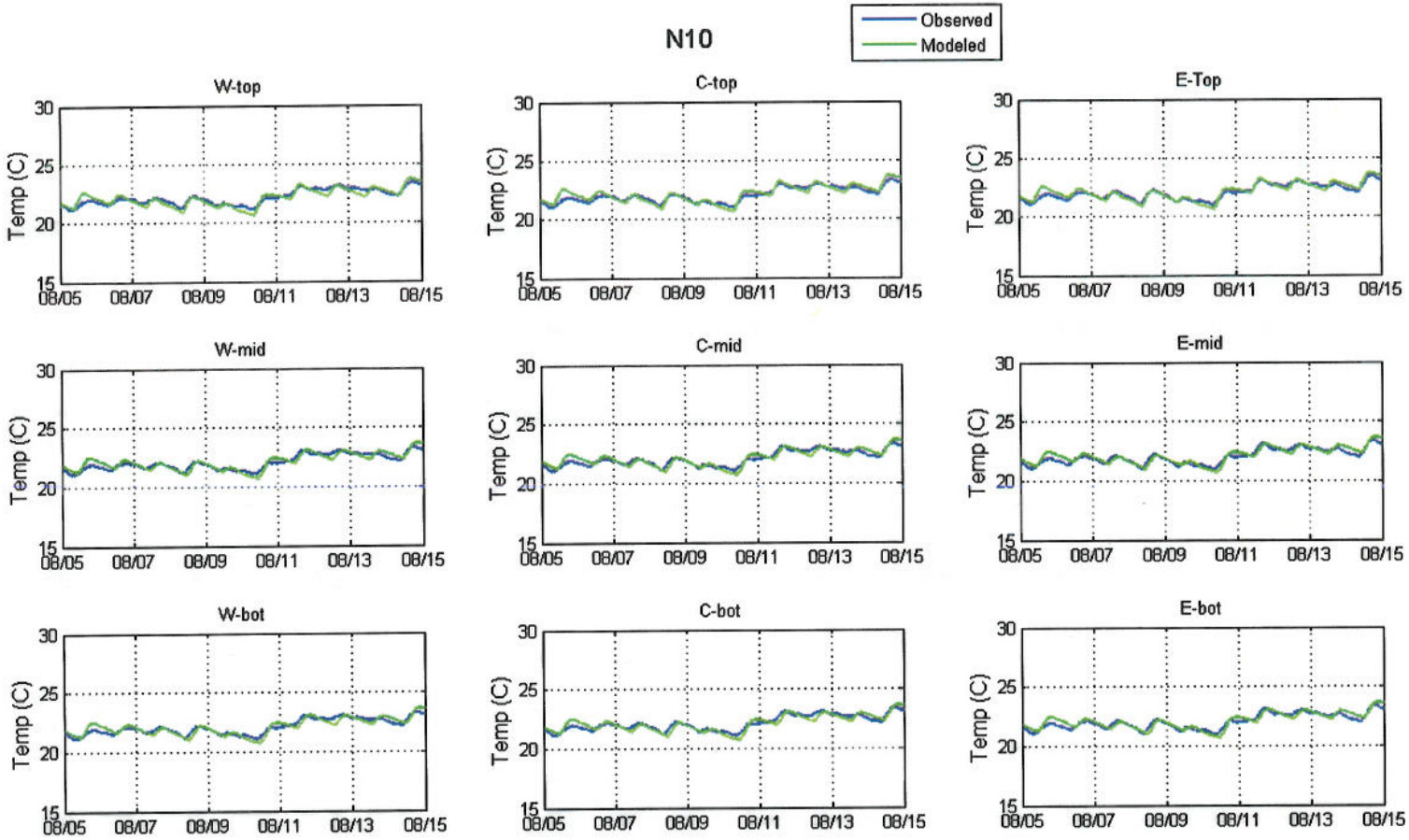

Figure 7-17. N10 observed (blue) versus model predicted temperature (green) during calibration time period.

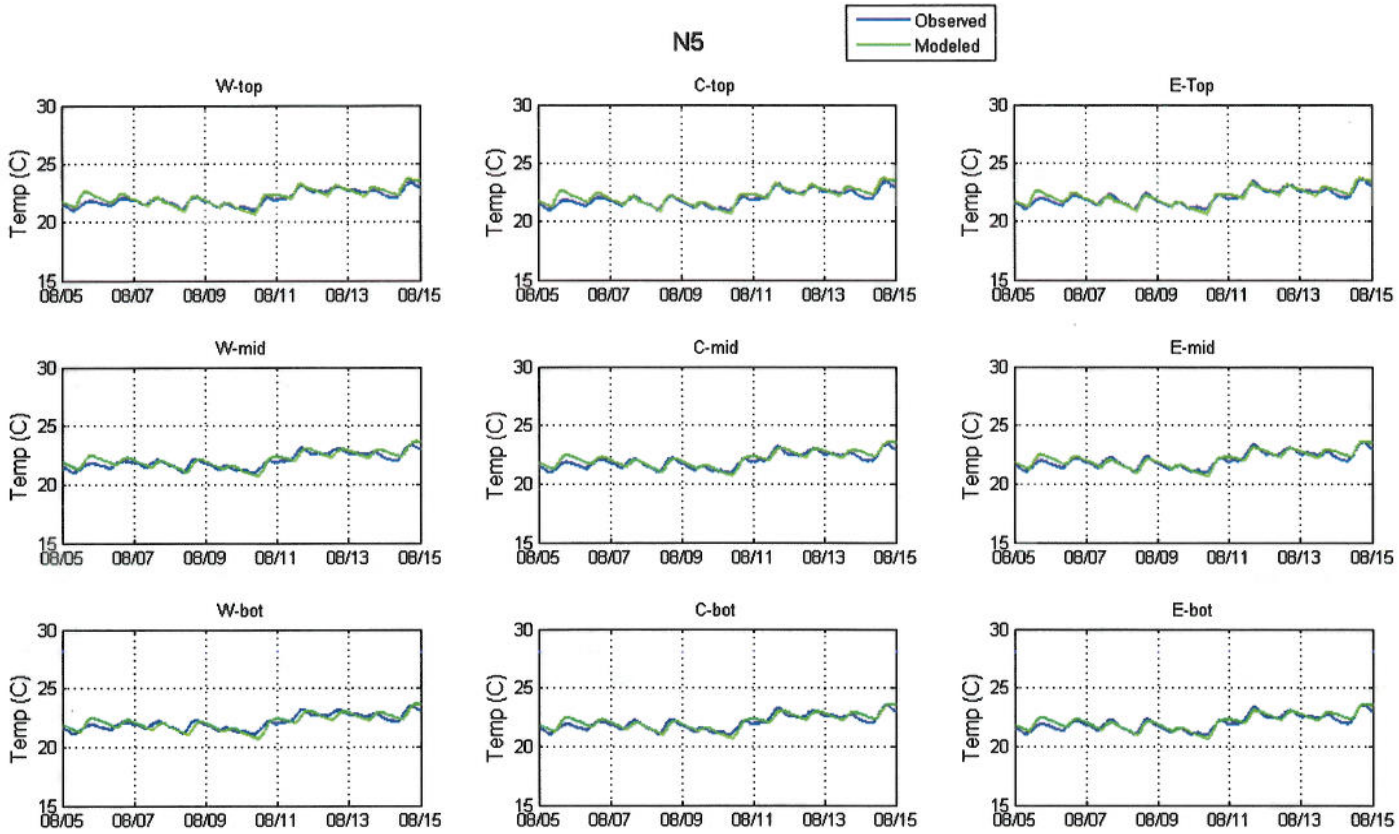

Figure 7-18. N5 observed (blue) versus model predicted temperature (green) during calibration time period.

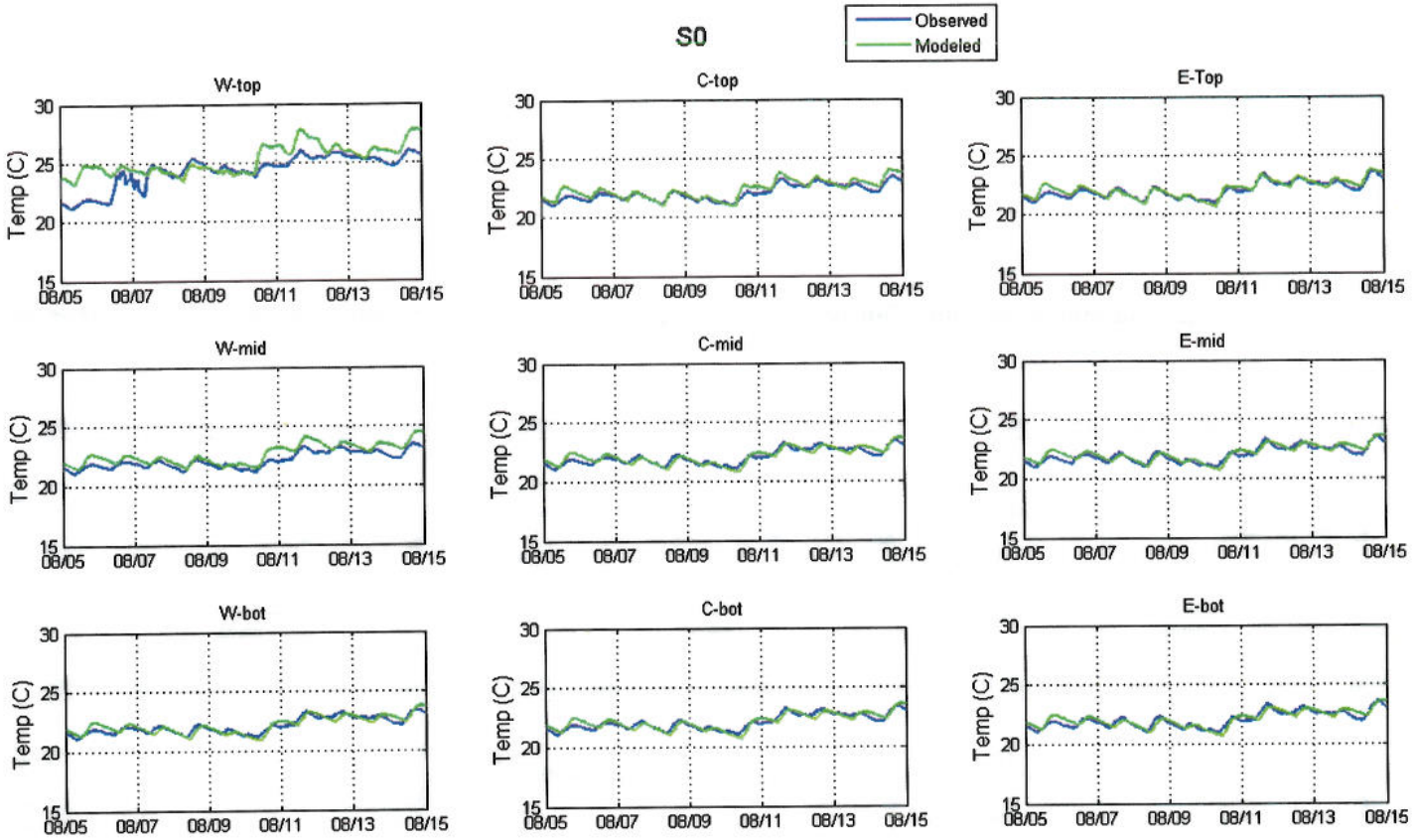

Figure 7-19. S0 observed (blue) versus model predicted temperature (green) during calibration time period.

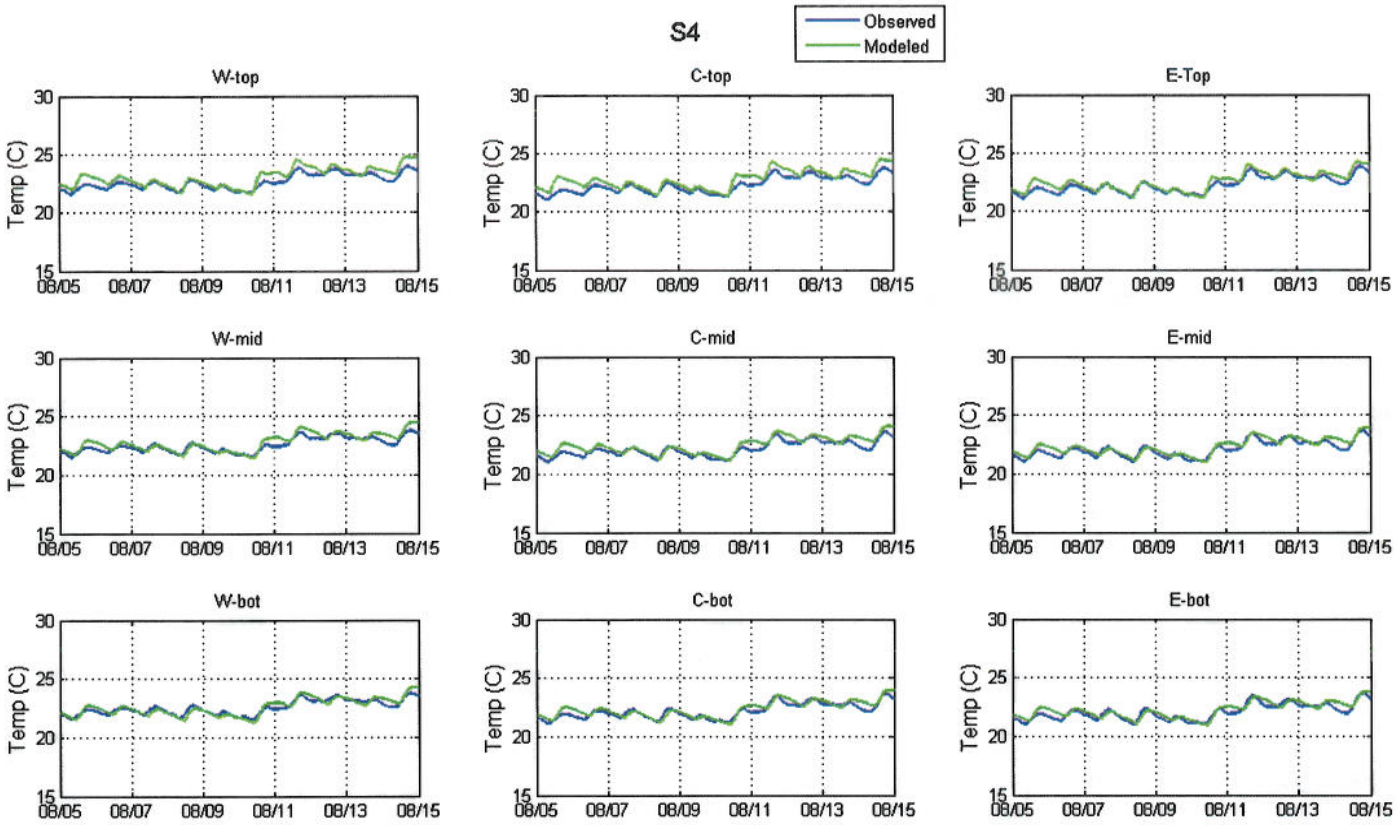

Figure 7-20. S4 observed (blue) versus model predicted temperature (green) during calibration time period.

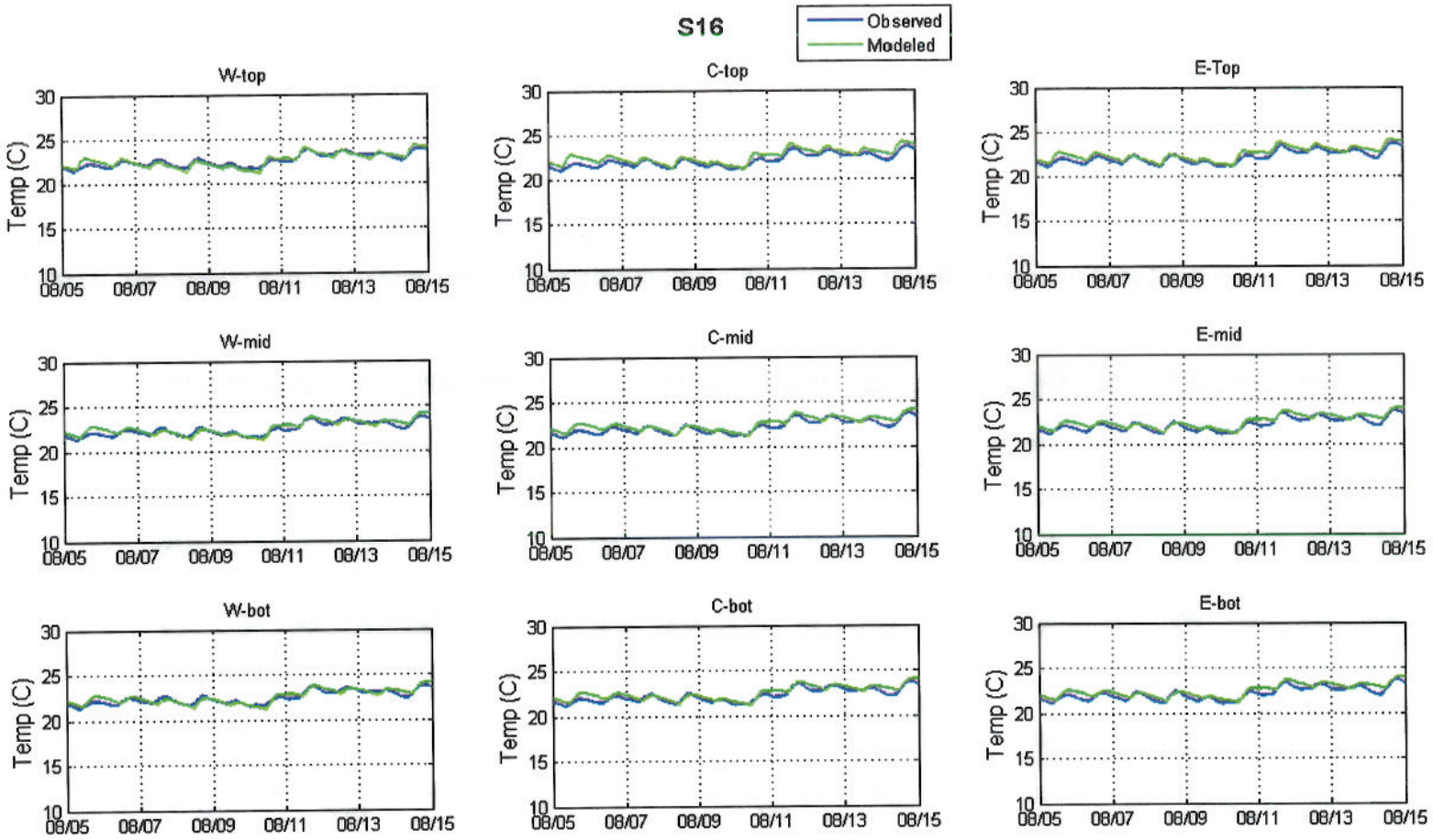

Figure 7-21. S16 observed (blue) versus model predicted temperature (green) during calibration time period.

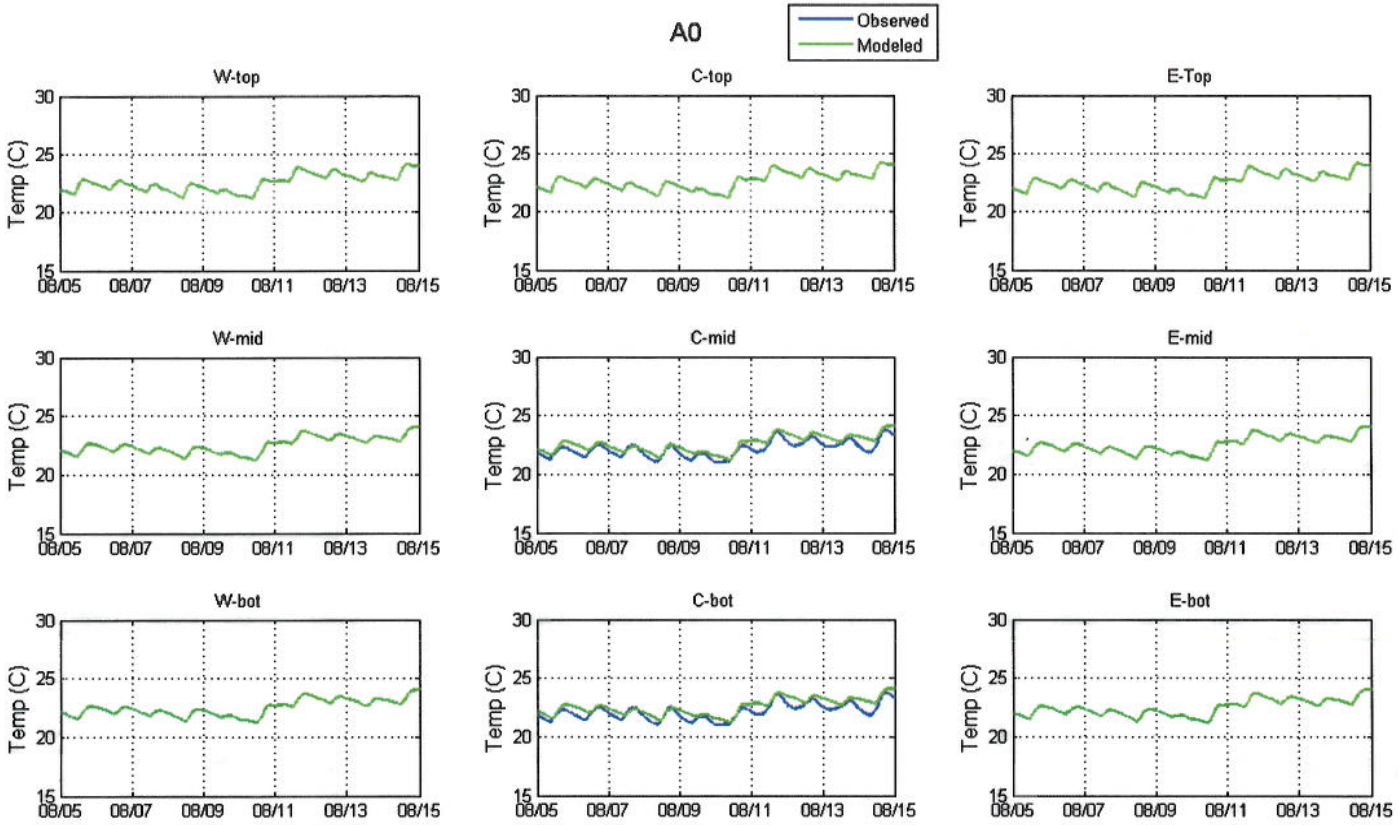

Figure 7-22. A0 observed (blue) versus model predicted temperature (green) during calibration time period.

Table 7-3. Summary of calibration period statistics of model predicted water temperatures.

Station	Location	Position	r^2	rme	ecv	skill
N10	West	Top	0.828	0%	1%	0.95
N10	West	Middle	0.828	0%	1%	0.95
N10	West	Bottom	0.828	0%	1%	0.95
N10	Center	Top	0.828	0%	1%	0.95
N10	Center	Middle	0.828	0%	1%	0.95
N10	Center	Bottom	0.846	0%	1%	0.96
N10	East	Top	0.810	0%	1%	0.95
N10	East	Middle	0.828	0%	1%	0.95
N10	East	Bottom	0.828	0%	1%	0.95
N5	West	Top	0.846	1%	1%	0.95
N5	West	Middle	0.846	1%	1%	0.95
N5	West	Bottom	0.846	0%	1%	0.96
N5	Center	Top	0.774	1%	2%	0.92
N5	Center	Middle	0.828	1%	1%	0.94
N5	Center	Bottom	0.884	0%	1%	0.96
N5	East	Top	0.706	0%	2%	0.92
N5	East	Middle	0.810	0%	1%	0.94
N5	East	Bottom	0.865	0%	1%	0.96
S0	West	Top	0.462	4%	6%	0.71
S0	West	Middle	0.865	1%	2%	0.94
S0	West	Bottom	0.828	0%	1%	0.95
S0	Center	Top	0.846	3%	3%	0.79
S0	Center	Middle	0.828	0%	1%	0.95
S0	Center	Bottom	0.828	0%	1%	0.95
S0	East	Top	0.792	1%	2%	0.93
S0	East	Middle	0.792	1%	1%	0.93
S0	East	Bottom	0.810	0%	1%	0.94
S4	West	Top	0.865	2%	2%	0.87
S4	West	Middle	0.865	1%	2%	0.92
S4	West	Bottom	0.865	0%	1%	0.95
S4	Center	Top	0.846	2%	3%	0.84
S4	Center	Middle	0.846	1%	2%	0.9
S4	Center	Bottom	0.846	1%	1%	0.94
S4	East	Top	0.846	1%	2%	0.91
S4	East	Middle	0.828	1%	2%	0.92
S4	East	Bottom	0.828	1%	2%	0.93
S16	West	Top	0.828	0%	1%	0.95
S16	West	Middle	0.846	1%	1%	0.95
S16	West	Bottom	0.865	0%	1%	0.96
S16	Center	Top	0.846	2%	2%	0.86
S16	Center	Middle	0.865	2%	2%	0.9
S16	Center	Bottom	0.865	1%	2%	0.94
S16	East	Top	0.828	2%	2%	0.88
S16	East	Middle	0.846	2%	2%	0.9
S16	East	Bottom	0.846	2%	2%	0.9
A0	West	Top	0.846	2%	2%	0.9
A0	West	Middle	0.828	2%	2%	0.87
AVERAGE			0.827	1%	2%	0.92
GUIDANCE			0.840	25%	2%	0.85

7.4.1.1 POWER SPRAY MODULE

The PSM enhanced cooling functionality is an optional Station operation that is used during peak output periods in warm ambient conditions. The PSMs are located within the discharge canal upstream of the historical S0H station located also within the discharge canal. A measure of the effectiveness of the PSM is the temperature differential between the Station outfall and S0H with a larger differential for periods of enhanced cooling at the same Station output. As part of the calibration process the implementation of the power spray module solution was evaluated by comparing the observed and model predicted temperature differential between Station discharge and SOH. Figure 7-23 illustrates the temperature rise through the plant as well as the observed and modeled temperature differential between Station discharge and S0H in the upper panel and Station output, flow and indication of PSM operational on/off times denoted by indicator on the top (PSM-on) or bottom (PSM -off) of the y axis in the bottom panel. As can been seen in this figure, the model recreated the increased temperature differential during periods of PSM on and the slightly decreased temperature differential during periods of PSM off. Note that larger model vs. observed differences at the beginning of the simulation are due to the model not yet fully ramped in.

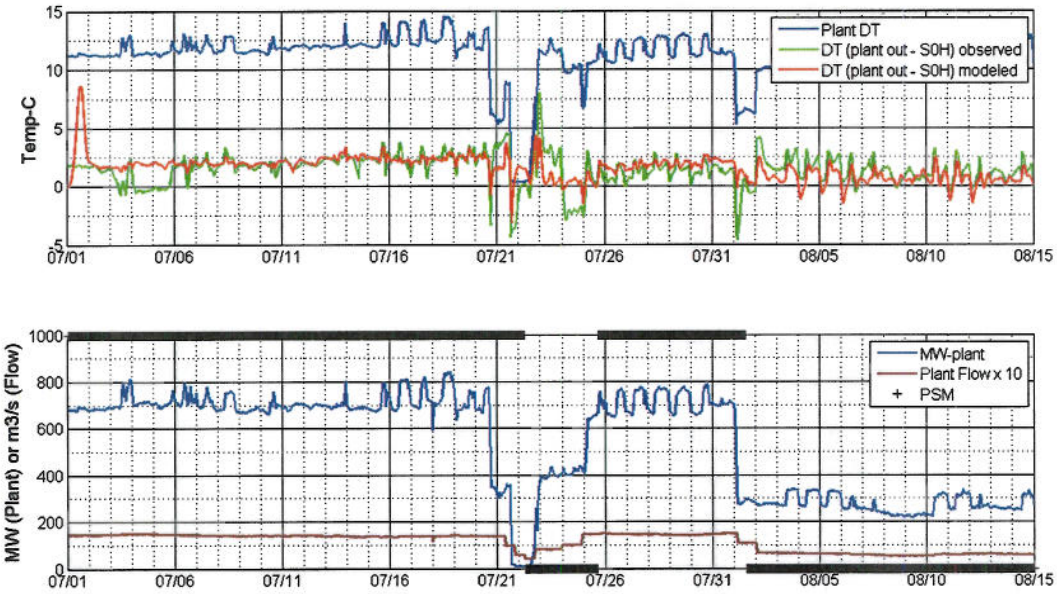

Figure 7-23. PSM model performance calibration.

7.4.2 VALIDATION

Comparisons of observed vs. simulated temperatures during the validation timeframe of 11 July through 21 July 2009 for stations N10, N5, S0, S4, S16 and A0 are shown at River locations for top, middle and bottom in the west, center and east locations in Figure 7-24 through Figure 7-29, respectively. Similar to the calibration period, these figures show that the model does well at recreating the upstream water temperatures as well as capturing the strong signal of the thermal plume at station S0, in particular the strong signal at the top and weaker signal at the bottom. Additionally these comparisons show that the model is able to simulate the vertically and laterally mixed plume well at locations south of S0 as observed.

Furthermore the model recreates the vertical structure of the water column well with good agreement between simulated and observed stratification with the exception of S0-West. The model does recreate thermal stratification at S0-West, however it overpredicts temperature in the middle of the water column, but does not overpredict the bottom temperatures significantly. While the thermal signal of the plume is also observed at S0-Center Top and even at S0-East Top, these events are episodic, such as that observed 16 July through 19 July. The environmental forcing and Station operations during this time period are quite similar to the days preceding and following this event and the model simulations respond to the forcing in a similar manner. The model is unable to recreate the temperature signal observed at S0-Center Top, and it is unclear exactly what forces are exerted to move the plume over that station. As the signal is episodic, it may be assumed that the station is located at a point on the exact edge of the plume, and that the model grid cell location does not reflect this fact accurately. Table 7-4 summarizes each of the quantitative measures at each station. As can be seen from this table the model performance during the validation time period exceeds all standards in terms of quantitative statistics.

Given that the validation period was assumed to have a greater impact on the River than the calibration period because of the greater associated heat rejections during this time period, the validation period results were compared to the ambient or background simulations in order to determine the relative impact of the plant. This was done by running a scenario using all validation period environmental forcing factors but without the plant thermal discharge, called an "environmental background" case. The differential between these two scenarios then reflects the plant thermal discharge impacts, in terms of the resulting temperature rise above ambient. Figure 7-30 through Figure 7-33 show the time series of temperature difference at the top, middle and bottom for the west, center and east locations of stations S0, S4, S16 and A0 respectively.

Figure 7-30 shows that during this time period the thermal plume from the Station is only significant (between 2 – 4.25°C [3.6 – 7.65°F] above background) at the top and middle of the west side of the River and only somewhat noticeable in terms of a temperature rise less than 0.5°C (0.9°F) above background on the surface at the center of the River at S0. The remaining thermistors along the transect show a negligible temperature rise. Further downstream at

station S4 the thermal plume has been attenuated in magnitude however it has increased in extent. Figure 7-31 shows that there was a noticeable rise in temperature above background at all locations, and was greatest at 1.8°C (3.24°F) at the surface on the west side of the River. This trend continues further downstream at station S16 with rise above background at all stations, however less than 1.5°C (2.7°F) at all locations as shown in Figure 7-32. Finally at station A0, close to the Hooksett Dam, the observed temperature rise above background at each location is similar to those seen at S16, less than 1.5°C (2.7°F) at all locations. The plume is well mixed within the water column at station A0.

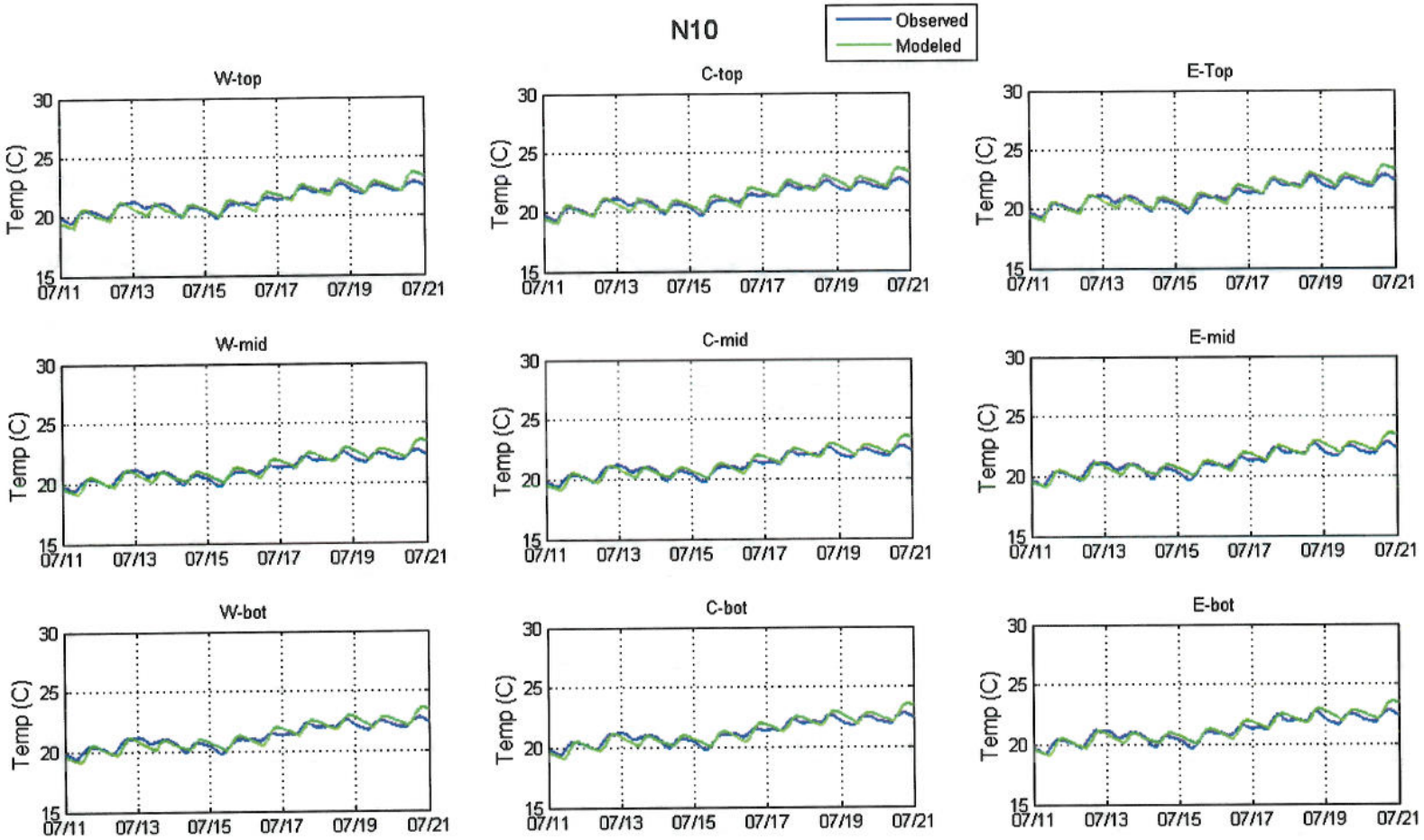

Figure 7-24. N10 observed (blue) versus model predicted temperature (green) during validation time period.

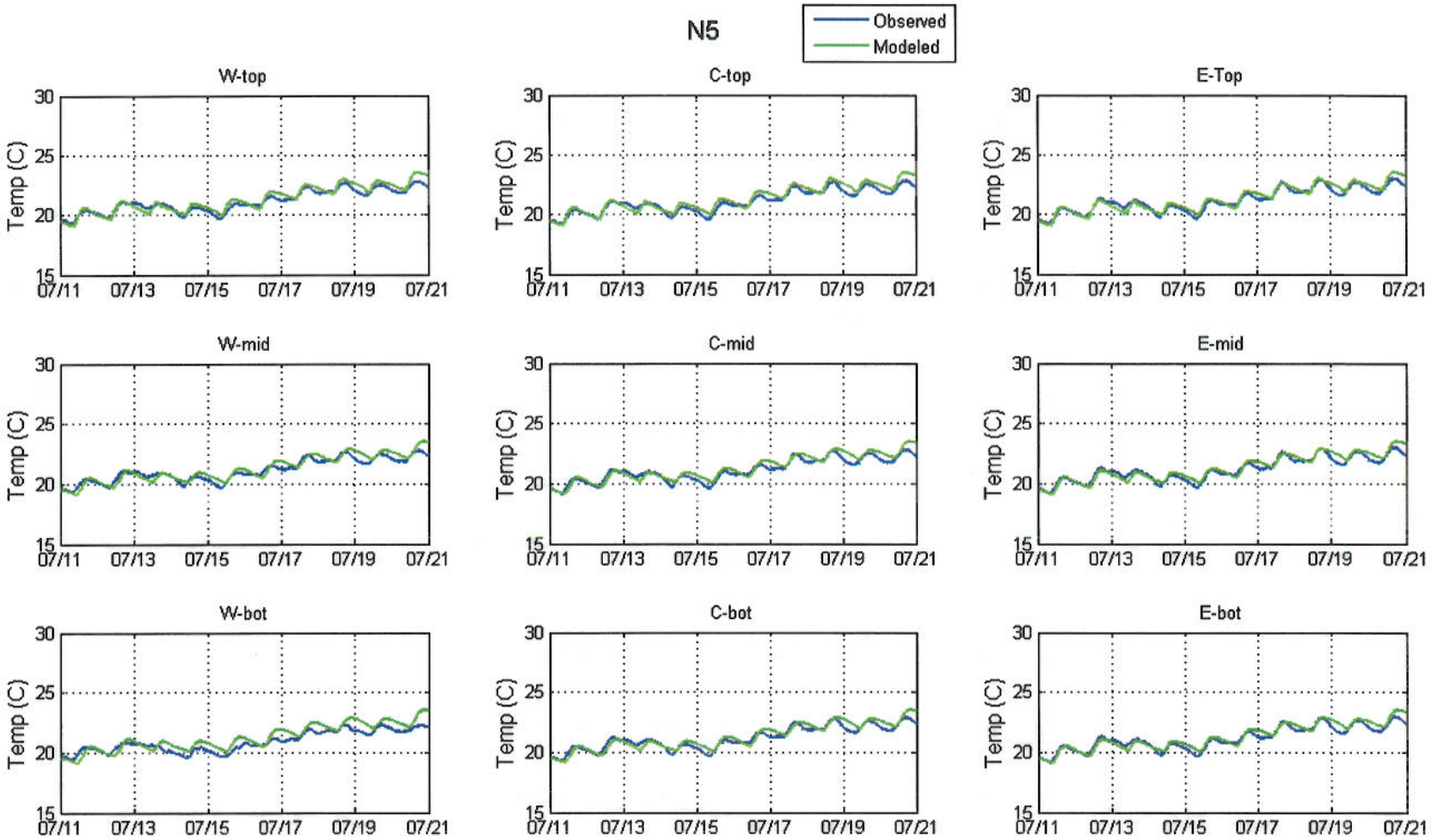

Figure 7-25. N5 observed (blue) versus model predicted temperature (green) during validation time period.

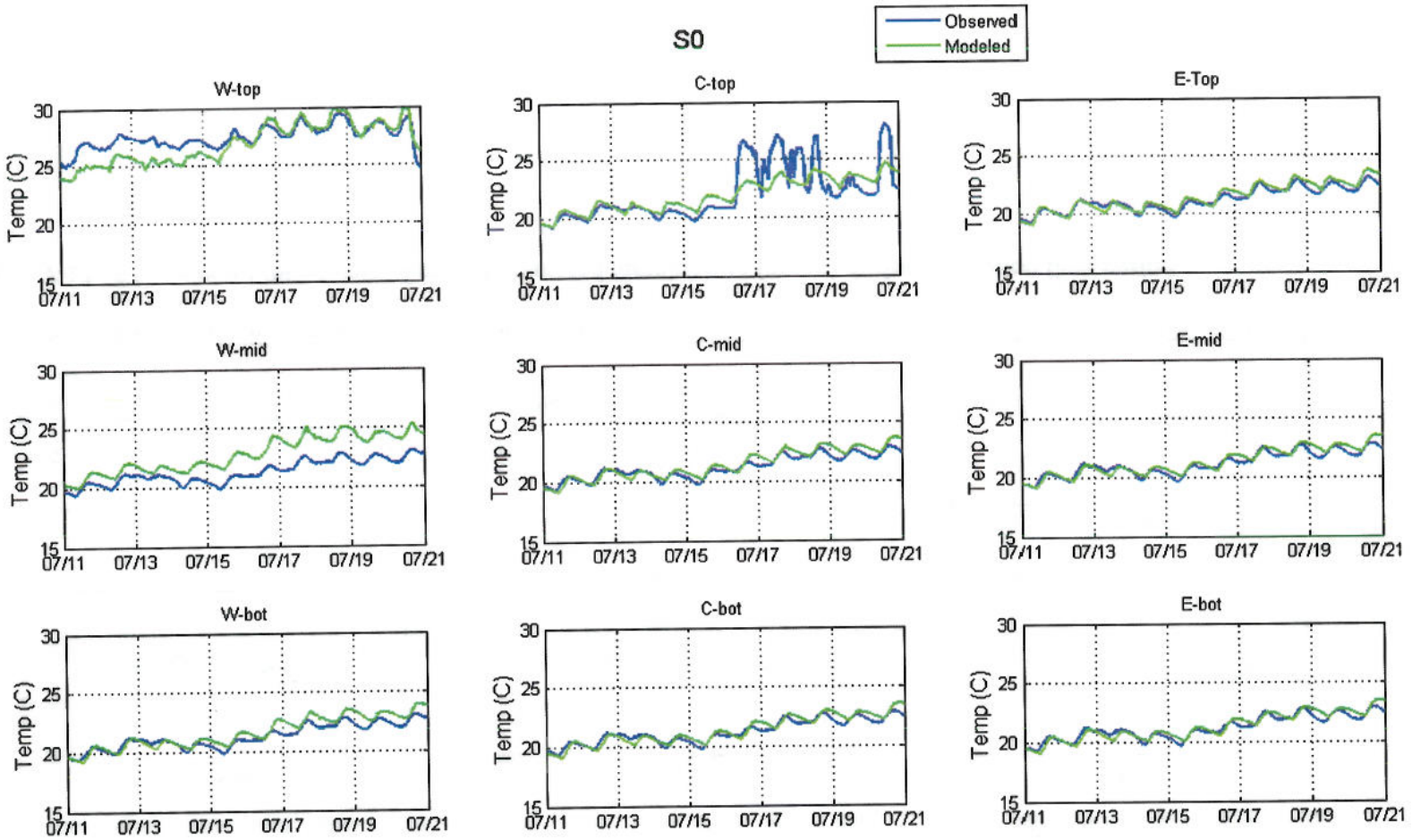

Figure 7-26. S0 observed (blue) versus model predicted temperature (green) during validation time period.

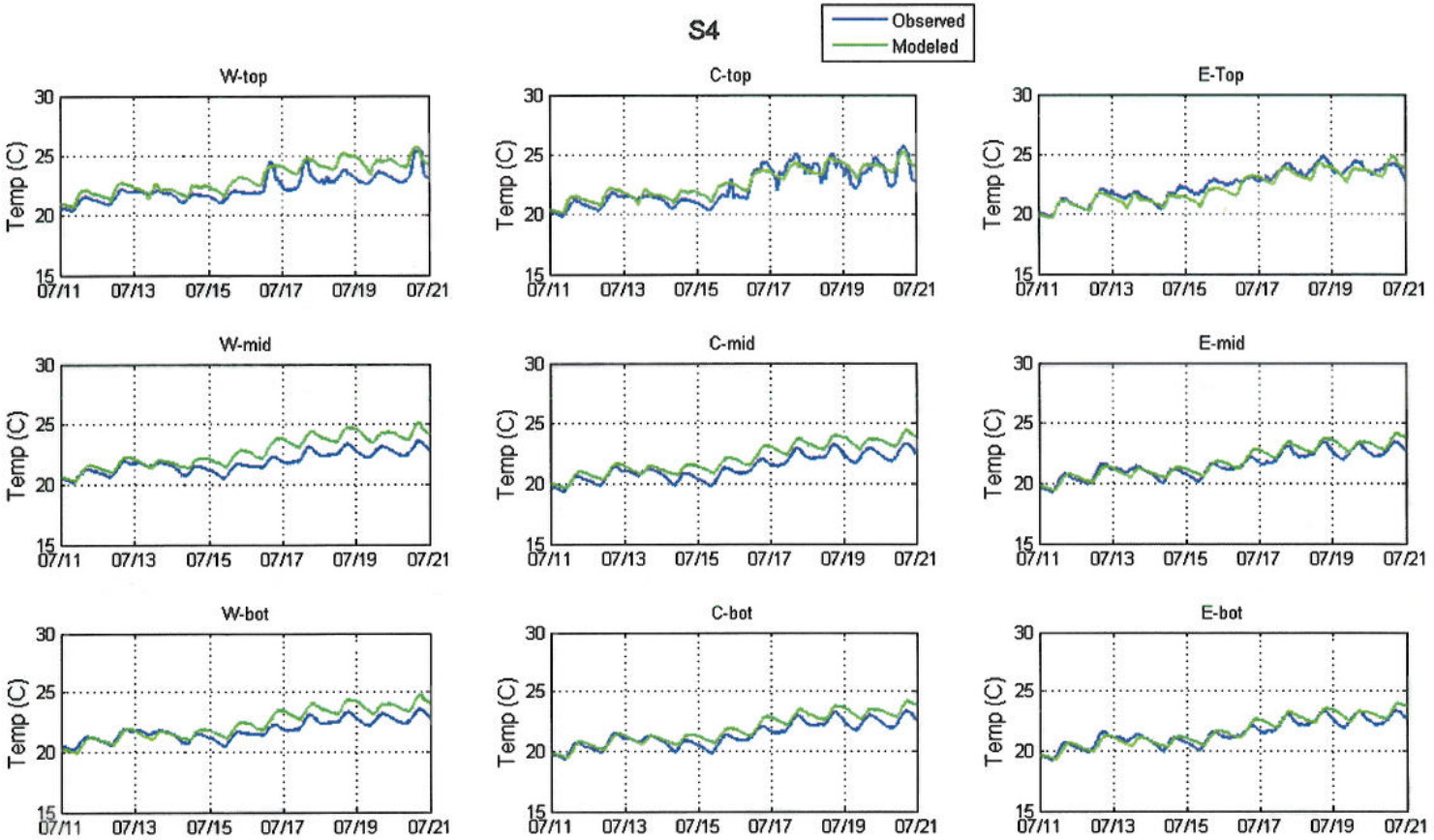

Figure 7-27. S4 observed (blue) versus model predicted temperature (green) during validation time period.

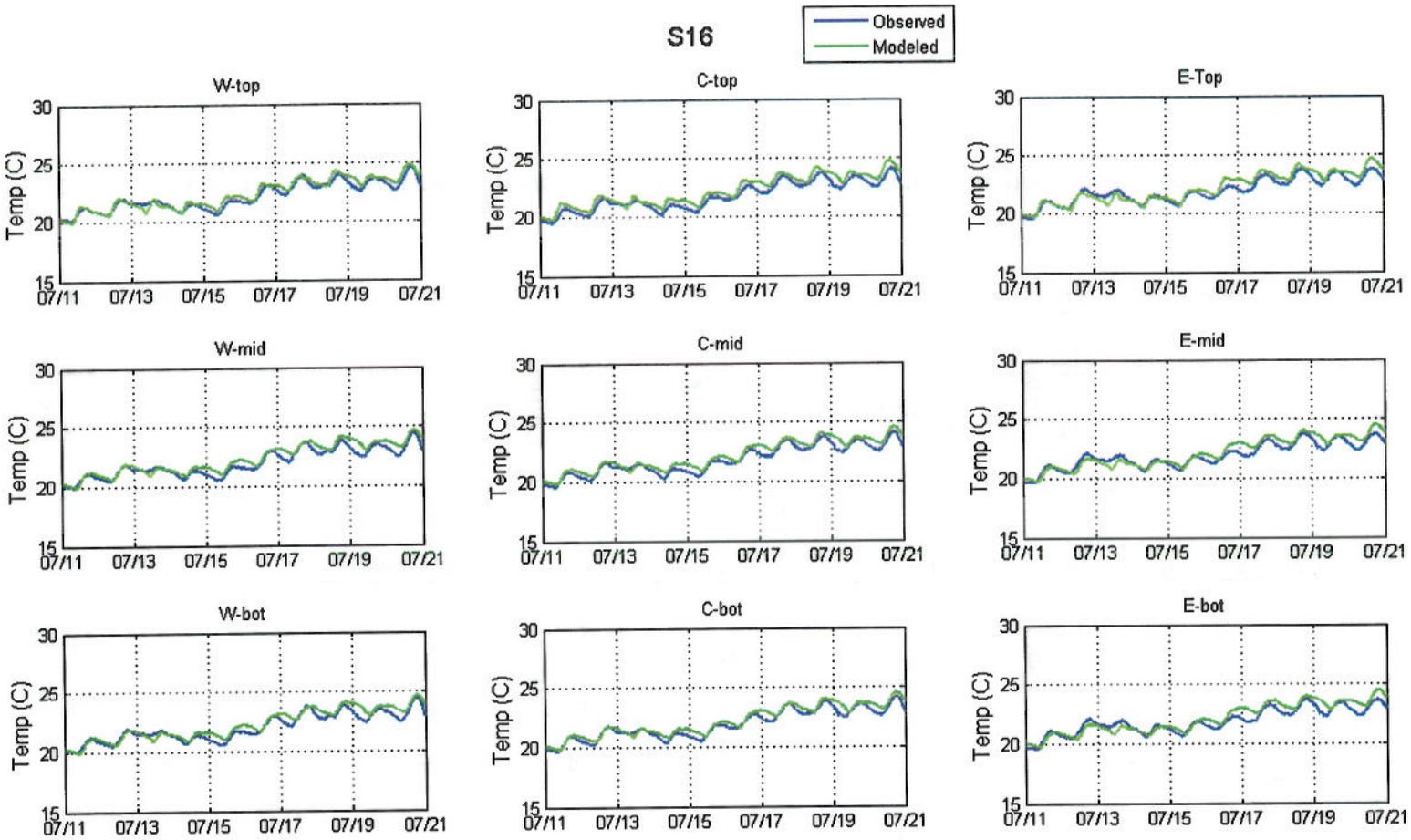

Figure 7-28. S16 observed (blue) versus model predicted temperature (green) during validation time period.

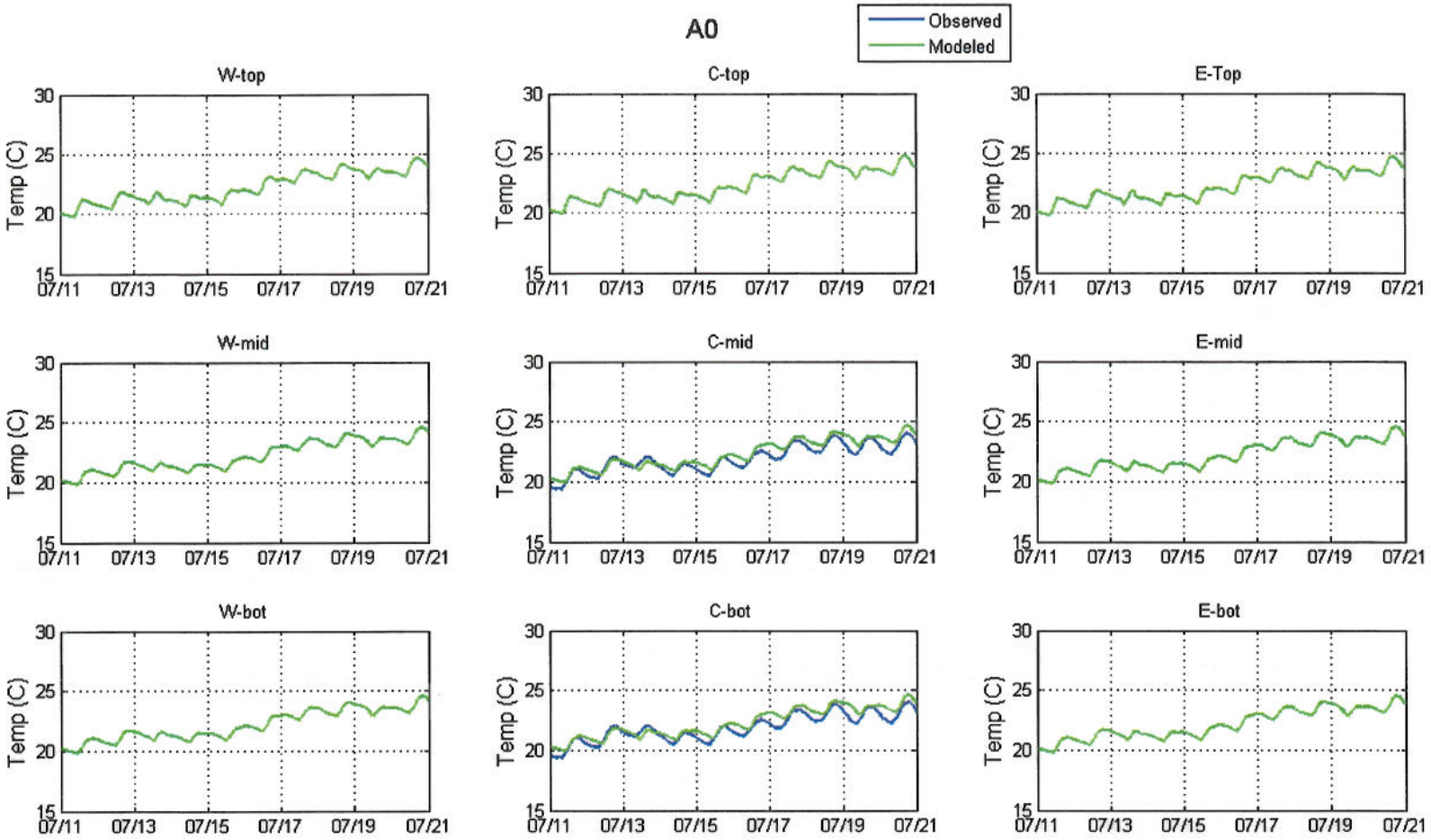

Figure 7-29. A0 observed (blue) versus model predicted temperature (green) during validation time period.

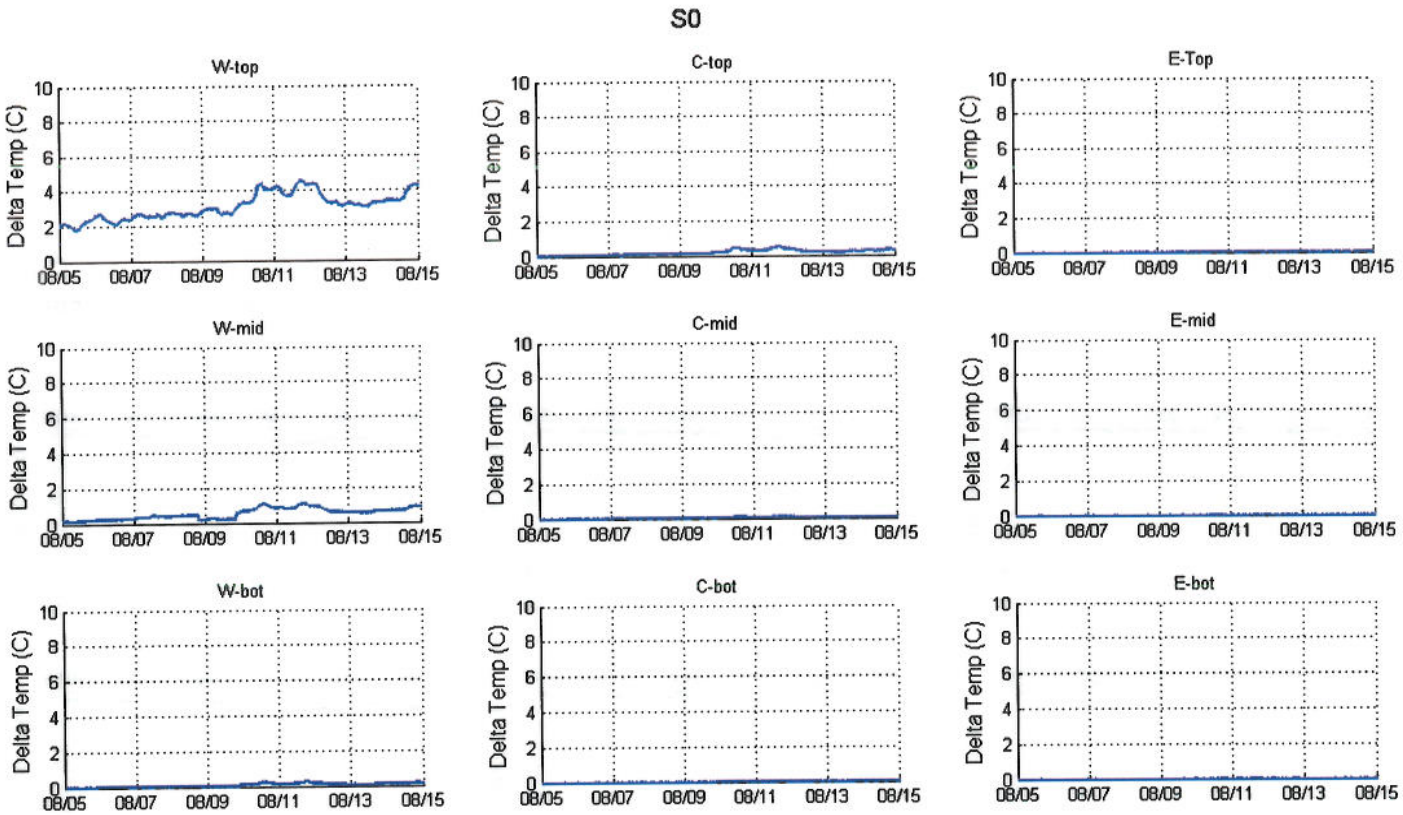

Figure 7-30. Validation Delta T at S0.

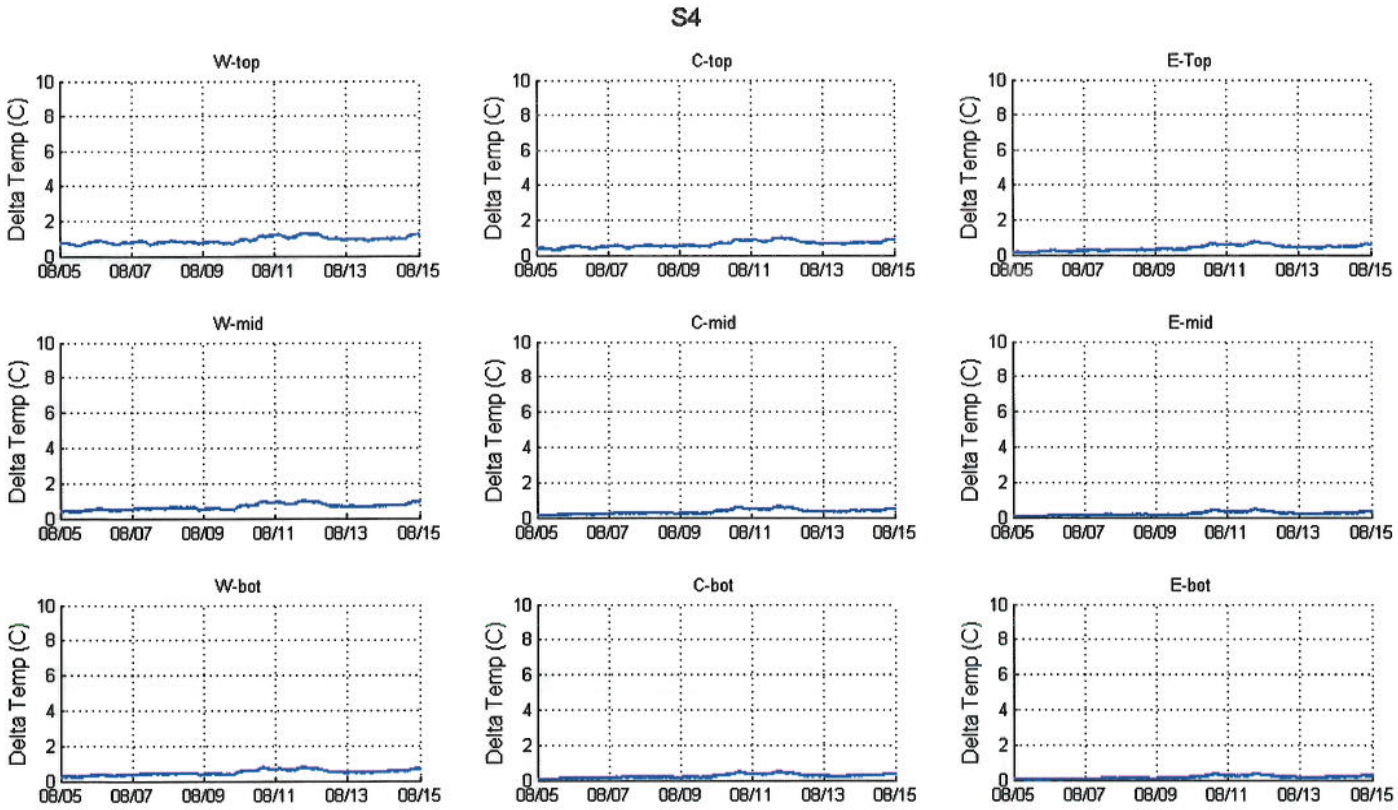

Figure 7-31. Validation Delta T at S4.

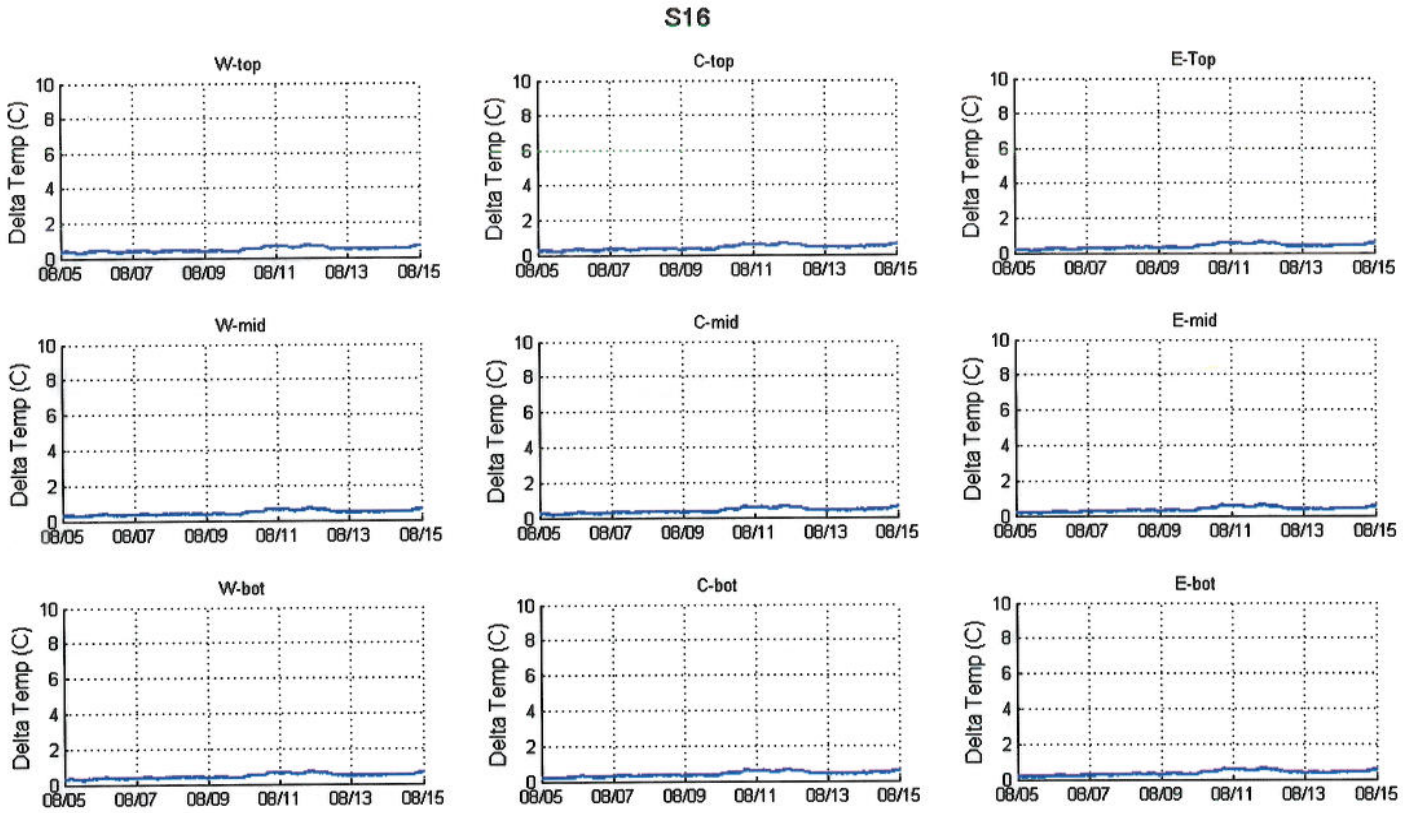

Figure 7-32. Validation Delta T at S16.

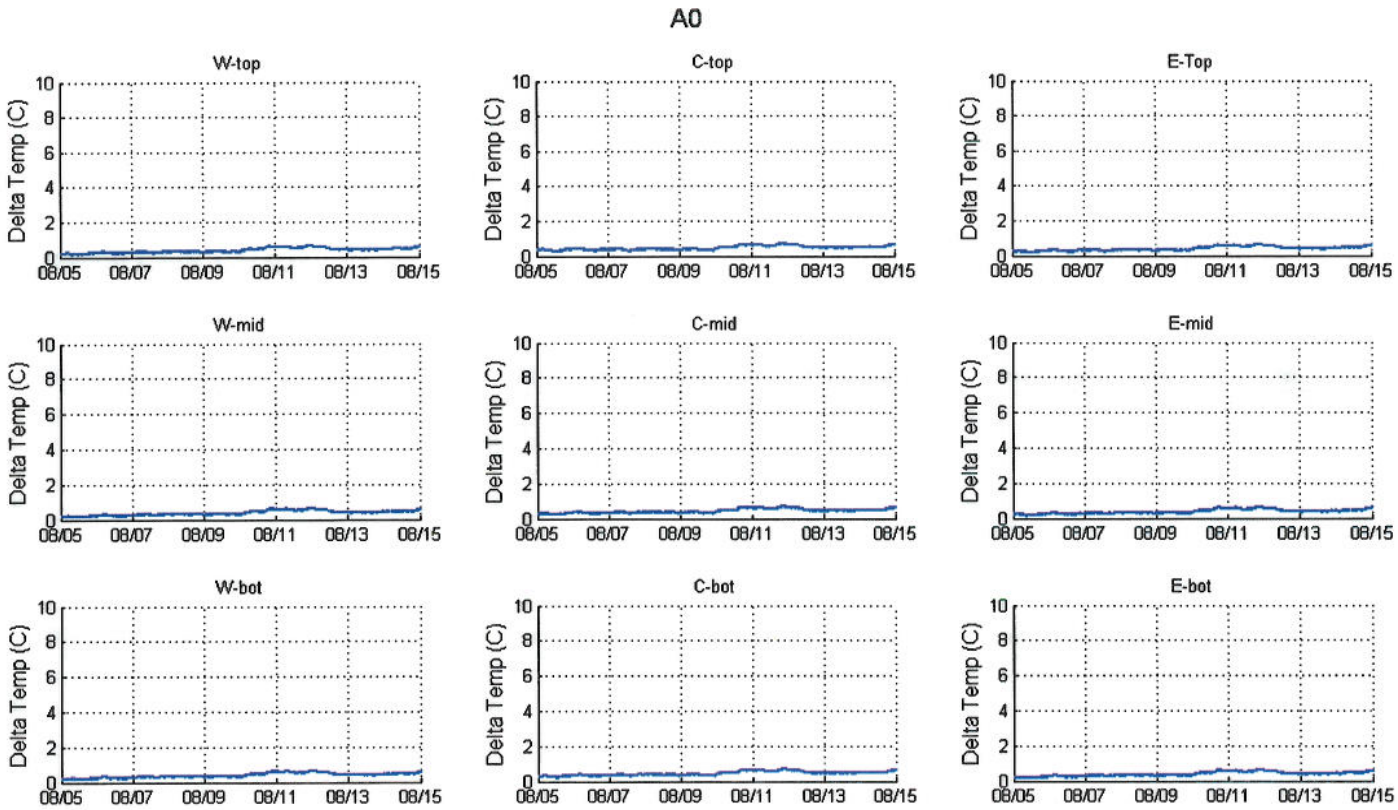

Figure 7-33. Validation Delta T at A0.

Table 7-4. Summary of validation period statistics of model predicted water temperatures.

Station	Location	Position	r^2	rme	ecv	skill
N10	West	Top	0.941	0.00%	2%	0.97
N10	West	Middle	0.941	1%	2%	0.96
N10	West	Bottom	0.941	1%	2%	0.97
N10	Center	Top	0.922	1%	2%	0.96
N10	Center	Middle	0.922	1%	2%	0.97
N10	Center	Bottom	0.922	0%	2%	0.97
N10	East	Top	0.903	0%	2%	0.97
N10	East	Middle	0.922	1%	2%	0.97
N10	East	Bottom	0.922	1%	2%	0.97
N5	West	Top	0.941	1%	2%	0.97
N5	West	Middle	0.941	1%	2%	0.97
N5	West	Bottom	0.884	2%	3%	0.91
N5	Center	Top	0.884	1%	2%	0.96
N5	Center	Middle	0.922	1%	2%	0.96
N5	Center	Bottom	0.941	1%	2%	0.97
N5	East	Top	0.846	0%	2%	0.95
N5	East	Middle	0.903	0%	2%	0.97
N5	East	Bottom	0.941	1%	2%	0.97
S0	West	Top	0.723	-2%	4%	0.82
S0	West	Middle	0.941	3%	4%	0.87
S0	West	Bottom	0.960	1%	1%	0.98
S0	Center	Top	0.578	3%	8%	0.79
S0	Center	Middle	0.922	1%	2%	0.95
S0	Center	Bottom	0.922	0%	2%	0.97
S0	East	Top	0.903	2%	3%	0.91
S0	East	Middle	0.903	1%	2%	0.96
S0	East	Bottom	0.922	0%	2%	0.97
S4	West	Top	0.828	4%	4%	0.84
S4	West	Middle	0.903	4%	4%	0.81
S4	West	Bottom	0.903	2%	3%	0.89
S4	Center	Top	0.846	2%	3%	0.93
S4	Center	Middle	0.922	4%	4%	0.87
S4	Center	Bottom	0.922	2%	3%	0.93
S4	East	Top	0.903	0%	2%	0.97
S4	East	Middle	0.903	2%	2%	0.95
S4	East	Bottom	0.903	1%	2%	0.96
S16	West	Top	0.941	1%	2%	0.98
S16	West	Middle	0.941	1%	2%	0.97
S16	West	Bottom	0.941	1%	2%	0.98
S16	Center	Top	0.960	2%	3%	0.95
S16	Center	Middle	0.960	2%	2%	0.97
S16	Center	Bottom	0.960	1%	2%	0.98
S16	East	Top	0.884	2%	2%	0.94
S16	East	Middle	0.884	1%	2%	0.95
S16	East	Bottom	0.884	1%	2%	0.95
A0	West	Top	0.884	1%	2%	0.95
A0	West	Middle	0.903	2%	2%	0.95
AVERAGE			0.904	1%	2%	0.94
GUIDANCE			0.840	25%	2%	0.85

8 EXTREME CASE SCENARIO SIMULATION

In order to understand what the maximum thermal impacts of the Station effluent is on the River, an extreme case scenario was developed. There were two parts to this scenario simulation: development of the simulation time frame and extreme conditions, and then model simulations and post processing. The model simulations utilized the previously calibrated and validated model with modified forcing to reflect the extreme case scenario time frame. The scenario timeframe was selected to represent a combination of simultaneously occurring extreme environmental forcing conditions such as high air temperatures, high water temperatures, low river flows and high Station output. Furthermore, the scenario time period was run for two cases: one with the Station operating at maximum capacity (800 MWt (2730 Btu/hr) of rejected heat at 10.31 m^3/s (364 cfs) cooling water flow) and the other without the Station in operation to generate the environmental background. The Model results were then further processed to obtain the temperature differential between the two cases for each cell in the Model domain at every time step of the simulation period. This "deltaT" defines the relative Station thermal impacts to the River.

8.1 DEVELOPMENT OF EXTREME CASE SCENARIO TIMEFRAME

The goal of developing each scenario timeframe was to capture environmental conditions in which the Station thermal discharge exhibits the greatest spatial extent in the River. A review of the observed water temperature at the historical N10 (N10H) transect along with observed air temperatures and solar radiation at Concord Airport was performed from which the period of 24 July through 3 August 2007 was identified as a period of consistently high river and air temperatures with strong solar radiation.

8.2 EXTREME CASE SCENARIO FORCING

The boundary forcing for the scenario Model simulation was set up similar to that of the calibration and validation timeframe, however it was adjusted where data was not available to generate the required forcing.

8.2.1 LOWER RIVER BOUNDARY AT HOOKSETT DAM

Similar to the calibration and timeframe simulations the downstream boundary was forced with surface elevation and water temperatures. Observed surface elevation data during the scenario timeframe was not available and therefore was estimated based on a relationship developed between river flow and surface elevation during 2009. Using this relationship the surface elevation for the scenario period was estimated as a function of the river flow. Figure 8-1 illustrates the relationship between 2009 River flow and Pool elevation as well as the linear trend line fit to the data which was subsequently used to estimate elevation based on river flow during the scenario timeframe. The downstream temperatures were assumed equal to N10H

during the scenario timeframe. Figure 8-2 illustrates the River flow and temperature during the scenario timeframe. During the scenario period the downstream surface elevation varied between –0.3 m to -0.25 m (-1 to 0.82 ft), with daily variability approximately 0.02 m (0.07 ft.). During this time period the water temperature ranged from 22 to 28°C (71.6 – 81.4°F).

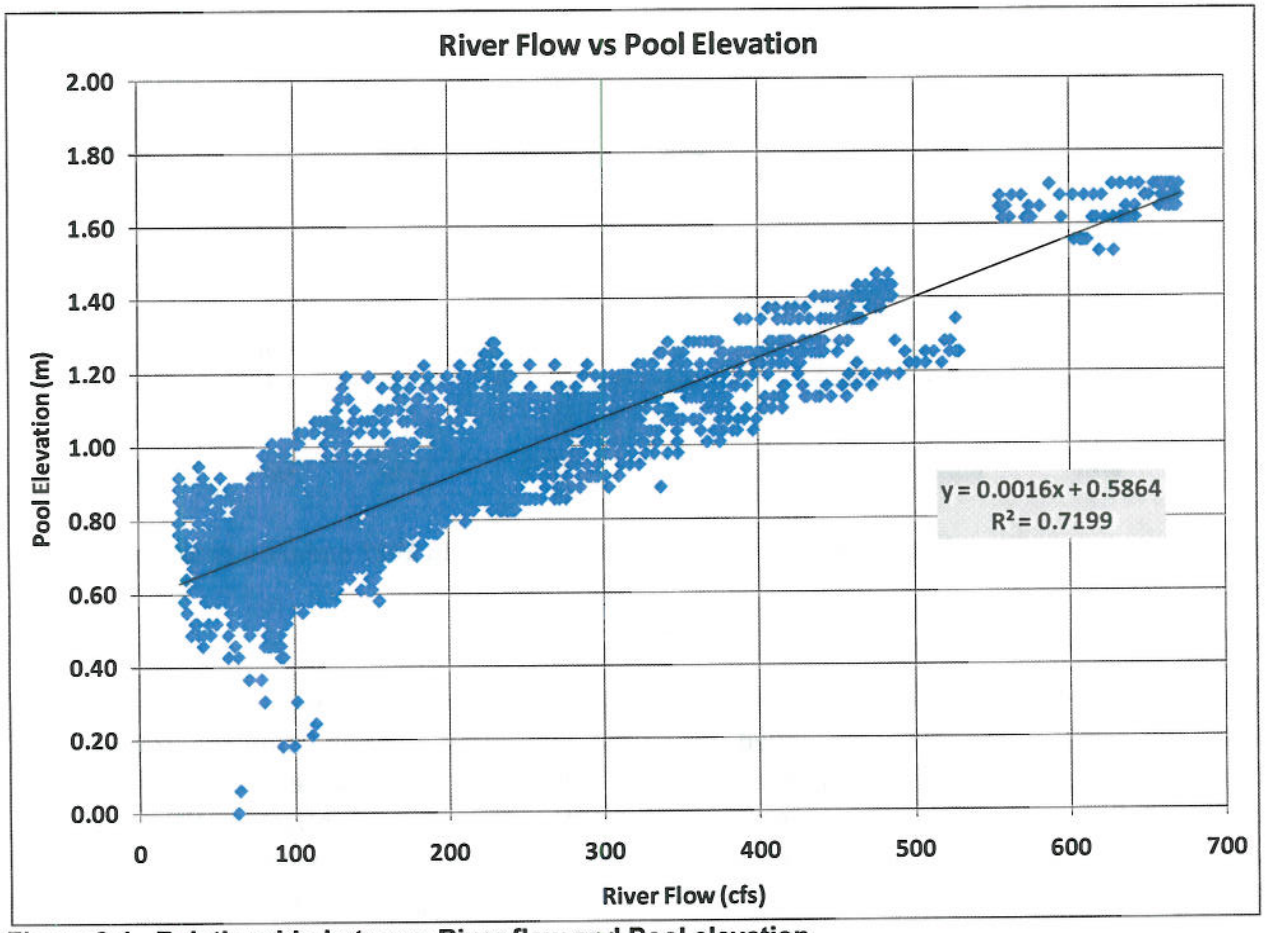

Figure 8-1. Relationship between River flow and Pool elevation.

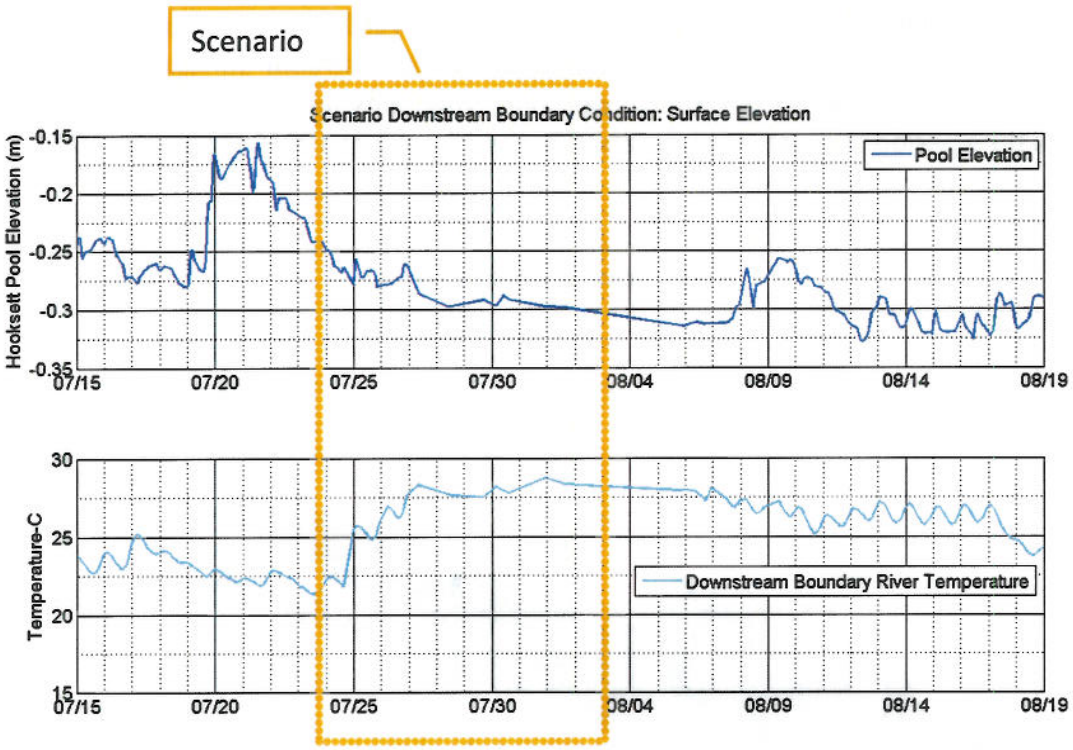

Figure 8-2. Lower River boundary forcing at Hooksett Dam during 2007 scenario timeframe.

8.2.2 Upper River Boundary at Garvins Dam

The upstream boundary forcing consisted of time varying river flow and water temperature using the same methodology employed during the calibration and validation timeframe. This consisted of estimating flow using the previously developed statistical relationships based on observed flow and observed temperatures at N10H. The 15 hour offset in time was also applied to the forcing to account for travel time down the upstream portion of the River. Figure 8-3 shows the upstream River boundary flow and temperature for the scenario time period. During the scenario period the upstream River flow ranged from 35 – 70 m^3/s (115 – 230 cfs) and the River temperatures ranged from 22 to 28°C (71.6 – 81.4°F).

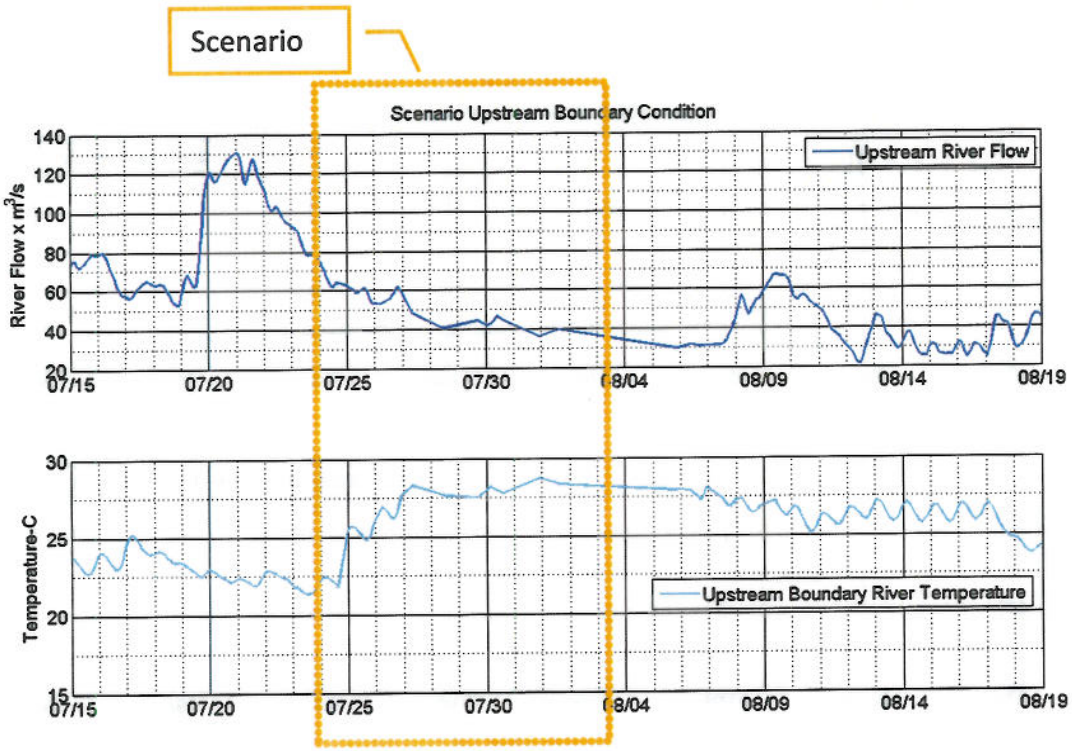

Figure 8-3. Upper River boundary forcing at Garvins Falls during 2007 scenario timeframe.

8.2.3 Suncook River Tributaries

The boundary forcing representing the Suncook tributary inputs consisted of time varying river flow and water temperature using the same methodology employed during the calibration and validation timeframe. This consisted of estimating flow using the previously developed statistical relationships based on observed flow and observed temperatures at N10H. The 15 hour offset in time was also applied to the forcing to again account for travel time down the upstream portion of the River. Figure 8-4 shows the Suncook tributary boundary flow and temperature for the scenario time period. During the scenario period the upstream flow ranged from 2.5 – 4 m^3/s (8 – 13 cfs) and the temperatures ranged from 22 to 28°C (71.6 – 81.4°F).

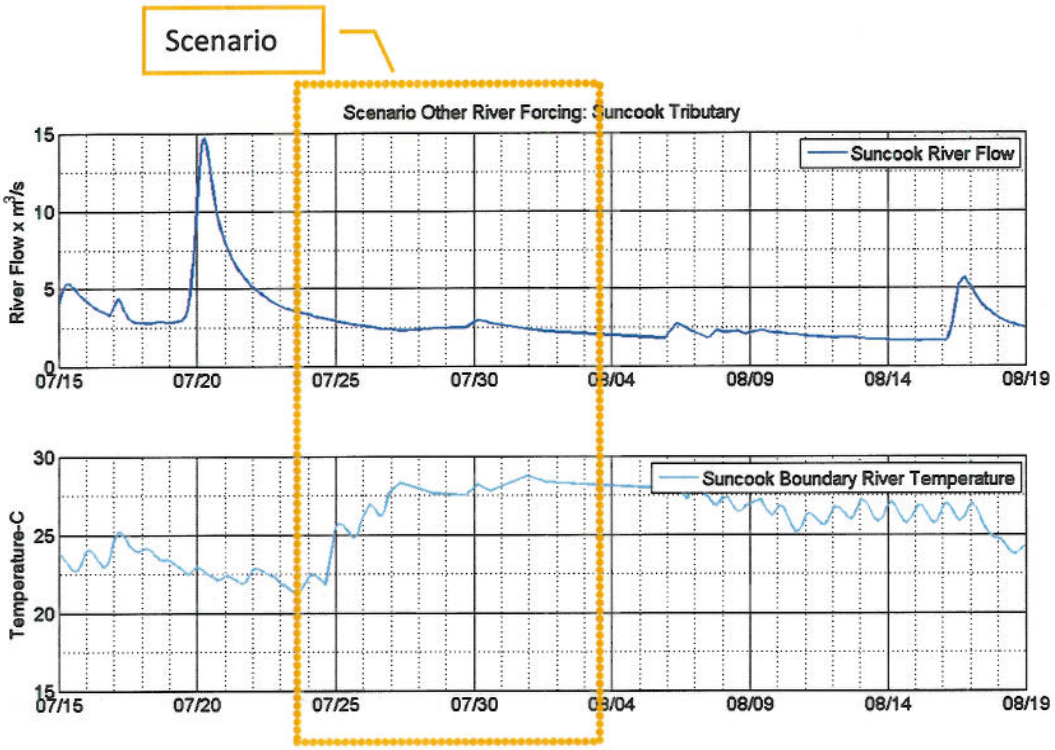

Figure 8-4. Suncook River boundary forcing during 2007 scenario timeframe.

8.2.4 Meteorological Conditions at Concord

The meteorological forcing during the scenario timeframe was developed in the same manner as during the calibration and validation timeframe. Observations from Concord airport were used to develop the forcing inputs and are presented in Figure 8-5 for the scenario period.

The air temperature during the scenario period had a diurnal signal that varied between 15 - 34°C (59 – 93.2°F). The dew point had a much smaller diurnal range though it followed the air temperature trends ranging from 13 - 22°C (55 – 72°F). The relative humidity varied from 35 to 97%, tracking the signal of solar radiation closely where higher values occur when there is little or no solar radiation.

The wind is shown as a vector with its length scaled to the speed and its direction pointing downwind (oceanographic convention). The wind during the scenario timeframe was generally weak, between 0 - 10 knots (0 - 11.5 mph), and variable in direction. Atmospheric pressure varies between 998 and 1009 mbar and solar radiation peaked at approximately 850 W/m^2 and consistently peaked over 800 W/m2 during the scenario time period.

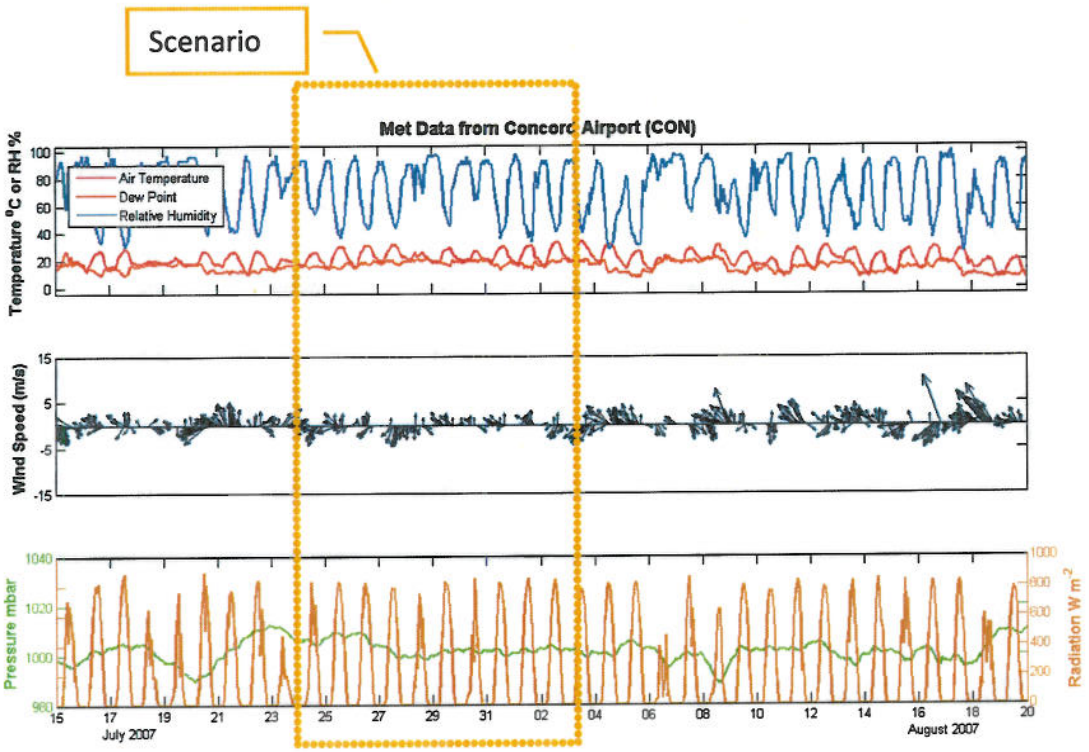

Figure 8-5. Meteorological observations during 2007 scenario timeframe.

8.2.5 Station Thermal Discharges and Spray Module Operation

The Station forcing during the scenario timeframe was developed assuming a constant maximum potential Station heat rejection and cooling water flow. During this time frame it was assumed that the Station would reject 800 MWt (2,730 Btu/hr) of heat at 10.31 m^3/s (364 cfs) cooling water flow which equates to an 18.56°C (33°F) temperature rise of the cooling water before it is discharged into the canal. It was assumed that the Power Spray Modules were in operation during this time period.

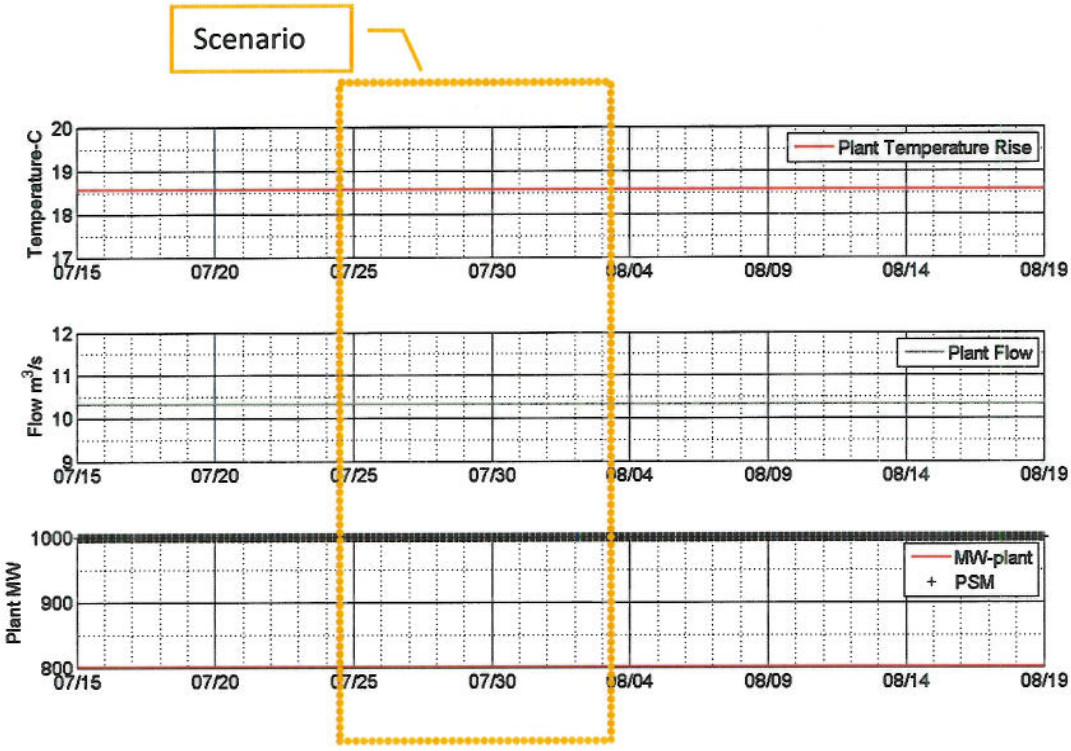

Figure 8-6. Scenario Station output during 2007 scenario timeframe.

8.3 Scenario Results

The Model was run for the scenario period both with and without Station thermal contributions. Subsequent to these model runs this set of cases were further processed to determine the delta temperature between the two cases at every grid cell for every time step. This delta demonstrates the relative thermal impact of the scenario Station thermal discharge.

Figure 8-7 through Figure 8-9 show contour plots of the delta temperature at S0, S4 and A0 respectively. These show the temperature delta in the River due to the Station at a time near the end of the scenario period. From these plots it can be seen that at S0, close to the Station, the relative thermal impacts are higher at the western side of the channel and that the plume is not yet vertically or laterally mixed. Figure 8-8 presents a plan view and cross section at S4 and shows that at S4 the plume has mixed more laterally and vertically however is not yet completely mixed across the width of the River. Figure 8-9 shows that at A0 the plume is well mixed within the water column both vertically and laterally.

Figure 8-10 through Figure 8-13 show the individual time series of scenario delta temperature for the top, middle and bottom of the west, center and east positions of station S0, S4, S16 and A0, respectively. Reviewing the figures it can be seen that the relative impact of the Station is greatest at the western side of the River near S0 and the plume increases in size while decreasing in temperature with distance from the canal. All locations within the S0 cross

section experience a temperature rise above the ambient, with the largest increase of 10°C (18°F) on the surface along the west side of the River. A temperature rise of 4°C (7.2°F) above ambient extends to depths at the middle of the water column in the vertical as well as towards the center of the River. The remaining locations at S0 have an approximate 2°C (3.6°F) increase above ambient under the scenario forcing.

Further downstream at station S4 the plume has mixed substantially, however, surface temperatures are still slightly larger than those at depth as can be seen in Figure 8-11. Overall the scenario forcing results in a 2 - 2.5°C (3.6 - 4.5°F) temperature rise above background at S4. The plume is further mixed at station S16 (see Figure 8-12) with temperature rise at all locations only slightly over 2°C (3.6°F). At station A0 (Figure 8-13) the plume is well mixed within the water column and under the scenario conditions, the corresponding temperature rise at A0 is approximately 2°C (3.6°F) in all locations.

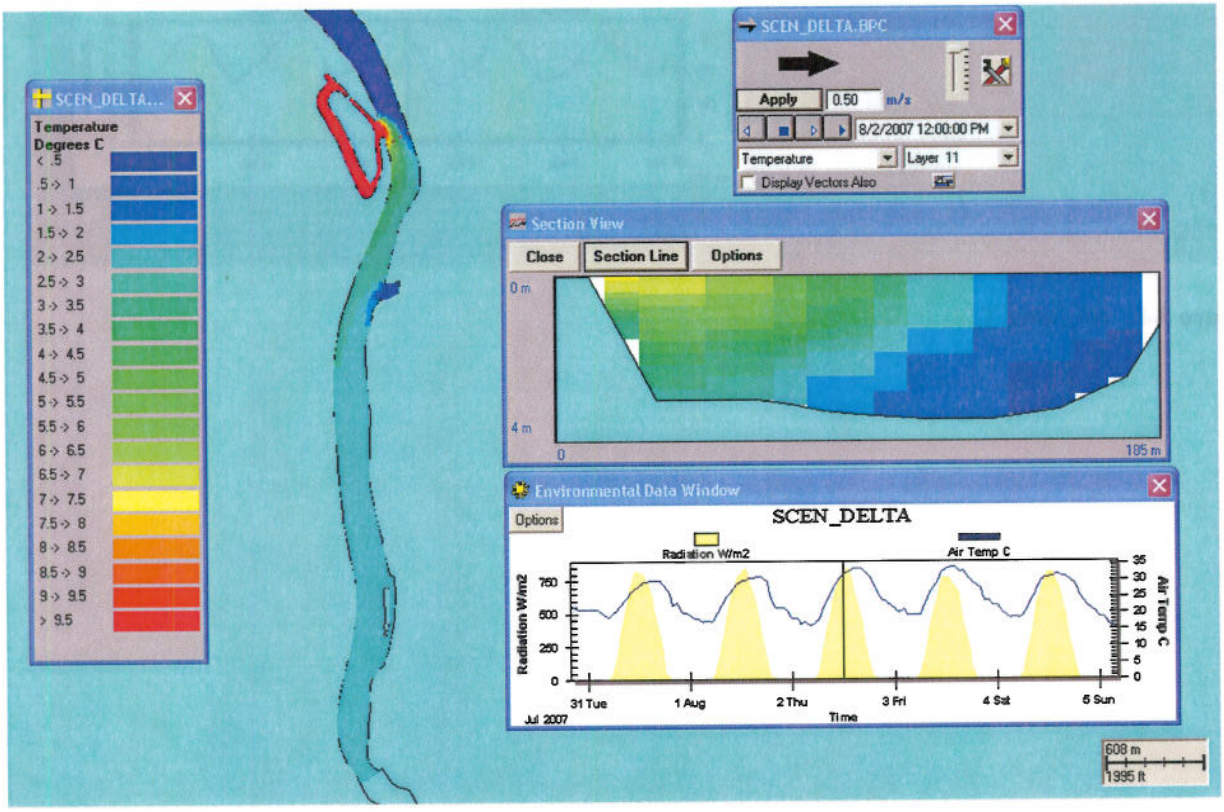

Figure 8-7. S0 Delta T.

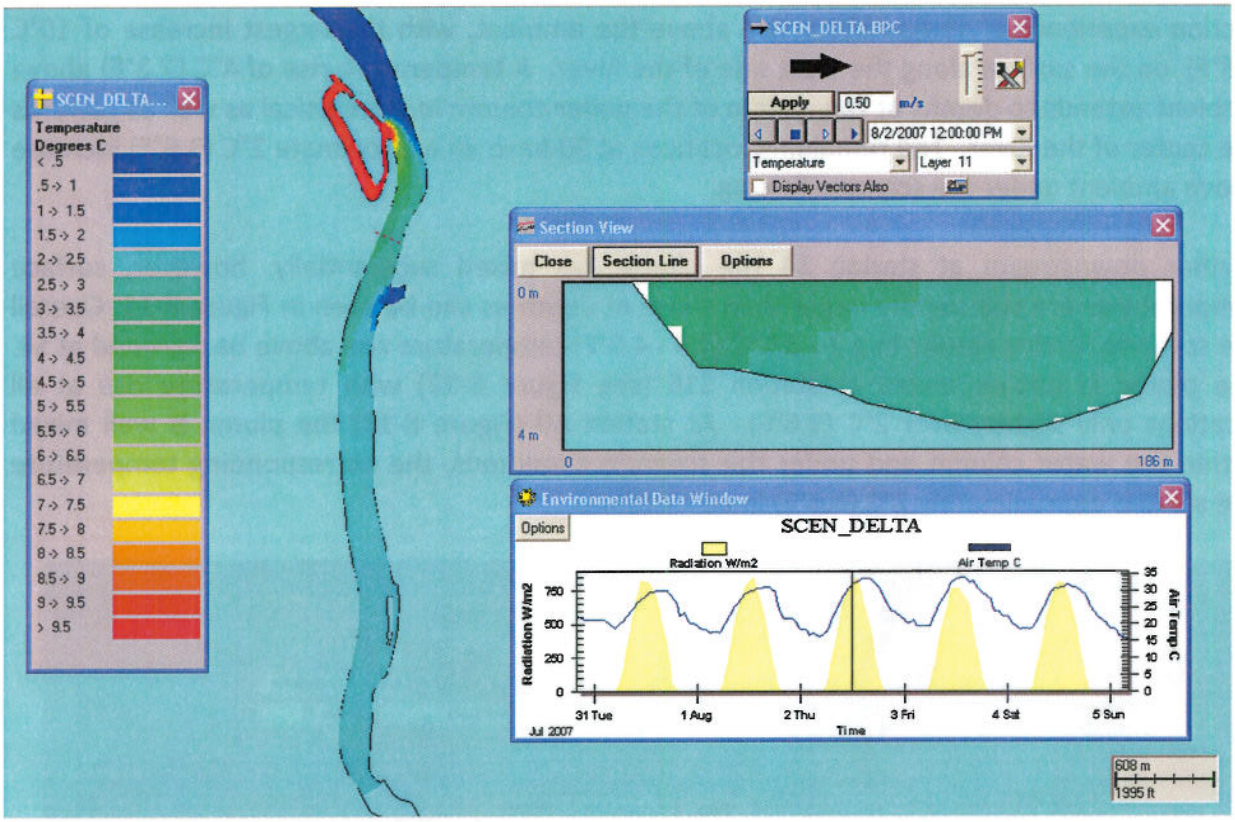

Figure 8-8. S4 Delta T.

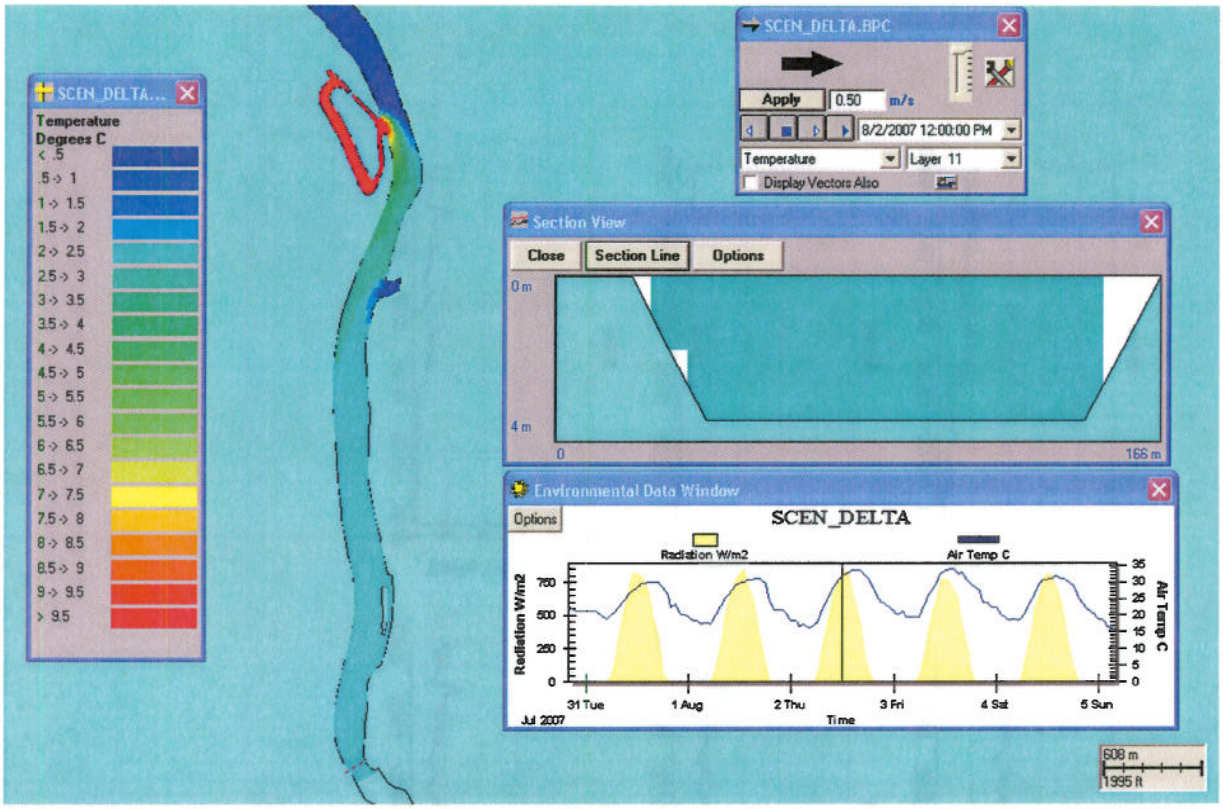

Figure 8-9. A0 Delta T.

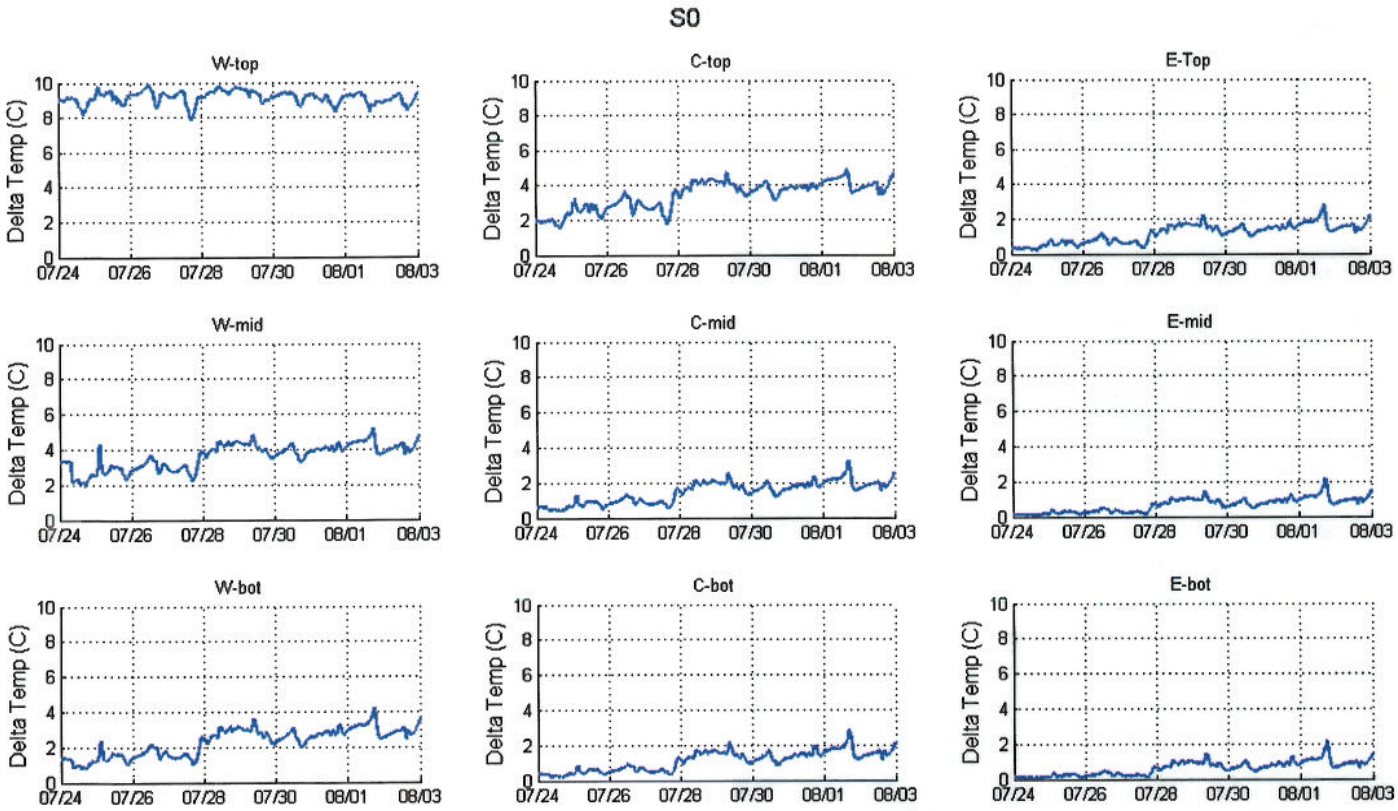

Figure 8-10. Scenario Delta T at S0.

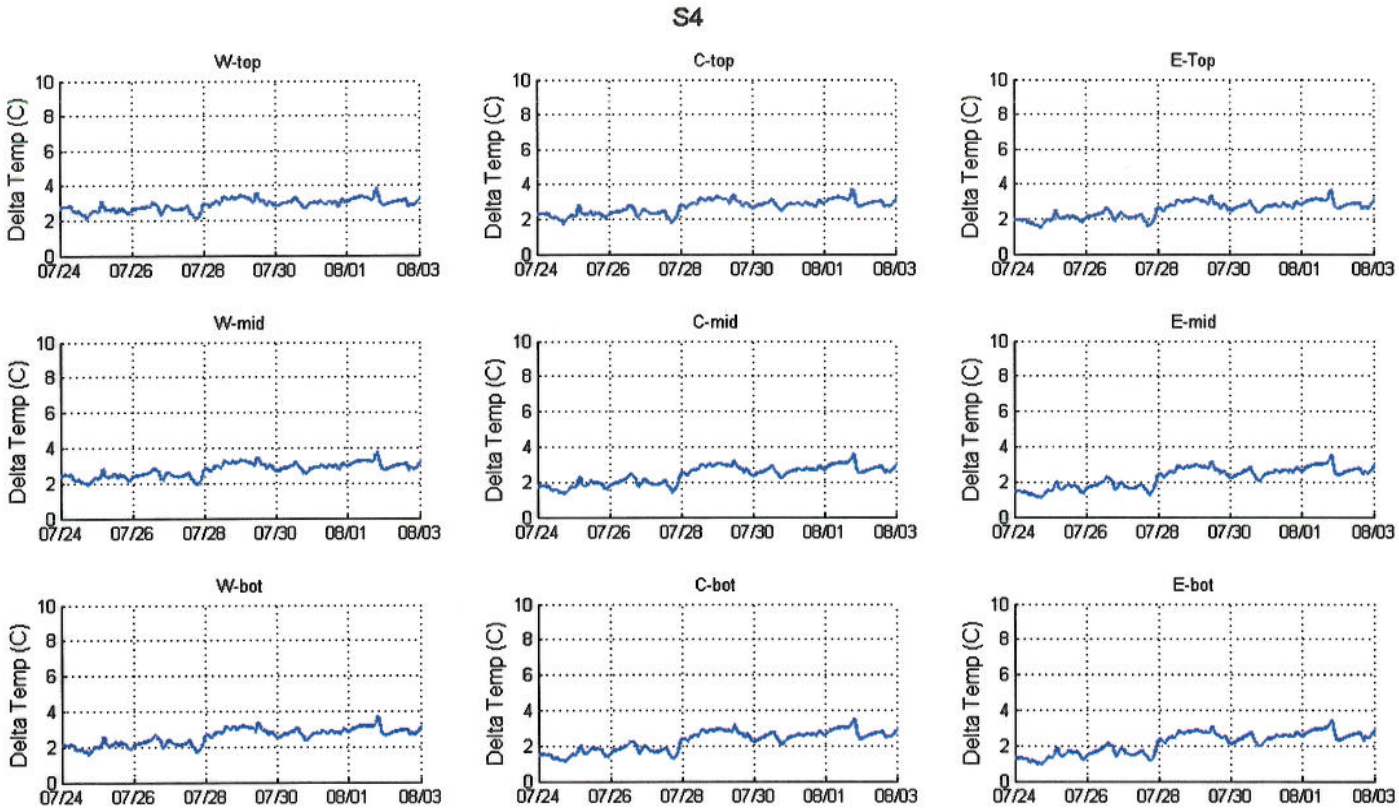

Figure 8-11. Scenario Delta T at S4.

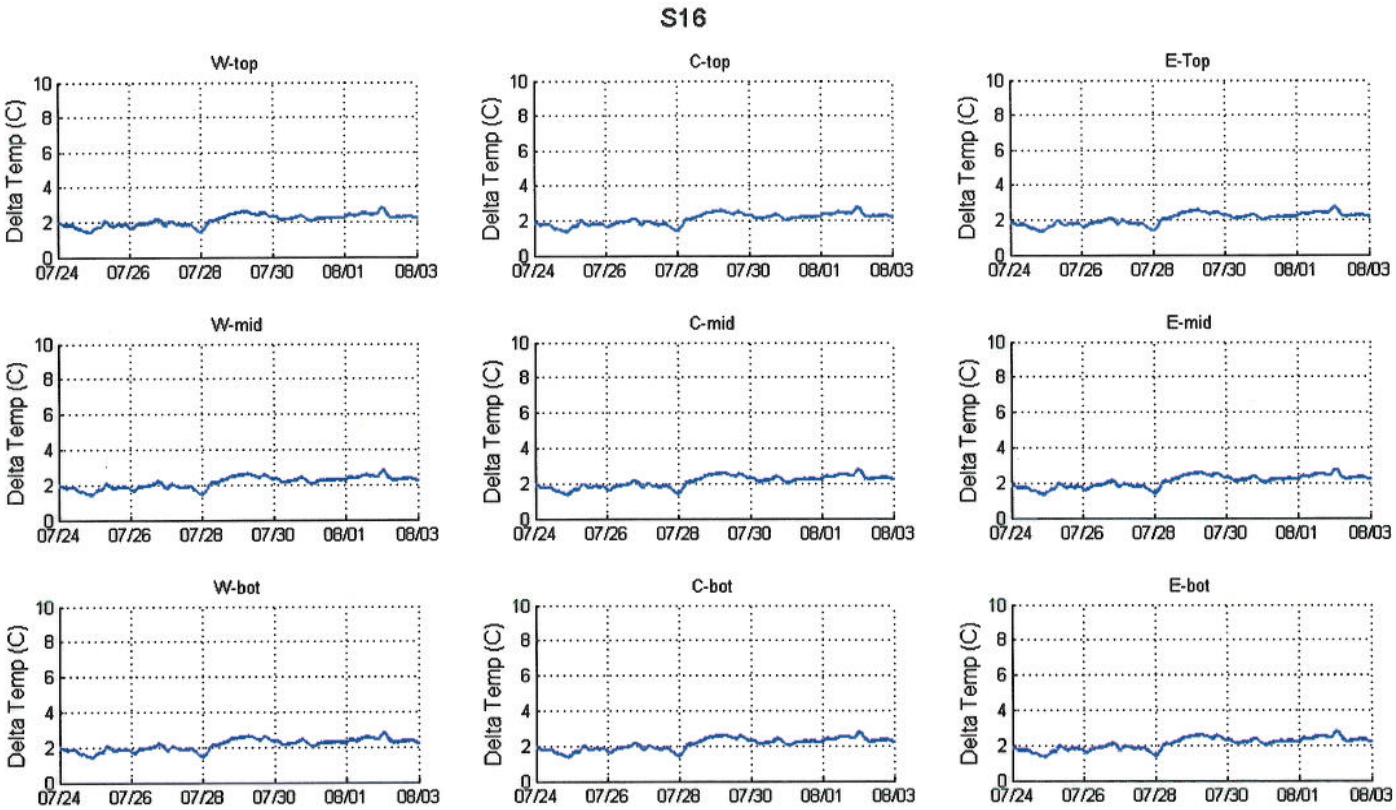

Figure 8-12. Scenario Delta T at S16.

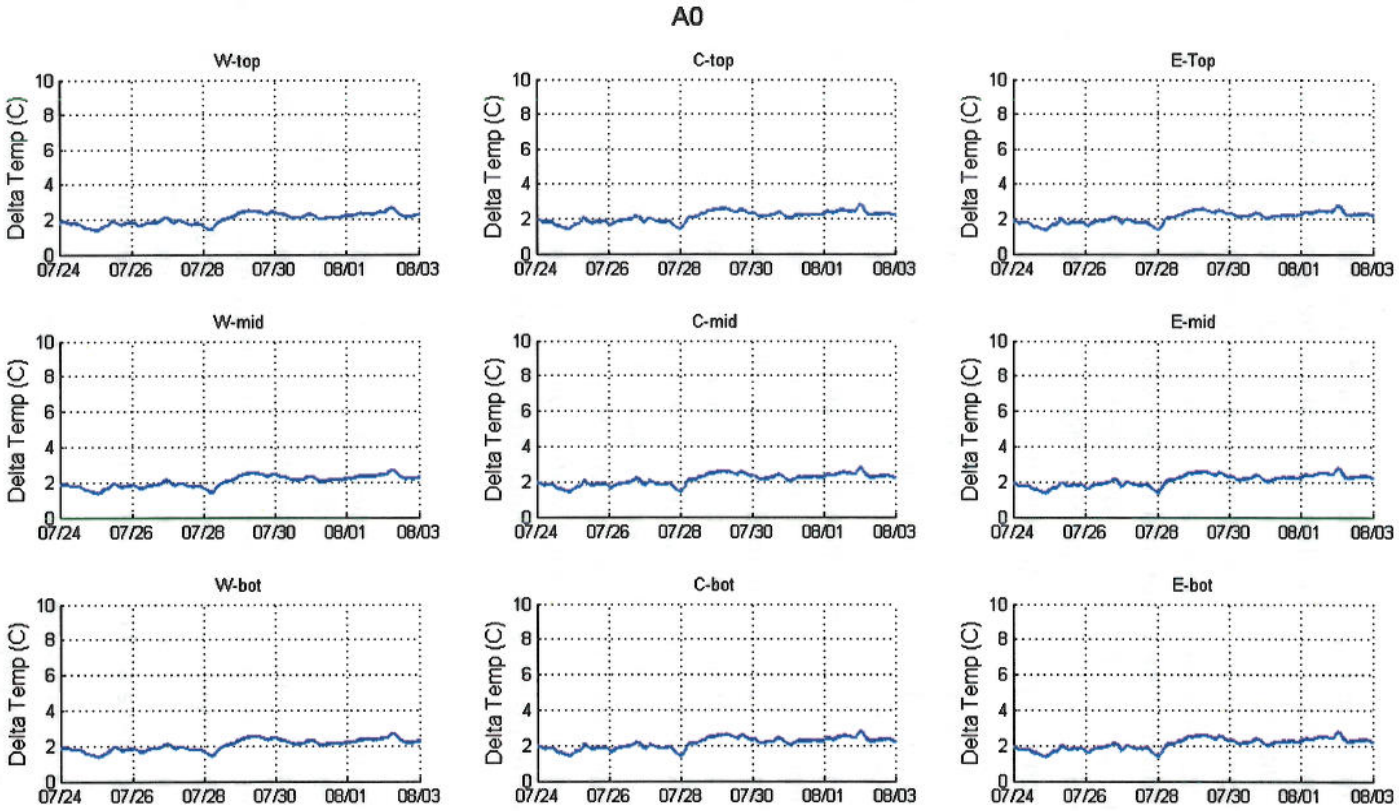

Figure 8-13. Scenario Delta T at A0.

9 CONCLUSIONS

9.1 SUMMARY

This report summarizes the methodology and findings of a data analysis and hydrothermal modeling study that focused on characterizing the thermal plume generated by a coal fired electrical generating Station utilizing river water in a once through cooling cycle to condense steam in the power generation process. The study evaluated both long and short term environmental and Station data and developed a three dimensional hydrothermal model, calibrated to the data observations. The calibrated Model was validated using the same data sources used to calibrate the Model, only for a different, independent time period. The calibration and validation procedure showed that the Model performed well, exceeding the recommended model application acceptability guidelines.

The calibrated Model was then used to simulate an extreme case to understand and evaluate the potential maximum impacts to the River from the thermal effluent. This extreme case scenario was reflective of a time period where the Station impacts were anticipated to be the greatest as measured by the extent and magnitude of temperature rise in the River. The extreme case scenario was simulated both with and without the Station thermal discharge. These two cases were then further processed to determine the temperature rise due to the Station only; this was done by subtracting the environmental background (no Station) case from the Station case for every cell for every time step. The end result of that process is a spatially and temporally varying field of model predicted Station thermal impacts in terms of a temperature increase above environmental background. This process showed that the extreme case scenario forcing would result in a well mixed water column at the Hooksett Dam that is approximately 2.0°C (3.6°F) higher than the background temperatures.

9.2 DATA ANALYSIS

The data available for the data analysis study included a long term history of three river water temperature observation stations, long term river flow estimates developed by NAI based on nearby USGS observations, long term meteorological observations from Concord Airport, short term record of Pool elevation observations, short term record of multiple (15) fixed water temperature observations at five River transects within the Pool, four days of mobile surveys (river currents) at the locations corresponding to the aforementioned River transects and observed Station data including intake and discharge temperature and estimated pump flow.

An analysis of this data showed that thermal plume was most often observed on the west side of the River close to the discharge canal as expected. In this area the observed elevated temperatures were primarily contained between the west and center of the River in the top to middle of the water column and not observed on the bottom. The most consistent location of the observed thermal plume was at S0 West Top which was the surface thermistor located on

the west side of the River at the S0 transect which is adjacent to the discharge canal, however there were some episodes where the signal observed at S0 West Top was not significant. These episodes did not have any significant environmental or Station forcing that would cause these differences and therefore it was concluded to have been caused by meanderings of the bulk flow in the river, causing the plume to meander, that was not accounted for. Similarly, there were episodes of relatively significant thermal plume response signal at S0 Center Top, S0 West Middle and S4 West Top however their occurrence was not always consistent under similar conditions again leading to the conclusion that there were some forcing mechanisms not completely understood or monitored. It was consistently observed however that the thermal plume was well mixed in both the vertical and lateral dimensions at station S16 and A0.

9.3 Model Application

Following the data analysis study, a three dimensional hydrothermal modeling study was performed, using ASA's BFHYDRO Model in WQMAP. The Model was set up to reflect the physical characteristics of the domain including geometry, river bathymetry, and appropriate boundaries located where Model forcing could be applied. The Model input forcing, driving the circulation and temperature response in the River, included river flow, water surface elevation, temperature and winds while solar radiation and auxiliary parameters, such as air and dew point temperature, relative humidity and pressure, as well as Station thermal discharge and flow properties play an important role in determining the thermal field.

For periods of high temperatures the Station employs a power spray module (PSM) system to cool the effluent plume in the discharge canal before emptying into the river. In order to simulate the cooling effects of the spray modules, an analytical model of the module performance was implemented in the BFHYDRO model system. The implementation of the spray module system for this application was tested during the Model calibration assessment and proved to be robust.

The Model was calibrated and validated successfully and was able to recreate the trend and general magnitude of observed currents. The Model was also able to recreate the observed upstream water temperatures, forced only by the environmental meteorological condition as well as capture the strong signal of the thermal plume at station S0, in particular the strong signal at the top and weaker signal at the bottom. Furthermore, the Model was able to simulate the observed vertically mixed plume well at locations south of S0 as well as the vertical structure of the water column which matches the observations in that on a regular basis there is little vertical variability in temperature with the exception of S0-West Top. Finally, the Model was able to simulate the enhanced cooling of the PSMs which was validated using historical temperature observations in the canal during both PSM on and off time periods. All of the guidance criteria for adequate model calibration and validation based on quantitative statistical measures were exceeded.

9.4 Extreme Case Scenario

After successful calibration and validation, the Model was used to simulate an extreme case scenario. The scenario time period was reflective of conditions that would result in the greatest impact of the Station, meaning a time where the combination of environmental (low river flow, high air and water temperatures) and Station forcing (maximum heat rejection of 800 MWt) were such that the River would see the highest increase in temperature. The scenario timeframe selected was 24 July through 3 August 2007. The scenario was run both with and without the Station thermal effluent, and then subsequently the results of these two cases were post processed to determine the differential in these cases, thus isolating the temperature rise due to Station loading.

This set of runs and analysis showed that under this extreme case condition the thermal plume behaves similarly in distribution as it did during the calibration and validation timeframes however that the overall temperature rise is much greater due to the high heat rejection and low thermal capacity of the environment. The temperature rise, above the environmental background conditions, due to the Station operation ranged from 7°C (12.6°F) at station S0 West down to approximately 2°C (3.8°F) of well mixed waters down at station A0, close to the Hooksett Dam. It should be noted that the process of determining the temperature rise attributable to the Station was also performed on the validation scenario, as it was a more stringent (higher heat rejection) timeframe than the calibration time frame. The results of that case showed that similar to the extreme case, the location of the plume most often at S0 West and that the plume was again vertically mixed downstream, however the 2009 summer conditions modeled only resulted in a temperature rise of less than 1.5°C (2.7°F) at station A0, close to the Hooksett Dam as opposed to the 2°C (3.8°F) rise experienced under extreme case conditions.

10 REFERENCES

Adriance, W.R., 2010. Joint Application for CWA § 401 Water Quality Certification NRC License Renewal – Entergy Nuclear Indian Point Units 2 and 3 DEC Nos.: 3-5522-00011/00030 (IP2) and 3-5522-00031 (IP3) *Notice of Denial*. Letter from Division of Environmental Permits, New York State Department of Environmental Conservation to Dara F. Gray, Entergy Nuclear Operations, Inc., Buchanan, NY, 2 April 2010.

Crowley, D.J. and D.L. Mendelsohn. Ras Tanura Integrated Project Recirculation Study. Final Report, ASA Project 09-229, Applied Science Associates, Inc., 2009

EAI (Epsilon Associates, Inc.), MRI (Marine Research, Inc.) and ASA (Applied Science Associates, Inc.), 1998. Fore River station thermal discharge technical information document. Submitted on behalf of Sithe Edgar Development, LLC, ASA Project 98-018.

Maulbetsch, J.S. and J.A. Bartz, 'Cooling Towers and Ponds'. In: Handbook of Heat Transfer Applications, Rosenow, W.M., J.P. Hartnett and E.N. Ganic, eds. Chapter 10. McGraw-Hill, 1985.

McCutcheon, S.C., Z. Dongwei and S. Bird, 1990. Model calibration, validation, and use. Chapter 5 in: Technical Guidance Manual for Performing Waste Load Allocations, Book III: Estuaries. Part 2: Application of Estuarine Waste Load Allocation Models. Edited by J.L. Martin, R.B. Ambrose and S.C. McCutcheon. United States Environmental Protection Agency, Office of Water. March 1990.

Mendelsohn, D., 1998. Development of an Estuarine Thermal Environmental Model in a Boundary Fitted, Curvilinear Coordinate System. Applied Science Associates, Inc., 1998.

Mendelsohn, D., et al, 1995. WQMAP in a Windows environment, published in proceedings of: 4th International Conference on Estuarine and Coastal Modeling, ASCE, San Diego, October 26-28, 1995.

Muin, Muslim, 1993. Development and Application of a Three-Dimensional Boundary-fitted Model in Providence River, presented at: Estuarine and Coastal Modeling III, proceedings of the 3rd International Conference, Oak Brook, Illinois, September 8-10, 1993.

Muin, Muslim, and Malcolm Spaulding, 1998. Three-Dimensional Boundary-Fitted Circulation Model, published in: Journal of Hydraulic Engineering, January 1997.

Normandeau Associates Incorporated, 'A Probabilistic Thermal Model of the Merrimack River Downstream Of Merrimack Station'. 2007.

Porter, R.W. et.al., 'Thermal Performance of Spray-Cooling Systems', Proc. Am. Power Conf., Vol 38, pp 1458-1472, 1976.

Ralston,K.D., Geyer,W.R.,and Lerczak,J.A.,2007, Subtidal Salinity and Velocity in the Hudson River Estuary: Observations and Modeling. , Journal of Physical Oceonography, v. 38 no.4, p. 753-770.

Warner, J.,Geyer, and W.R, Lerczack,J. 2005.Numerical modeling of an estuary: A comprehensive skill assessment. Journal of Geophysical Research, v. 110, C05001, doi:10.1029/2004JC0026

Swanson, J.C., 1986. A three-dimensional numerical model system of coastal circulation and water quality, Ph.D. Dissertation, Univ. of Rhode Island, Kingston, R.I.

Swanson, C. and T. Isaji, 2001. Preliminary modeling of the RESCO facility thermal plume in the Saugus River. Report prepared for Environmental Strategic Systems, Inc., May 2001, 15 p.

Swanson, J. C., H.-S. Kim, S. Subbayya, P. Hall, and J. Patel. 2004 (Revised). Hydrothermal Modeling of the Cooling Water Discharge from the Vermont Yankee Power Plant to the Connecticut River, Prepared for Normandeau Associates, Inc., Bedford, NH, ASA Project 02-088, 84 p. plus appendices, Applied Science Associates, Narragansett, RI.

Swanson, C., Y. Kim, D. Mendelsohn, and D. Crowley, 2010Y. Preliminary Analysis of Hudson River Thermal Data. ASA Project 09-167. Prepared for Elise Zoli, Goodwin Procter, Boston, MA, 10 February 2010.

APPENDIX A: HYDRODYNAMIC MODEL DESCRIPTION (MUIN AND SPAULDING, 1997)

THREE-DIMENSIONAL BOUNDARY-FITTED CIRCULATION MODEL

By Muslim Muin[1] and Malcolm Spaulding[2]

ABSTRACT: A spherical coordinate, three-dimensional, nonorthogonal, boundary-fitted circulation model (contravariant formulation) for application to estuarine, coastal sea, and continental shelf waters is presented. The model employs a split mode technique where the equations are decomposed into exterior and interior modes. The exterior mode (vertically averaged) described in an earlier paper (Muin and Spaulding 1996) is solved using a semiimplicit solution technique. The interior mode (vertical structure) is solved explicitly, except for the vertical diffusion terms that are solved implicitly. The temporally and spatially varying eddy viscosity and diffusivity are determined from a turbulent kinetic energy equation and an empirically specified length scale. A series of tests are presented to evaluate model performance where analytical solutions or other numerical solutions are available for comparison. The model's ability to predict the point vertical structure of tidal flow is tested against analytic solutions employing (1) constant viscosity; and (2) an eddy viscosity varying linearly with depth with a no-slip bottom boundary condition. The ability of the model to simulate three-dimensional tidal flow was tested against an exact solution for an annular section channel with quadratically varying bathymetry. The model was also tested against analytic solutions for steady residual flow generated by density gradient, wind, and river flow in a channel. The model predicted turbulent energy distributions generated from a bottom boundary were compared to those from a previous numerical study by Davies and Jones (1990). No-slip and bottom stress formulations at the sea bed, and their effect on the vertical structure of the flow are analyzed. The model was used to predict the salinity distribution in a simple rectangular channel identical to the Rotterdam Waterway. The computational method is very economical, stable, and accurate with the CFL stability condition up to 100.

INTRODUCTION

Numerical modeling techniques are routinely used to study circulation and pollutant transport in estuarine and coastal waters. The majority of models employ finite-difference techniques on square grid systems. While this has proven useful in various applications, it becomes expensive when the study region is geometrically and bathymetrically complex. Such difficulties motivate the use of alternative solution approaches that allow flexibility in the grid specification, for example finite elements (Lynch and Werner 1987) and boundary-fitted coordinates (Johnson 1980; Spaulding 1984; Sheng 1986; Swanson 1986; Muin and Spaulding 1996).

This paper presents the extension of a two-dimensional (2D) vertically averaged, boundary fitted, spherical coordinate circulation model developed by Muin and Spaulding (1996) to three dimensions. The paper first presents the governing equations in spherical coordinates with appropriate assumptions and boundary conditions. The equations are further transformed to a σ-coordinate. This is followed by presentations of the governing equations in a generalized curvilinear coordinate system, turbulence parameterization, the solution methodology, and model testing for which analytic (linear problems) solutions or other numerical solutions are readily available. Testing emphasizes calculations of the vertical structure of the flow. Testing of the 2D vertically averaged version of the model for a series of horizontal flow problems (see Lynch and Gray 1978) was presented in Muin and Spaulding (1996).

GOVERNING EQUATIONS

Using a spherical coordinate system, where ϕ = longitude positive east; θ = latitude positive north; and r = positive up, the equations of continuity, momentum, and conservation of substance can be written as

Continuity

$$\frac{1}{r\cos\theta}\frac{\partial u}{\partial \phi}+\frac{1}{r}\frac{\partial v}{\partial \theta}-\frac{v}{r}\tan\theta+\frac{1}{r^2}\frac{\partial r^2 w}{\partial r}=0 \tag{1}$$

Momentum

ϕ-direction

$$\frac{\partial u}{\partial t}+\frac{u}{r\cos\theta}\frac{\partial u}{\partial \phi}+\frac{v}{r}\frac{\partial u}{\partial \theta}-\frac{uv}{r}\tan\theta+w\frac{\partial u}{\partial r}+\frac{uw}{r}-fv = -\frac{1}{\rho_o r\cos\theta}\frac{\partial p}{\partial \phi}+\frac{\partial}{\partial r}\left(A_v\frac{\partial u}{\partial r}\right) \tag{2}$$

θ-direction

$$\frac{\partial v}{\partial t}+\frac{u}{r\cos\theta}\frac{\partial v}{\partial \phi}+\frac{v}{r}\frac{\partial v}{\partial \theta}+\frac{uu}{r}\tan\theta+w\frac{\partial v}{\partial r}+\frac{vw}{r}+fu = -\frac{1}{\rho_o r\cos\theta}\frac{\partial p}{\partial \theta}+\frac{\partial}{\partial r}\left(A_v\frac{\partial v}{\partial r}\right) \tag{3}$$

r-direction

$$\frac{\partial p}{\partial r}=-\rho g \tag{4}$$

Conservation of Substance

$$\frac{\partial q}{\partial t}+\frac{u}{r\cos\theta}\frac{\partial q}{\partial \phi}+\frac{v}{r}\frac{\partial q}{\partial \theta}+w\frac{\partial q}{\partial r}=\frac{\partial}{\partial r}\left[D_v\left(\frac{\partial q}{\partial r}\right)\right]+\frac{D_h}{r^2}\left[\frac{\partial^2 q}{\cos^2\theta\,\partial\phi^2}+\frac{\partial^2 q}{\partial\theta^2}\right] \tag{5}$$

Equation of State of Sea Water

$$\rho=f(S,\Theta) \tag{6}$$

where t = time; u, v and w = velocity components in ϕ, θ, and r directions, respectively; f = Coriolis parameter; p = pressure; g = gravity; ρ = water density; ρ_o = basin-averaged water density; A_v = vertical eddy viscosity; D_v = vertical eddy diffusiv-

[1]Jurusan Teknik Sipil, Institut Teknologi Bandung, Bandung, Indonesia.

[2]Prof. and Chair., Dept. of Oc. Engrg., Univ. of Rhode Island, Narragansett Bay Campus, Narragansett, RI 02882.

Note. Discussion open until June 1, 1997. Separate discussions should be submitted for the individual papers in this symposium. To extend the closing date one month, a written request must be filed with the ASCE Manager of Journals. The manuscript for this paper was submitted for review and possible publication on January 10, 1994. This paper is part of the *Journal of Hydraulic Engineering*, Vol. 123, No. 1, January, 1997. ISSN 0733-9429/97/0001-0002–0012/$4.00 + $.50 per page. Paper No. 7655.

ity; D_h = horizontal eddy diffusivity; Θ = temperature °C; S = salinity (ppt); and q = concentration of a conservative substance such as Θ or S.

The equations described previously assume the following: the flow is incompressible, density differences are neglected unless multiplied by gravity (Boussinesq approximation), the vertical acceleration is very small compared to gravity (hydrostatic assumption), and the horizontal stresses are neglected.

Boundary Conditions

The land boundaries are assumed impermeable where the normal component of velocity is set to zero

$$\vec{V}\cdot\vec{n} = 0 \tag{7}$$

On river boundaries, the velocities are specified and the pressure gradient is set to zero. At open boundaries the water elevation or vertically varying velocity as a function of time is known from field observations or otherwise specified.

At closed boundaries the transport of substance is zero. At an open boundary the concentration must be specified during inflow. On outflow the substance is advected out of the model domain according to

$$\frac{\partial q}{\partial t} + \frac{u}{r\cos\theta}\frac{\partial q}{\partial \phi} = 0 \tag{8a}$$

$$\frac{\partial q}{\partial t} + \frac{v}{r}\frac{\partial q}{\partial \theta} = 0 \tag{8b}$$

At the surface, the wind stress is specified as

$$\tau_{s\phi} = \rho_a C_a W_\phi \sqrt{W_\phi^2 + W_\theta^2}, \quad \tau_{s\theta} = \rho_a C_a W_\theta \sqrt{W_\phi^2 + W_\theta^2} \tag{9}$$

where W_ϕ and W_θ = wind speeds in the ϕ and θ directions, respectively; ρ_a = density of air; and C_a = drag coefficient at the surface.

The kinematic free surface boundary condition is given as

$$w = \frac{\partial \zeta}{\partial t} + \frac{u}{r\cos\theta}\frac{\partial \zeta}{\partial \phi} + \frac{v}{r}\frac{\partial \zeta}{\partial \theta} \tag{10}$$

Two options are available to specify the bottom boundary condition

1. Bottom stress condition

$$\tau_{b\phi} = \rho_o C_b u_b \sqrt{u_b^2 + v_b^2}, \quad \tau_{b\theta} = \rho_o C_b v_b \sqrt{u_b^2 + v_b^2} \tag{11}$$

   where C_b = bottom drag coefficient; and u_b and v_b = velocity components at the bottom in the ϕ and θ directions, respectively.
2. No-slip condition

$$u_b = 0 \quad \text{and} \quad v_b = 0 \tag{12}$$

At the bottom boundary, no momentum flux is allowed and the kinematic condition is specified

$$w = -u_b\frac{1}{r\cos\theta}\frac{\partial h}{\partial \phi} - v_b\frac{1}{r}\frac{\partial h}{\partial \theta} \tag{13}$$

The governing equations are transformed to a σ-coordinate system to resolve bathymetric variations with a constant number of grids. The transformation is defined as

$$\phi = \phi', \quad \theta = \theta', \quad r = R + \zeta + (\sigma - 1)(\zeta + h)/2, \quad t = t' \tag{14}$$

The governing equations now become (dropping the primes for convenience)

Continuity

$$\frac{\partial \zeta}{\partial t} + \frac{1}{r\cos\theta}\frac{\partial uD}{\partial \phi} + \frac{1}{r}\frac{\partial vD}{\partial \theta} - \frac{vD}{r}\tan\theta + \frac{\partial \omega D}{\partial \sigma} = 0 \tag{15}$$

Momentum

ϕ-direction

$$\frac{\partial uD}{\partial t} + \frac{1}{r\cos\theta}\frac{\partial uuD}{\partial \phi} + \frac{1}{r}\frac{\partial uvD}{\partial \theta} - \frac{2uvD}{r}\tan\theta + \frac{\partial u\omega D}{\partial \sigma} - fvD$$
$$= -\frac{gD}{2\rho_o r\cos\theta}\left\{[\lambda + (\rho_s - 2\rho)(1-\sigma)]\frac{\partial D}{\partial \phi} + (4\rho - 2\rho_s)\frac{\partial \zeta}{\partial \phi} + D\frac{\partial \lambda}{\partial \phi}\right\} + \frac{4}{D}\frac{\partial}{\partial \sigma}\left(A_v\frac{\partial u}{\partial \sigma}\right) \tag{16}$$

θ-direction

$$\frac{\partial vD}{\partial t} + \frac{1}{r\cos\theta}\frac{\partial uvD}{\partial \phi} + \frac{1}{r}\frac{\partial vvD}{\partial \theta} - \frac{uu - vv}{r}D\tan\theta + \frac{\partial v\omega D}{\partial \sigma} + fuD$$
$$= -\frac{gD}{2\rho_o r}\left\{[\lambda + (\rho_s - 2\rho)(1-\sigma)]\frac{\partial D}{\partial \theta} + (4\rho - 2\rho_s)\frac{\partial \zeta}{\partial \theta} + D\frac{\partial \lambda}{\partial \theta}\right\} + \frac{4}{D}\frac{\partial}{\partial \sigma}\left(A_v\frac{\partial v}{\partial \sigma}\right) \tag{17}$$

σ-direction

$$\frac{2}{D}\frac{\partial p}{\partial \sigma} = -\rho g \tag{18}$$

Conservation of Substance

$$\frac{\partial q}{\partial t} + \frac{u}{r\cos\theta}\frac{\partial q}{\partial \phi} + \frac{v}{r}\frac{\partial q}{\partial \theta} + \omega\frac{\partial q}{\partial \sigma} = \frac{4}{D^2}\frac{\partial}{\partial \sigma}\left[D_v\left(\frac{\partial q}{\partial \sigma}\right)\right] + \frac{D_h}{r^2}\left(\frac{\partial^2 q}{\cos^2\theta\,\partial\phi^2} + \frac{\partial^2 q}{\partial \theta^2}\right) \tag{19}$$

where

$$\lambda = \int_\sigma^1 \rho\, d\sigma \tag{20a}$$

$$\omega = -\frac{1}{D}(1+\sigma)\frac{\partial \zeta}{\partial t} + \gamma_\phi u + \gamma_\theta v + \frac{2}{D}w \tag{20b}$$

$$\gamma_\phi = \frac{1}{D}\left[\frac{1-\sigma}{r\cos\theta}\frac{\partial h}{\partial \phi} - \frac{1+\sigma}{r\cos\theta}\frac{\partial \zeta}{\partial \phi}\right] \tag{20c}$$

$$\gamma_\theta = \frac{1}{D}\left[\frac{1-\sigma}{r\cos\theta}\frac{\partial h}{\partial \theta} - \frac{1+\sigma}{r\cos\theta}\frac{\partial \zeta}{\partial \theta}\right] \tag{20d}$$

where $D = h + \zeta$ = total water depth.

The horizontal velocities and independent variables are next transformed to a curvilinear coordinate system. The equations of motion and continuity equation in a curvilinear coordinate system (ξ, η), in terms of the contravariant velocity components, are as follows:

Continuity

$$Jr\cos\theta\frac{\partial \zeta}{\partial t} + \frac{\partial}{\partial \xi}(\cos\theta Ju^c D) + \frac{\partial}{\partial \eta}(\cos\theta Jv^c D) + Jr\cos\theta\frac{\partial(\omega D)}{\partial \sigma} = 0 \tag{21}$$

Momentum Equation

ξ-direction

$$\frac{\partial u^c D}{\partial t} = -\frac{\theta_\eta\theta_\eta + \cos^2\theta\phi_\eta\phi_\eta}{J^2\rho_o r\cos^2\theta}\frac{Dg}{2}\left\{[\lambda + (\rho_s - 2\rho)(1-\sigma)]\frac{\partial D}{\partial \xi} + (4\rho - 2\rho_s)\frac{\partial \zeta}{\partial \xi} + D\frac{\partial \lambda}{\partial \xi}\right\} + \frac{\theta_\xi\theta_\eta + \cos^2\theta\phi_\xi\phi_\eta}{J^2\rho_o r\cos^2\theta}\frac{Dg}{2} \cdot\left\{[\lambda + (\rho_s - 2\rho)(1-\sigma)]\frac{\partial D}{\partial \eta} + (4\rho - 2\rho_s)\frac{\partial \zeta}{\partial \eta} + D\frac{\partial \lambda}{\partial \eta}\right\} - \frac{\theta_\eta}{J^2 r\cos^2\theta}\left[\frac{\partial}{\partial \xi}(\phi_\xi\cos^2\theta J u^c u^c D + \phi_\eta\cos^2\theta J u^c v^c D) + \frac{\partial}{\partial \eta}(\phi_\xi\cos^2\theta J u^c v^c D + \phi_\eta\cos^2\theta J v^c v^c D)\right] + \frac{\phi_\eta}{J^2 r\cos^2\theta}\left[\frac{\partial}{\partial \xi}(\theta_\xi\cos^2\theta J u^c u^c D + \theta_\eta\cos^2\theta J u^c v^c D) + \frac{\partial}{\partial \eta}(\theta_\xi\cos^2\theta J u^c v^c D + \theta_\eta\cos^2\theta J v^c v^c D)\right] - \frac{\partial}{\partial \sigma}(\omega u^c D) + \frac{fD}{J\cos\theta}[(\theta_\xi\theta_\eta + \cos^2\theta\phi_\xi\phi_\eta)u^c + (\theta_\eta\theta_\eta + \cos^2\theta\phi_\eta\phi_\eta)v^c] + \frac{4}{D}\frac{\partial}{\partial \sigma}\left(A_v\frac{\partial u^c}{\partial \sigma}\right) \tag{22}$$

η-direction

$$\frac{\partial v^c D}{\partial t} = \frac{\theta_\eta\theta_\xi + \cos^2\theta\phi_\eta\phi_\xi}{J^2\rho_o r\cos^2\theta}\frac{Dg}{2}\left\{[\lambda + (\rho_s - 2\rho)(1-\sigma)]\frac{\partial D}{\partial \xi} + (4\rho - 2\rho_s)\frac{\partial \zeta}{\partial \xi} + D\frac{\partial \lambda}{\partial \xi}\right\} - \frac{\theta_\xi\theta_\xi + \cos^2\theta\phi_\xi\phi_\xi}{J^2\rho_o r\cos^2\theta}\frac{Dg}{2} \cdot\left\{[\lambda + (\rho_s - 2\rho)(1-\sigma)]\frac{\partial D}{\partial \eta} + (4\rho - 2\rho_s)\frac{\partial \zeta}{\partial \eta} + D\frac{\partial \lambda}{\partial \eta}\right\} + \frac{\theta_\xi}{J^2 r\cos^2\theta}\left[\frac{\partial}{\partial \xi}(\phi_\xi\cos^2\theta J u^c u^c D + \phi_\eta\cos^2\theta J u^c v^c D) + \frac{\partial}{\partial \eta}(\phi_\xi\cos^2\theta J u^c v^c D + \phi_\eta\cos^2\theta J v^c v^c D)\right] - \frac{\phi_\xi}{J^2 r\cos^2\theta}\left[\frac{\partial}{\partial \xi}(\theta_\xi\cos^2\theta J u^c u^c D + \theta_\eta\cos^2\theta J u^c v^c D) + \frac{\partial}{\partial \eta}(\theta_\xi\cos^2\theta J u^c v^c D + \theta_\eta\cos^2\theta J v^c v^c D)\right] - \frac{\partial}{\partial \sigma}(\omega v^c D) - \frac{fD}{J\cos\theta}[(\theta_\xi\theta_\xi + \cos^2\theta\phi_\xi\phi_\xi)u^c + (\theta_\xi\theta_\eta + \cos^2\theta\phi_\xi\phi_\eta)v^c] + \frac{4}{D}\frac{\partial}{\partial \sigma}\left(A_v\frac{\partial v^c}{\partial \sigma}\right) \tag{23}$$

Conservation of Substance

$$\frac{\partial q}{\partial t} + \frac{u^c}{r}\frac{\partial q}{\partial \xi} + \frac{v^c}{r}\frac{\partial q}{\partial \eta} + \omega\frac{\partial q}{\partial \sigma} = \frac{4}{D^2}\frac{\partial}{\partial \sigma}\left(D_v\frac{\partial q}{\partial \sigma}\right) + \frac{D_h}{r^2 J^2} \cdot\left[\left(\frac{\theta_\eta\theta_\eta}{\cos^2\theta} + \phi_\eta\phi_\eta\right)\frac{\partial^2 q}{\partial \xi^2} - 2\left(\frac{\theta_\xi\theta_\eta}{\cos^2\theta} + \phi_\xi\phi_\eta\right)\frac{\partial^2 q}{\partial \xi\partial \eta} + \left(\frac{\theta_\xi\theta_\xi}{\cos^2\theta} + \phi_\xi\phi_\xi\right)\frac{\partial^2 q}{\partial \eta^2}\right] \tag{24}$$

where u^c and v^c = contravariant velocities in the (ξ, η) directions, respectively; ζ = water elevation; $D = \zeta$ + depth; and the Jacobian, $J = \phi_\xi\theta_\eta - \phi_\eta\theta_\xi$. The relationship between the contravariant velocities (u^c, v^c) and velocities in spherical coordinates (u, v) is given by

$$u = \cos\theta\phi_\xi u^c + \cos\theta\phi_\eta v^c \tag{25a}$$

$$v = \theta_\xi u^c + \theta_\eta v^c \tag{25b}$$

TURBULENCE PARAMETERIZATION

The turbulence parameterization is a key model component for predicting flow and mixing processes in stratified fluids. There is, however, no universally accepted procedure to represent turbulence (ASCE 1988; Cheng and Smith 1990). In this study, we employ a one equation turbulent kinetic energy model to calculate the vertical eddy viscosity and diffusivity. The length scale is specified using the approach suggested by Blackadar (1962) that has been successfully used in modeling turbulence for tidal problems (Davies and Jones 1990). The effect of stratification is accounted for by using an empirical relationship similar to the ones employed for the mixing length approach. This model accounts for the convection, diffusion, and time history of turbulent kinetic energy in unsteady flows.

Turbulent Energy

The turbulence kinetic energy equation in spherical and σ-coordinates is given as follows:

$$\frac{\partial b}{\partial t} + \frac{u}{r\cos\theta}\frac{\partial b}{\partial \phi} + \frac{v}{r}\frac{\partial b}{\partial \theta} + \omega\frac{\partial b}{\partial \sigma} = \frac{4}{D^2}\frac{\partial}{\partial \sigma}\left(\frac{A_v}{\sigma_b}\frac{\partial b}{\partial \sigma}\right) + A_v\left[\left(\frac{2}{D}\frac{\partial u}{\partial \sigma}\right)^2 + \left(\frac{2}{D}\frac{\partial v}{\partial \sigma}\right)^2\right] + \beta g\frac{2A_v}{D\sigma_t}\frac{\partial \Phi}{\partial \sigma} - \varepsilon \tag{26}$$

where b = kinetic energy.

After transformation to curvilinear coordinates (ξ, η), the preceding equation can be written as

$$\frac{\partial b}{\partial t} + \frac{u^c}{r}\frac{\partial b}{\partial \xi} + \frac{v^c}{r}\frac{\partial b}{\partial \eta} + \omega\frac{\partial b}{\partial \sigma} = \frac{4}{D^2}\frac{\partial}{\partial \sigma}\left(\frac{A_v}{\sigma_b}\frac{\partial b}{\partial \sigma}\right) + A_v\left[\left(\frac{2}{D}\frac{\partial u}{\partial \sigma}\right)^2 + \left(\frac{2}{D}\frac{\partial v}{\partial \sigma}\right)^2\right] + \beta g\frac{2A_v}{D\sigma_t}\frac{\partial \Phi}{\partial \sigma} - \varepsilon \tag{27}$$

where β = volumetric expansion coefficient; σ_b = empirical diffusion constant; σ_t = Schmidt number; Φ = mean scalar quantity; and ε = dissipation. In this study the interchange between turbulent kinetic energy and potential energy or production/dissipation by buoyant forces is neglected. It is assumed that the turbulent kinetic energy is advected and diffused in a homogeneous fluid while the effect of stratification is accounted for by an empirical formula using a Richardson number (damping function). As argued by Abraham (1988), the reproduction of internal mixing at tidal slack is beyond the capability of present turbulence models and, hence, they should not be used where this aspect is important.

Eddy Viscosity and Diffusivity Relationships

Based on dimensional reasoning the eddy viscosity is related to the kinetic energy b and mixing length L_m by

$$A_v = C_\mu L_m\sqrt{b} \tag{28}$$

where C_μ = empirical constant.

In homogeneous water, the vertical eddy viscosity and diffusivity are considered to be equal, $A_v = D_v$. In the presence of a stable vertical density gradient, both A_v and D_v are lower than their homogeneous values. The magnitude of A_v is always greater than the corresponding value of D_v.

The general form for the eddy viscosity and diffusivity are given as

$$A_v = f(R_i) C_\mu L_m \sqrt{b} \tag{29a}$$

$$D_v = g(R_i) C_\mu L_m \sqrt{b} \tag{29b}$$

Several semiempirical relations for $f(R_i)$ and $g(R_i)$ have been proposed by Munk and Anderson (1948) and Officer (1976).

Munk and Anderson (1948)

$$f(R_i) = (1 + 10.0R_i)^{-1/2} \tag{30a}$$

$$g(R_i) = (1 + 3.33R_i)^{-3/2} \tag{30b}$$

Officer (1976)

$$f(R_i) = (1 + R_i)^{-1} \tag{31a}$$

$$g(R_i) = (1 + R_i)^{-2} \tag{31b}$$

where the Richardson number, R_i, is defined by

$$R_i = -\frac{2g}{\rho D} \frac{\dfrac{\partial \rho}{\partial \sigma}}{\left[\dfrac{\partial (u)}{\partial \sigma}\right]^2 + \left[\dfrac{\partial (v)}{\partial \sigma}\right]^2} \tag{32}$$

Dissipation

From dimensional analysis the expression for dissipation, in terms of the turbulent kinetic energy and mixing length, is given by

$$\varepsilon = C_d (b^{3/2}/L_m) \tag{33}$$

where C_d = empirical constant.

Mixing Length

The mixing length formulation proposed by Blackadar (1962) is

$$L_m = \frac{KD[1 + (\sigma - 1)/2]}{1 + \dfrac{KD[1 + (\sigma - 1)/2]}{L_v}} \tag{34}$$

where K = Von Karman's constant; D = total water depth and in which the mixing length, L_m, increases from the sea bottom to the surface and the value of L_v is determined by the vertical distribution of the turbulent energy as follows:

$$L_v = \gamma D \frac{\displaystyle\int_{-1}^{1} b^{1/2}[1 + (\sigma - 1)/2]\, d\sigma}{\displaystyle\int_{-1}^{1} b^{1/2}\, d\sigma} \tag{35}$$

The constant γ determines the vertical extent of the boundary layer and vertical eddy viscosity, and is adjusted to match field observations. The viscosity increases rapidly with increasing γ in both amplitude and vertical extent (Mofjeld and Lavelle 1983). The constant γ typically ranges from 0.05 to 0.3. The coefficients in (28), (34), and (35) have values C_μ = 0.463; C_d = 0.1; σ_b = 1.37; and K = 0.4 (Davies and Jones 1990).

Boundary Conditions

The boundary condition at the surface is specified as

$$\frac{2\alpha_b A_v}{D} \frac{\partial b}{\partial \sigma} = \alpha_w U_{*_s}^2 \tag{36}$$

where U_{*_s} = friction velocity due to the wind stress and α_b, α_w are coefficients. A similar boundary condition is used by Davies and Jones (1988) in which α_b = 0.73, and α_w = 2.6. In the absence of wind forcing the flux of turbulence at the surface disappears.

For a no-slip bottom boundary condition, the turbulent kinetic energy flux into the sea bed is zero (Davies and Jones 1988) and, therefore

$$\frac{\partial b}{\partial \sigma} = 0 \tag{37}$$

For the bottom stress boundary condition, the bottom boundary layer is not resolved in detail. The turbulent kinetic energy, b, at the first grid point near the wall (where the turbulence is assumed in equilibrium and the velocity follows the log-law) is given as follows:

$$b = U_{*_b}^2 / \sqrt{C_\mu C_d} \tag{38}$$

where U_{*_b} = friction velocity associated with the bottom stress. While this boundary condition is not always rigorously satisfied under unsteady conditions (Celik and Rodi 1985), it is used as a first-order approximation.

SOLUTION TECHNIQUE

The basic approach is to transform the dependent, as well as independent, variables in spherical coordinates to a curvilinear coordinate system. The equation of motion is split into exterior and interior modes to increase the allowable time step and, hence, reduce the computational time.

The velocity is decomposed into

$$u^c = U^c + u^{c\prime} \tag{39a}$$

$$v^c = V^c + v^{c\prime} \tag{39b}$$

where (U^c, V^c) and $(u^{c\prime}, v^{c\prime})$ = vertically averaged velocities and deviation velocity (from the vertically averaged velocity) in (ξ, η) directions, respectively. Solution of the exterior mode using a semiimplicit (space staggered grid) solution, methodology, and presentations of the approach used to generate the boundary conforming grid are presented by Muin and Spaulding (1996). The focus here is on three-dimensional (3D) aspects, including the deviation velocity and the turbulence equation.

Subtracting the vertically averaged momentum equations from the 3D momentum equations gives the vertical deviation velocity equations of motion

$$\frac{\partial u^{c\prime} D}{\partial t} = \frac{4}{D} \frac{\partial}{\partial \sigma} \left(A_v \frac{\partial u^{c\prime}}{\partial \sigma} \right) + A \tag{40a}$$

$$\frac{\partial v^{c\prime} D}{\partial t} = \frac{4}{D} \frac{\partial}{\partial \sigma} \left(A_v \frac{\partial v^{c\prime}}{\partial \sigma} \right) + B \tag{40b}$$

where A and B = nonbarotropic terms in the equations of motion. These terms are solved explicitly. The diffusion term in (40) is solved implicitly using a three-level scheme to damp out spurious oscillations (Fletcher 1988). The algorithm is second-order accurate both in time and spece. A tridiagonal set of equations in the unknown velocity deviation is solved using a Thomas algorithm. Both the exterior and interior modes are solved at the same time step.

The finite difference procedure used to solve the turbulent kinetic energy equations has been described by Davies and Jones (1990). In the present study, a three-level time discretization (Fletcher 1988) is used instead of the Crank-Nicholson method of Davies and Jones (1990). A nonstaggered grid is used in the vertical. The C form of Davies and Jones' (1990) numerical scheme is employed to calculate the dissipation term

in the energy equation to ease the time step restriction. No iteration or filtering is employed. The time step is restricted by the horizontal advection term. As will be shown in model testing, a CFL equal to 100 can be used to predict the vertical structure of tidally induced flows.

The transport model (24) is solved by a simple explicit technique, except for the vertical diffusion that is solved by an implicit scheme to ease the time step restriction due to the small vertical length scale. In the present model, two options are available to solve the advection term. The first option is a Lax-Wendroff scheme, which is consistent with a second-order truncation error (Fletcher 1988). The second option is an upwind-differencing scheme (first-order accurate) that introduces artificial diffusivity. The horizontal diffusion term is solved by a centered-in-space, explicit technique. The diffusive and advective stability criteria in these numerical techniques are $\Delta t < \Delta s^2/(2D_h)$, and $\Delta t < \Delta s/U_s$, where Δs and U_s = horizontal grid size and velocity, respectively. To avoid spatial oscillations, the Lax-Wendroff scheme requires $D_h > U_s\Delta s/2$. This gives approximately the same amount of artificial viscosity as inherent in the upwind scheme.

MODEL TESTING

Model formulation and implementation, in computer code, were compared to analytical solutions in which the nonlinear convective acceleration and Coriolis terms were removed and the governing equations solved on a spherical coordinate system, which because of the limited domain approximated a Cartesian grid. Additional test simulations were performed to confirm the operation of the turbulent closure equations to predict the vertical structure of tidal flow and compared to a previous numerical study by Davies and Jones (1990). The model was tested in an application to salinity intrusion in a simple rectangular channel representative of the Rotterdam Waterway.

Residual Flow

The ability of the model to predict residual flow was tested for a basin with vertically constant density and viscosity. The surface boundary was forced by a constant wind stress if wind forcing was used. The test was performed in a simple, rectangular, and constant depth channel open at one end (west). The model was run for two bottom boundary conditions: (1) no-slip condition; and (2) bottom stress condition.

Following Officer's (1976) approach and neglecting advection, the horizontal diffusion of momentum, and the cross channel terms (equations laterally averaged), the steady-state expression for the vertical velocity profiles with linearized bottom friction can be given as follows

$$u = -g\Lambda\left(\frac{z^3}{6\rho A_v} + \frac{h^2}{2\rho k} + \frac{h^3}{6\rho A_v}\right) - g\iota\left(\frac{h}{k} + \frac{h^2}{2A_v} - \frac{z^2}{2A_v}\right) + \frac{\tau_s}{\rho}\left(\frac{1}{k} + \frac{h}{A_v} + \frac{z}{A_v}\right) \quad (41)$$

where

$$g\iota = \frac{\left[-g\Lambda\left(\frac{h^3}{2\rho k} + \frac{h^4}{8\rho A_v}\right) + \frac{\tau_s}{\rho}\left(\frac{h}{k} + \frac{h^2}{2A_v}\right) - hu_o\right]}{\left(\frac{h^2}{k} + \frac{h^3}{3A_v}\right)} \quad (42)$$

where Λ = horizontal density gradient; g = gravity; ι = water elevation slope; τ_s = wind stress; u_o = river flow per width; and k = linearized bottom friction. A similar equation for a no-slip condition at the bottom is given on page 120 of Officer (1976).

Three separate simulations with different forcings were studied: (1) density gradient flow; (2) wind driven flow; and (3) density gradient, wind, and river-induced flow. In these simulations, the following conditions were assumed: the density increases linearly from the head (closed end) to the mouth (open end) $\Lambda = -0.00036$ kg/m^4; wind stress $\tau_s = 0.01$ N/m^2 (1 dyne/cm^2); river flow $u_o = -0.1$ m/s; depth $h = 10$ m; vertical viscosity $A_v = 10$ cm^2/s; and linearized bottom friction $k = 0.05$ cm/s. Depending on the case the appropriate forcing parameters were used. Testing was performed using five, 10, and 20 vertical levels. The model was started with zero velocities and elevation. The density gradient was applied gradually until a steady state was achieved.

Density Gradient Forcing

Fig. 1(a) shows a comparison of the model prediction to analytic solution for the bottom stress formulation under density gradient forcing. Model predictions approach the analytic solution as the grid resolution is increased. The model overpredicts the currents near the bottom and surface at low grid resolution. The maximum errors are about 7% for five levels, 2% for 10 levels, and less than 1% for 20 levels. The model was also run with a no-slip bottom boundary condition, as shown in Fig. 1(b). When the surface boundary condition was specified using a second-order accurate representation, the model never reached steady state even with 80 levels. This problem may be caused by an underestimate of the bottom friction, which is only first-order accurate. The model, however, reached steady state when the surface boundary was reduced to first order. For this approximation the model overpredicted the velocity near the surface by 20% [Fig. 1(b)] independent of the number of the vertical levels.

Wind Forcing

Comparison of model predictions with the analytic solution under constant wind forcing with a bottom stress condition is

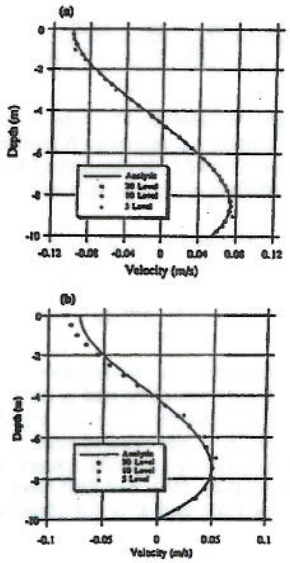

FIG. 1. Comparison of Model Predicted Vertical Structure of Velocity with Analytic Solution for Density-Induced Forcing (A_v = 10 cm^2/s, $\Lambda = -0.00036$ kg/m^4, $k = 0.05$ cm/s) for: (a) Bottom Stress; and (b) No-Slip Bottom Boundary Condition (Model Results Are Presented for 5, 10, and 20 Vertical Levels)

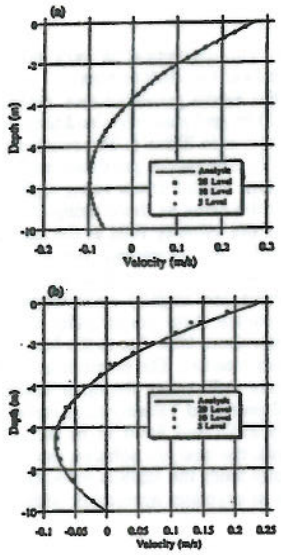

FIG. 2. Comparison of Model Predicted Vertical Structure of Velocity with Analytic Solution for Wind Driven Flow (A_v = 10 cm²/s, τ_s = 0.1 N/m² (1 dyne/cm²), k = 0.05 cm/s) for: (a) Bottom Stress; and (b) No-Slip Bottom Boundary Condition (Model Results Are Presented for 5, 10, and 20 Vertical Levels)

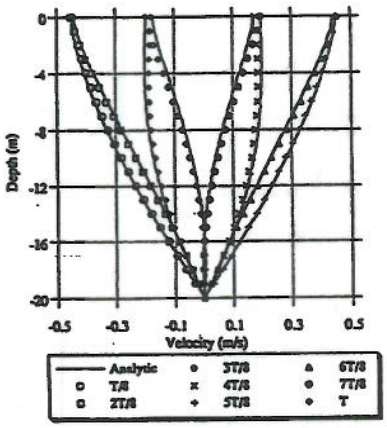

FIG. 3. Comparison of Model Predicted Velocity Structure with Analytic Solution for Tidally Driven Flow (Imposed Pressure Gradient of 0.058 N/m³) with Constant Vertical Viscosity, A_v = 0.011 m²/s at 1/8 Time Intervals Through One Tidal Cycle (Time Step, Δt = 279.45 s)

shown in Fig. 2(a). It can be seen that as the resolution increases the model predictions approach the analytic solution, especially near the bottom. The model represents the vertical velocity structure more accurately than for the density induced flow problem. The maximum errors are about 2% for five levels, 0.6% for 10 levels, and 0.2% for 20 levels. A similar problem, as in the density-induced flow, was found for the no-slip condition at the bottom and the boundary condition at the surface was modified to first order. The results are shown in Fig. 2(b). Again model prediction for this case is more accurate than in the baroclinic forcing problem.

Density Gradient Wind and River Forcing

The last test case considered flow driven by a combination of density gradient, wind, and river flow. The model was run using 20 levels. The results, not shown here, were simulated for bottom stress and no-slip bottom specifications, respectively. The agreement is excellent (<0.5%) for the bottom stress bottom boundary condition. The model underpredicts the velocity by about 5% in the mid-depth region for the no-slip bottom boundary condition.

Tidal Driven Flow

Two tests were employed to check the model's ability to simulate the vertical structure of tidal flow. The first test case is a point model in which the bottom boundary is specified using a no-slip condition, and the water slope is assumed known. The model was tested against constant and linearly varying vertical eddy viscosities. In the second test a bottom stress condition was employed at the sea bed. The bottom friction was linearized and related to the vertically averaged velocity.

Point Model Test

Constant Viscosity

The analytic solution for this problem was given in article 347 in Lamb (1945). The following data are used in model testing. The imposed pressure gradient was 0.058 N/m³; period T = 12.42 h; depth h = 20 m; vertical viscosity A_v = 0.011 m²/s; and time step Δt = 279.45 s (160 steps per cycle). The test was performed using 20 levels. The model was started with zero velocities. The water slope was applied gradually (linear ramp over 4 cycles) until a steady state was achieved. Comparison between the analytic solution and the model prediction is shown in Fig. 3. The agreement is excellent throughout the water column.

Viscosity Varying Linearly with Height

Two simulations were studied with viscosity; one increasing and one decreasing linearly from the sea bed to the sea surface. The analytic solution is presented in Prandle (1982). Simulations were performed using the same depth, grid size, period, time step, sea surface slope, and initial condition as the constant viscosity test case.

In the case of viscosity increasing linearly from the bottom (sea surface), the viscosity at the sea bed (surface) is set at A_v = 0.001 m²/s; and the viscosity at the sea surface (bed) A_v = 0.021 m²/s. The results of these simulations are in excellent agreement with the analytic solutions. The boundary layer in the linearly increasing case is (referenced from the sea bed) thinner than the constant viscosity case due to the lower viscosity near the bottom. The boundary layer for the linearly decreasing case is thicker than for the constant viscosity case and occupies the whole water column due to the fact that the vertical viscosity at the bottom is higher than in the two previous cases.

3D Testing

Lynch and Officer (1985) derived an analytic solution for the 3D flow driven by periodic forcing, with linearized bottom stress (ku_b, kv_b) and linked to the vertically averaged solution for an annular channel. The solutions were assembled from one-dimensional (1D) vertical diffusion and 2D vertically averaged solutions of the governing equations.

Consider the quarter-circle geometry with quadratically varying bathymetry $h = h_o r^2$. Note r refers to the radius of the annual channel. The sketch of geometry, bathymetry, and grid configuration are shown in Fig. 4. The viscosity is constant throughout the depth. The analytic solution, however, requires that $A_v/(\Omega h^2)$ and kh/A_v be constant, and hence A_v and k must

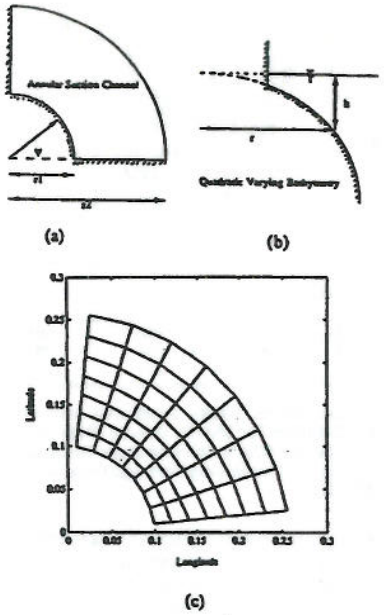

FIG. 4. Three-Dimensional Tidally Driven Model Test for: (a) Geometry; (b) Bathymetry; and (c) Grid Configuration [$r_1 = 9{,}950$ m; $r_2 = 31{,}250$ m; $h = 5\,(r/r_1)^2$]

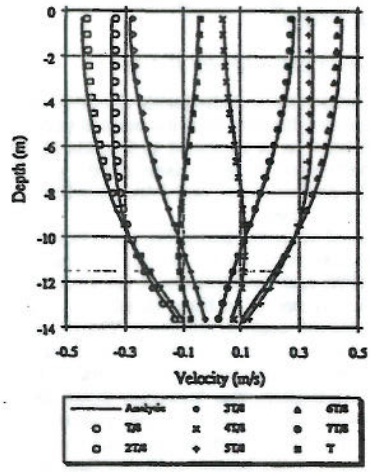

FIG. 5. Vertical Structure of Velocity at Increments of 1/8 of M_2 Tidal Period at $r = 16{,}660$ m and $\Psi = 39.4°$ for Three-Dimensional Model Test in Annular Section Channel, $r_1 = 9{,}950$ m; $r_2 = 31{,}250$ m; $A_v/(\Omega h^2) = 0.1$; $kh/A_v = 10$; $\Delta t = 558.9$ s

vary horizontally. Model tests were performed using a coarse, slightly nonorthogonal 7 × 7 grid system. The following parameters were used: inner radius $r_1 = 9{,}950$ m; outer radius $r_2 = 31{,}250$ m; $\Omega = 1.4 \times 10^{-4}\ s^{-1}$; $kh/A_v = 10$; $A_v/(\Omega h^2) = 0.1$; and $h_o = 5/r_1^2\ m^{-1}$. The open boundary was specified by varying the tidal amplitude $\zeta_o = 0.1 \cos(2\psi)$ m, where ψ = rotation angle. The model was run using eight and 20 levels in the vertical and time steps of 279.45, 558.9, and 1117.8 s.

Comparison of the model and analytical solution at point (5, 5) or at radius 16,660 m and $\psi = 39.375°$ for 20 levels with a time step of 558.9 s at one-eighth period increment is shown in Fig. 5. The agreement is very good. The largest errors (<10%) are near the surface area.

Sensitivity of the model predicted near surface currents (at 7/8, 7/4, 3/8, 7/2) to grid resolution and time step in the near surface region is shown in Table 1. The maximum errors occur at slack tide (at 7/2). The model predicted errors decrease with decreasing time step. Model errors using eight vertical levels are approximately the same as those using 20 vertical levels.

A vector plot of the velocity field at the surface at 7/4 (not presented) shows that the agreement between model predictions and analytic solution is excellent, even though the grid was relatively coarse and slightly nonorthogonal. The errors are less than 5%, except at the corner point of the inner radius $r = r_1$. Here they are about 10% due to the fact that the velocity is very small at this location. The errors become much smaller (<0.6%) at the outer radius near the open boundary. Comparison of the model-predicted velocity time series at a radius of 16,660 m, $\psi = 39.375°$, and for 0.35 m and 13.65 m below the sea surface with the analytic solution are shown in Fig. 6. The bottom velocity leads the surface velocity by 0.85 h. Predictions are again in excellent agreement with the analytic solution.

Turbulence Model Simulations

A simulation was performed in an open-closed, rectangular channel driven with tidal forcing, and a water depth of 10 m. The channel length is 51.34 km, and is represented by 20 horizontal grids. The tidal amplitude was 1.2 m, with a period of 12.42 h, $\gamma = 0.4$. A point 5.55 km from the open channel, where the pressure gradient has a magnitude that would give a current with amplitude 1.0 m/s in an inviscid calculation, was chosen to study the vertical structure of the velocity, eddy viscosity, and turbulent energy. The simulation assumed a ho-

TABLE 1. Model Prediction Errors (%) of Surface Velocity at $r = 16{,}660$ m and $\Psi = 39.4°$ for Annular Section Channel with Quadratic Bathymetry Using 8 and 20 Vertical Levels with Time Steps of 279.45, 558.9, and 1117.8 s

	8 Level			20 Level		
t (1)	279.45 s (CFL = 0.5) (2)	558.9 s (CFL = 1.0) (3)	1117.8 s (CFL = 2.0) (4)	279.45 s (CFL = 3.1) (5)	558.9 s (CFL = 6.2) (6)	1117.8 s (CFL = 12.4) (7)
7/8	4.1	4.2	4.8	3.9	4.0	4.6
7/4	3.7	3.7	4.0	3.5	3.5	3.9
3/8	3.1	3.0	3.0	3.1	3.0	3.0
7/2	8.7	10.0	12.6	7.6	8.8	11.6

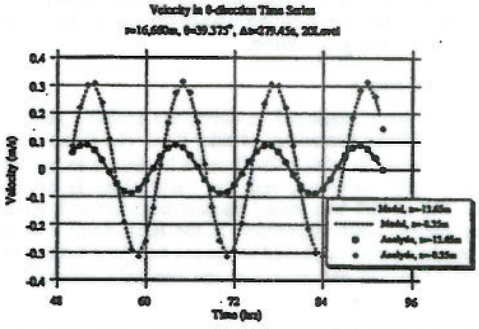

FIG. 6. Comparison of Model Predicted Velocity Time Series with Analytical Solution at $r = 16{,}660$ m and $\Psi = 39.4°$ for Three-Dimensional Model Test in Annular Section Channel Driven by M_2 Tide at Open Boundary with Varying Amplitude of $\zeta_o = 0.1 \cos(2\psi)$ m; $r_1 = 9{,}950$ m; $r_2 = 31{,}250$ m; $A_v/(\Omega h^2) = 0.1$; $kh/A_v = 10$; $\Delta t = 279.45$ s; and 20 Vertical Levels

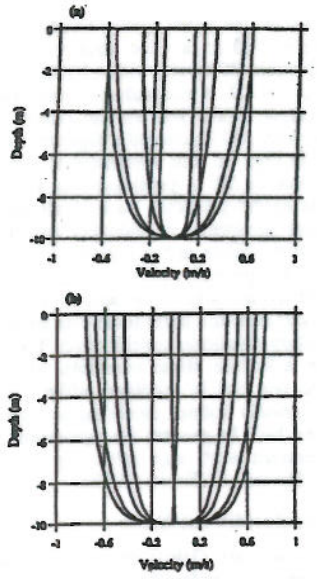

FIG. 7. Comparison of (a) Model Predicted Vertical Structure of Velocity with (b) Numerical Simulations of Davies and Jones (1990) for One-Dimensional Turbulence Model Test Driven by M_2 Tide with Imposed Pressure Gradient of 0.14 N/m^3; No-Slip Bottom Boundary Condition; $\gamma = 0.4$; $\Delta t = 558.9$ s; and 40 Vertical Levels

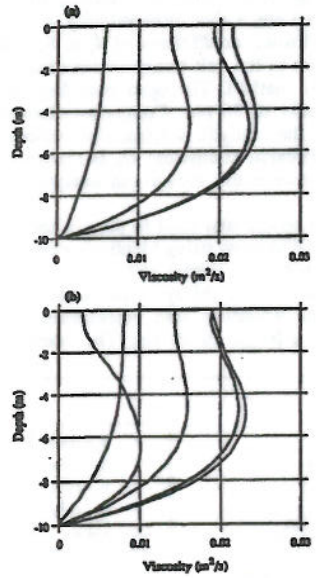

FIG. 8. Comparison of (a) Model Predicted Vertical Structure of Viscosity with (b) Numerical Simulations of Davies and Jones (1990) for One-Dimensional Turbulence Model Test Driven by M_2 Tide with Imposed Pressure Gradient of 0.14 N/m^3; No-Slip Bottom Boundary Condition; $\gamma = 0.4$; $\Delta t = 558.9$ s; and 40 Vertical Levels

mogeneous fluid. The Coriolis, baroclinic, and advective terms were neglected to compare the present results with the circulation and turbulence model developed by Davies and Jones (1990).

For a no-slip condition at the bottom boundary, simulations were conducted using 40 levels with a time step of 558.9 s. A comparison between the results of the present model (40 levels) and Davies and Jones' (1990) with 100 levels and a logarithmic transformation is shown in Figs. 7–10. Results are given at one-eighth intervals during the tidal cycle. The maximum surface velocity of the present model is about 20%

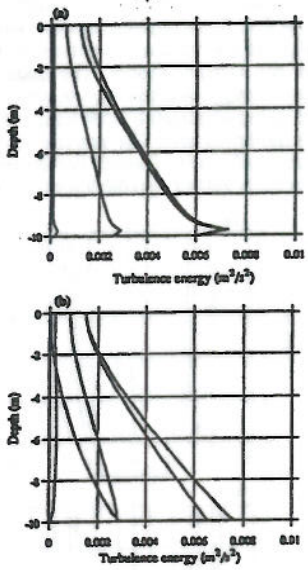

FIG. 9. Comparison of (a) Model Predicted Vertical Structure of Turbulence Energy with (b) Numerical Simulations of Davies and Jones (1990) for One-Dimensional Turbulence Model Test Driven by M_2 Tide with Imposed Pressure Gradient of 0.14 N/m^3; No-Slip Bottom Boundary Condition; $\gamma = 0.4$; $\Delta t = 558.9$ s; and 40 Vertical Levels

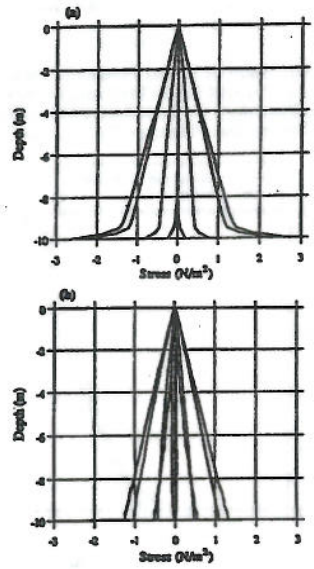

FIG. 10. Comparison of (a) Model Predicted Vertical Structure of Shear Stress with (b) Numerical Simulations of Davies and Jones (1990) for One-Dimensional Turbulence Model Test Driven by M_2 Tide with Imposed Pressure Gradient of 0.14 N/m^3; No-Slip Bottom Boundary Condition; $\gamma = 0.4$; $\Delta t = 558.9$ s; and 40 Vertical Levels

lower than their results. The structure of the eddy viscosity, turbulent energy, and shear stress are similar. However, the bottom shear stresses are twice as high in Davies and Jones (1990) than in the present simulation because the present grid structure does not provide sufficient resolution in the near-bed region. This problem is more severe at low grid resolution.

For the bottom stress specification, simulations were performed using 10 and 40 levels with a time step of 279.45 s. In these simulations the bottom drag coefficient was set at 0.0025, and $\gamma = 0.4$. A comparison between simulations using high (40 levels) and low vertical resolution (10 level) is shown in Fig. 11 for the velocity profile. The maximum viscosity, shear stress, and energy (not shown) computed using the low resolution grid are approximately 25% higher than simulations using the high resolution grid. The velocity structure (Fig. 11), however, is not significantly affected. Further tests showed that a stable and accurate velocity prediction can be obtained using

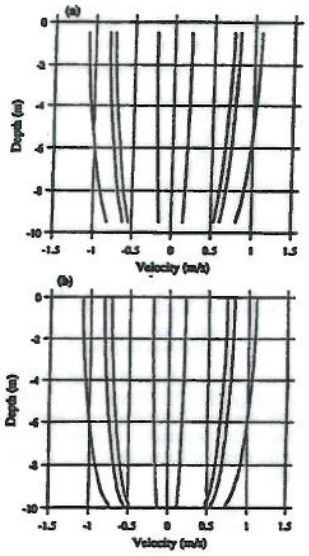

FIG. 11. Comparison of Model Predicted Vertical Structure of Velocity Using (a) 10 and (b) 40 Vertical Levels at Location 5.55 km from Open Boundary for Turbulence Model Test Driven by M_2 Tide; Bottom Stress Condition; $\gamma = 0.4$; $C_b = 0.0025$; $\Delta t = 558.9$ s

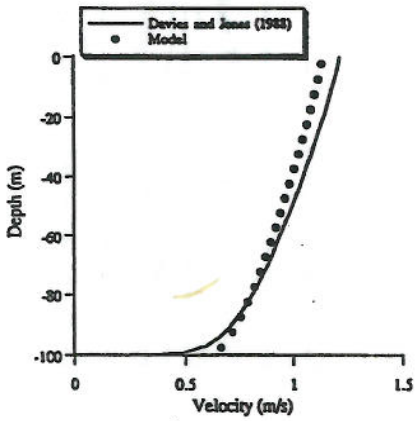

FIG. 12. Comparison of Model (Bottom Stress Condition) Predicted Vertical Structure of Velocity with Numerical Simulations of Davies and Jones (1988) Driven by Wind Stress; $\tau_s = 1.0$ N/m^2; $C_b = 0.0025$; and $\gamma = 0.2$

a time step of 1117.8 s (550 CFL, based on the diffusive time scale for 40 levels).

The model was also tested against steady wind-induced flow with a depth of 100 m, a wind stress of 1 N/m^2, a bottom stress specification; 20 levels, with a friction coefficient of, $C_b = 0.0025$, and $\gamma = 0.2$. A comparison of the velocity computed using the present model and similar results by Davies and Jones (1988) with 100 levels and a logarithmic transformation is presented in Fig. 12. The agreement is very good. A maximum difference of 5% is predicted near the surface and the sea bed. The model-predicted vertical structure of viscosity gives excellent agreement at middepth and near the surface, but slightly overpredicts at the bottom. The turbulent energy simulated by the present model is higher than Davies and Jones' (1988) model both at the surface and bottom. Differences that occur near the bottom are due to differences in the bottom boundary condition specification. The present simulations employ a bottom stress condition where the turbulent energy at the sea bed is specified while Davies and Jones (1988) use a no-slip bottom condition and specify no energy flux at the sea bed. In general the agreement is excellent although the present work uses relatively low grid resolution compared to Davies and Jones (1988).

Salinity Intrusion Simulations

Ippen and Harleman (1961) derived an analytical solution for salinity intrusion under the assumption that the salinity distribution can be represented by the equilibrium of the 1D convective-diffusion processes where the time and cross-sectionally averaged fresh water (seaward) flux of salt is balanced by the horizontal diffusive flux of salt (landward). The effect of gravitational convection by density differences (density included) is neglected. Consider a rectangular channel with a length of 105.5 km, a river flow velocity of 0.000714 m/s, and horizontal diffusion coefficients of 4, 6, 8, and 10 m^2/s. The advective term in the salt transport equation is solved by the Lax-Wendroff method. The open boundary is specified by a constant salinity of 30 ppt. Comparison between model predictions and the analytic solution for various values of the horizontal diffusion coefficient D_h is shown in Fig. 13. The agreement between the model and analytical solution is excellent.

Finally the model was used to predict the salinity intrusion in Rotterdam Waterway using identical conditions to those employed by Smith and Takhar (1981). The simulation was intended to evaluate the ability of the model to predict salinity intrusion. The waterway was represented by a rectangular channel with a length of 99 km. The width and depth were

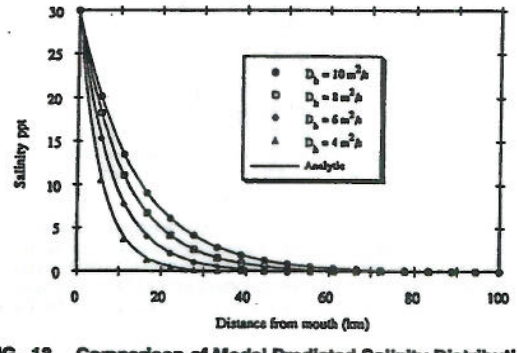

FIG. 13. Comparison of Model Predicted Salinity Distribution with Analytic Solution for One-Dimensional Salinity Intrusion Test (Transport Equation is Solved by Lax-Wendroff Method; River Flow Velocity is 0.000714 m/s; and Horizontal Diffusion Coefficients of 4, 6, 8, and 10 m^2/s Are Used)

kept constant with values of 400 and 13 m, respectively. The river inflow was 1,000 m^3/s. The model was run using 40 grids along the channel and 20 levels in the vertical. The initial conditions for velocity, elevation, and salinity were set to zero. Along the open boundary (mouth) the salinity distribution is assumed to vary from 30 ppt at the bottom to 20 ppt at the surface on inflow. The model was run with an M_2 tide. The time step was 558.9 s with a tidal amplitude at the open boundary of 0.9 m. The advective term in the salt transport equation was solved using the upwind method. The Lax-Wendroff method was not used because it required a large horizontal diffusivity (~5000 m^2/s) to maintain stability. The model was run for 66 d to achieve steady state.

A simulation was performed in which the vertical viscosity and diffusivity were calculated by the turbulence model. The bottom friction, C_b, was 0.0010. It was found that the model was very sensitive to the value of γ in the mixing length specification. Since the turbulent energy source is from the bottom boundary, the bottom drag coefficient, C_b, is also important in determining the vertical velocity structure. Fig. 14 shows the salinity distribution along the channel for $C_b = 0.0005$ and $\gamma = 0.03$ with the empirical formulation of (30), which was taken from Officer (1976), implemented to represent stratification effects. Smith and Takhar's (1981) model predictions and field observations are also shown [Fig. 14(a)]. The results show that the model-predicted high tide salinity distribution is in reasonable agreement with and an improvement over Smith and Takhar's results. Both the present and Smith and Takhar (1981) models do not accurately predict the low tide salinity distribution. As analyzed by Smith and Takhar (1981), the poor model performance for the low water salinity distribution is caused by the dock system in the waterway acting as a source and sink of salt on the ebb and flood tide, respectively.

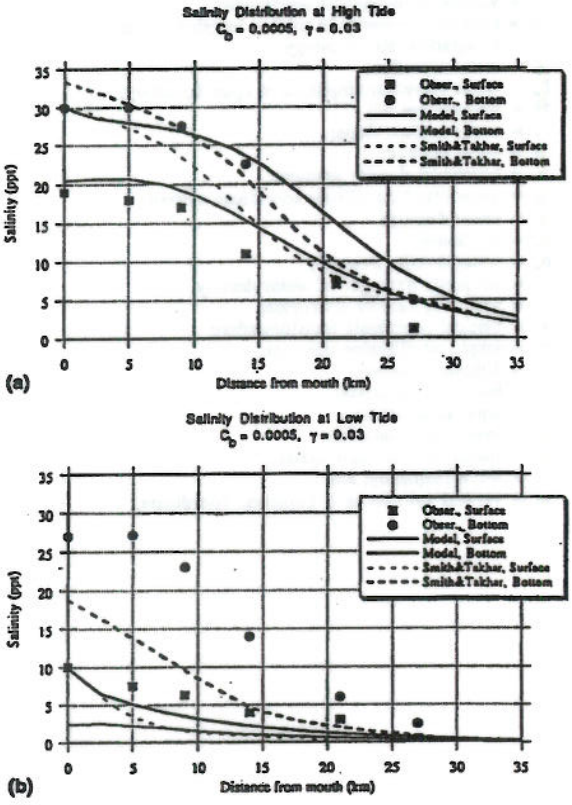

FIG. 14. Comparison of Model Predicted Salinity Distribution along Channel with Observations and Numerical Simulation of Smith and Takhar (1981) for Rotterdam Waterway at: (a) High Tide; and (b) Low Tide (Vertical Viscosity and Diffusivity Are Obtained from Turbulence Model Using Bottom Friction; C_b = 0.0005; and γ = 0.3)

CONCLUSION

A detailed description of the 3D boundary-fitted circulation model in spherical coordinates for coastal waters is presented. Both the dependent and independent horizontal variables are transformed to a boundary-fitted coordinate system. The equations are also transformed to σ-coordinates to resolve the variation in bathymetry. Both the exterior and interior mode are solved using the same time step. The numerical scheme is second order in time and space. The time step is not restricted by the shallow water gravity wave and vertical diffusion CFL criteria. The eddy viscosity/diffusivity can be specified or obtained from a one equation turbulence energy model.

A series of model tests to linear problems shows that the present model is fully capable of predicting the vertical structure of the flow in response to tidal, wind, river, and density forcing. The 3D model test in an annular section channel with quadratic bathymetry under tidal forcing has shown the model's ability to resolve a more complicated geometry and bathymetry.

The model, with a bottom stress condition, gives good predictions of the vertical structure of the velocity, shear stress, turbulence energy, and eddy viscosity even at modest vertical grid resolutions. No iteration or filtering is employed. The no-slip bottom boundary condition version of the present model fails to accurately predict the shear stress and energy distributions at the sea bed for 40 vertical levels because of the lack of vertical resolution near the sea bed.

Agreement between the model and analytic solution is excellent for the 1D salinity intrusion problem where the density gradient induced flow is neglected. The model accurately predicted the salinity distribution at high tide in the Rotterdam Waterway where the viscosity/diffusivity were obtained from a turbulence model. The poor results at low tide were probably caused by the lack of consideration of the effect of the dock system on the salinity field (Smith and Takhar 1981).

The CPU time of the internal mode with turbulence model for each water cell per computational step is 3.1×10^{-6} min on a 486/50 MHz personal computer system using a Lahey F7732 Version 5.1 Fortran compiler. The CPU time of the external mode is 2.9×10^{-6} min using the same machine and compiler.

APPENDIX I. REFERENCES

Abraham, G. (1988). "Turbulence and mixing in stratified tidal flows." *Physical processes in estuaries*, P. Dronkers and R. Leussen, eds., Springer-Verlag KG, Berlin, Germany.

ASCE Task Committee on Turbulence Models in Hydraulic Computations. (1988). "Turbulence modeling of surface water flow and transport: Part I." *J. Hydr. Engrg.*, ASCE, 114(9), 970–991.

Blackadar, A. K. (1962). "The vertical distribution of wind and turbulent exchange in a neutral atmosphere." *J. Geophys. Res.*, 67, 3095–3120.

Celik, I., and Rodi, W. (1985). "Calculation of wave-induced turbulent flows in estuaries." *Oc. Engrg.*, 12(6), 531–542.

Cheng, R. T., and Smith, P. E. (1990). "A survey of three-dimensional numerical estuarine models." *Estuarine and coastal modeling*, M. L. Spaulding, ed., ASCE, New York, N.Y., 1–15.

Davies, A. M., and Jones, J. E. (1988). "Modelling turbulence in shallow sea regions." *Small-scale turbulence and mixing in the ocean, Proc., 19 Liege Colloquium on Oc. Hydrodyn.*, J. C. Nihoul and B. M. Jamart, eds., Univ. of Liege, Liege, Belgium.

Davies, A. M., and Jones, J. E. (1990). "On the numerical solution of the turbulence energy equations for wave and tidal flows." *Int. J. for Numer. Meth. in Fluids*, 11, 1–25.

Fletcher, C. A. J. (1988). *Computational techniques for fluid dynamics, volume I, fundamental and general techniques*. Springer-Verlag New York, Inc., New York, N.Y.
Ippen, A. T., and Harleman, D. R. F. (1961). "One-dimensional analysis of salinity intrusion in estuaries." *Tech. Bull. No. 5*, Com. on Tidal Hydr., U.S. Army Corps of Engrs., Fort Belvoir, Va.
Johnson, B. H. (1980). "VAHM-A vertically averaged hydrodynamic model using boundary-fitted coordinates." *MP HL-80-3*, U.S. Army Corps of Engrs. Wtrwy. Experiment Station, Vicksburg, Miss.
Lamb, H. (1945). *Hydrodynamics*. Dover Publications, Inc., New York, N.Y.
Lynch, D. R., and Gray, W. G. (1978). "Analytic solutions for computer flow model testing." *J. Hydr. Div.*, ASCE, 104(00), 1409–1428.
Lynch, D. R., and Officer, C. B. (1985). "Analytic solutions for three-dimensional hydrodynamic model testing." *Int. J. for Numer. Meth. in Fluids*, 5, 529–543.
Lynch, D. R., and Werner, F. E. (1987). "Three-dimensional hydrodynamics on finite-element. Part I: Linearized harmonic model." *Int. J. for Numer. Meth. in Fluids*, 7, 871–909.
Mofjeld, H. O., and Lavelle, J. W. (1984). "Setting the length scale in a second-order closure model of the unstratified bottom boundary layer." *J. Phys. Oceanography*, 14, 833–839.
Muin, M. (1993). "A three-dimensional boundary-fitted circulation model in spherical coordinates," PhD dissertation, Univ. of Rhode Island, Narragansett Bay Campus, Narragansett, R.I.
Muin, M., and Spaulding, M. L. (1996). "Two-dimensional boundary-fitted circulation model in spherical coordinates." *J. Hydr. Engrg.*, ASCE, 122(9), 512–521.
Munk, W. H., and Anderson, E. R. (1948). "Notes on theory of thermocline." *J. Marine Res.*, 7, 276.
Officer, C. B. (1976). *Physical oceanography of estuaries*. John Wiley & Sons, Inc., New York, N.Y., 120.
Prandle, D. (1982). "The vertical structure of tidal currents." *Geophys. Astrophys. Fluid Dyn.*, 22, 29–49.
Sheng, Y. P. (1986). "A three-dimensional mathematical model of coastal, estuarine and lake currents using boundary-fitted grid." *Tech. Rep. No. 585*, Aeronautical Research Associates of Princeton, Princeton, N.J.
Smith, T. J., and Takhar, H. S. (1981). "A mathematical model for partially mixed estuaries using the turbulence energy equation." *Estuarine, Coast., and Shelf Sci.*, 13, 27–45.
Spaulding, M. L. (1984). "A vertically averaged circulation model using boundary-fitted coordinates." *J. Phys. Oceanography*, 14, 973–982.
Swanson, J. C. (1986). "A three-dimensional numerical model system of coastal circulation and water quality," PhD dissertation, Univ. of Rhode Island, Kingston, R.I.

APPENDIX II. NOTATION

The following symbols are used in this paper:

A_v = vertical eddy viscosity;
a = tidal wave amplitude;
b = turbulence kinetic energy;
C_μ = empirical constant in eddy viscosity relationship;
C_s = drag coefficient at surface;
C_b = drag coefficient at bottom;
C_d = empirical constant in energy dissipation relationship;
D = elevation + water depth;
D_h = horizontal eddy diffusivity;
D_v = vertical eddy diffusivity;
g = gravitation;
h = water depth;
J = Jacobian of curvilinear coordinate;
K = Von Karman constant;
k = linearized bottom friction;
L = wave length;
L_m = mixing length;
l = length of channel;
n = node number;
p = pressure;
q = concentration of substance;
R = radius of earth;
R_i = Richardson number;
S = salinity;
T = wave period;
t = time;
u_o = river flow;
U_{w_s} = friction velocity due to wind stress;
U_{w_b} = friction velocity due to bottom stress;
U, V = vertically averaged velocity in ϕ and θ direction;
U^c, V^c = vertically averaged velocity in curvilinear coordinate;
u, v, w = water velocity in ϕ, θ, r direction;
u^c, v^c = water velocity in curvilinear coordinate;
u_b = bottom velocity in ϕ direction;
v_b = bottom velocity in θ direction;
W_ϕ = wind speed in ϕ direction;
W_θ = wind speed in θ direction;
β = volumetric expansion coefficient;
γ = constant parameter in mixing length formulation;
ε = dissipation rate of energy;
ζ = water elevation;
ζ_o = water elevation amplitude at open boundary;
Θ = temperature °C;
ι = water surface slope;
κ = wave number;
Λ = horizontal density gradient;
ξ, η = generalized curvilinear coordinate system;
ρ = water density;
ρ_a = air density;
ρ_o = water density average;
$\bar{\rho}$ = vertically averaged of water density;
ρ' = vertically density difference;
σ = vertical coordinate transformation;
σ_t = empirical diffusion constant;
σ_t = Schmidt number;
τ_b = bottom shear stress;
τ_s = wind shear stress;
Φ = mean scalar quantity;
ϕ, θ, r = spherical coordinate system;
Ω = wave frequency; and
ω = vertical velocity in σ transform coordinate.

APPENDIX B: DEVELOPMENT OF AN ESTUARINE THERMAL ENVIRONMENTAL MODEL IN A BOUNDARY FITTED, CURVILINEAR COORDINATE SYSTEM (MENDELSOHN, 1998)

Development of an Estuarine Thermal Environmental Model in a Boundary-Fitted, Curvilinear Coordinate System

Daniel L. Mendelsohn
Applied Science Associates, Inc.
South Kingstown, Rhode Island 02879

INTRODUCTION

With the deregulation of the power industries in the United States there has been a rekindled interest in the development of new power generation station and the re-permitting of existing older or dormant stations. In the last two decades however increased public awareness of the possible adverse environmental effects of using 'once through cooling' in natural water bodies has led to substantial pressure on regulators as well as the utilities to study, understand and mitigate against potential degradation. Once through cooling involves the intake of water from a natural water body, (e.g. river, lake, estuary), the use of that water to cool process water, (e.g. to condense steam) and the subsequent expulsion of the now warmer water back into the environment. The incentives for this form of cooling are both efficiency and economics.

The two most prevalent and more important concerns associated with once through cooling are: 1) the potential for an unacceptable increase in temperatures in the power station effluent receiving waters; 2) the possibility that increased surface water temperatures will enhance thermal stratification of the water column resulting in a reduction of hypolimnetic reaeration. Increased temperature and reduced oxygen are both considered degredation of habitat and can cause avoidance and increased mortality to indigenous marine floral and faunal populations. For the case of an existing facility, when measurements of temperature and dissolved oxygen are made in the environment, the question is, to what extent are those measurements influenced by the thermal effluent? These are difficult concerns to address in both the scientific and the regulatory realms. Increasingly, parties involved in the decision making process have come to rely on computer modeling to address the physical, chemical and, occasionally, biological aspects of a problem, allowing regulatory and engineering decisions to be made on a solid scientific basis.

Recent improvements in computing power and observational data retrieval, storage and dissemination have made possible the development and application of a new generation of hydro-thermal models capable of addressing the concerns listed above.

THERMAL MODEL DEVELOPMENT

The development of the temperature model follows the formulation of the coupled, three-dimensional, boundary-fitted, general curvilinear coordinate, hydrodynamic and salinity transport model system for which it is to become a component. For a detailed description of the hydrodynamic model system development and testing the interested reader is referred to Muin and Spaulding, 1997 a; Mendelsohn et al. 1995 and Muin, 1993. Additional model applications can be found in Muin and Spaulding, 1997 b; Huang and Spaulding, 1995a,b; Swanson and Mendelsohn, 1996, 1993; Peene et.al. 1998.

The temperature model is designed to be integrated into and coupled with the hydrodynamic model system and use the transformed currents directly. The temperature equation must therefore be transformed as well.

Conservation of Temperature

Starting with the differential form of the conservation of energy equation, the three-dimensional conservation of temperature equation in spherical polar coordinates can be written as follows:

$$\frac{\partial T}{\partial t}+\frac{u}{r\cos\theta}\frac{\partial T}{\partial \phi}+\text{voverr}\frac{\partial T}{\partial \theta}+w\frac{\partial T}{\partial r}=\frac{Q_s}{\rho C_p V}+\frac{q_{env}}{\rho C_p \delta r}+\frac{\partial}{\partial r}(A_v)+\frac{A_h}{r^2}\left[\frac{\partial^2 T}{\cos^2\theta\partial\phi^2}+\frac{\partial^2 T}{\partial\theta^2}\right] \quad (1)$$

where,

T	= temperature, (°C)
t	= time, (s)
u	= east, φ, velocity vector component, (m/s)
v	= north, θ, velocity vector component, (m/s)
w	= vertical, r, velocity vector component, (m/s)
A_v	= vertical eddy diffusivity, (m^2/s)

A_h = horizontal eddy diffusivity, (m^2/s)
Q_s = system heat sources and sinks, (W)
q_{env} = net surface heat exchange with the environment, (W/m^2)
ρ = water density, (kg/m^3)
C_p = specific heat of water, (J/kg °C)
V = volume, (m^3)

The horizontal velocities and independent variables are next transformed to a general curvilinear coordinate system in the horizontal and at the same time the well known sigma transform, (Phillips, 1956) is applied in the vertical. The equations for the conservation of substance in a curvilinear coordinate system (ξ, η) in terms of the contravariant velocity components are as follows:

$$\frac{\partial T}{\partial t}+\frac{u^c}{r\cos\theta}\frac{\partial T}{\partial \xi}+\frac{v^c}{r}\frac{\partial T}{\partial \eta}=\frac{Q_s}{\rho \mathrm{Csubp} V}+\frac{2q_{env}}{\rho C_p D\,\delta\sigma}+\frac{4}{D^2}\frac{\partial}{\partial\sigma}\left(A_v\frac{\partial T}{\partial\sigma}\right)+$$

$$\frac{A_h}{r^2 J^2}\left[\left(\frac{\theta_\eta\theta_\eta}{\cos^2\theta}+\phi_\eta\phi_\eta\right)\frac{\partial^2 T}{\partial\xi^2}-2\left(\frac{\theta_\xi\theta_\eta}{\cos^2\theta}+\phi_\xi\phi_\xi\right)\frac{\partial^2 T}{\partial\xi\partial\eta}+\left(\frac{\theta_\xi\theta_\xi}{\cos^2\theta}+\phi\xi\phi\xi\right)\frac{\partial^2 T}{\partial\eta^2}\right] \quad (2)$$

where,
u^c = contravariant velocity component in the ξ direction
v^c = contravariant velocity component in the η direction
σ = transformed vertical coordinate
ζ = water surface elevation, (m)
D = total depth = ζ+ local depth, (m)
J = the Jacobian = $\varphi_\xi\varphi_\eta - \varphi_\eta\theta_\xi$

The relationship between the contravariant transformed velocities (u^c, v^c) and physical velocities in spherical coordinates (u,v) is given by

$$u=\cos\theta\,\phi_\xi\,u^c+\cos\theta\,\phi_\eta\,v^2$$
$$v=\theta_\xi\,u^c+\theta_\eta\,v^c \quad (3)$$

The temperature transport model (Eq. 2) is solved by a simple explicit technique except for the vertical diffusion term which is solved by a three time level, implicit scheme to ease the time step restriction due to the small vertical length scale. The advection terms are solved using either an upwind-differencing scheme which introduces minor numerical (artificial) diffusivities and is

first order accurate or the second order accurate QUICKEST formulation. Experimentation found that although the QUICKEST scheme was for the most part more conservative it was also less stable, requiring a smaller time step and consequently longer run-times than when using the 1st order upwind scheme. Horizontal gradients in temperature, (as well as in salinity, density and pressure) are evaluated along lines of constant depth to reduce the artificial numerical dispersion in the vertical associated with the sigma transform system.

The horizontal diffusion terms are solved by a centered-in-space, explicit technique. The diffusive and advective stability criteria for the numerical techniques are, $\Delta t < \Delta s^2/(2D_h)$, and $\Delta t < \Delta s/U_s$, where Δs and U_s are horizontal grid size and velocity, respectively.

Bottom Boundary Condition

The water bottom boundary condition is specified to assume that the water and bottom material are in thermal equilibrium, therefore there is no heat transfer between the water in the bottom layer and the bottom boundary. This may be written as:

$$\frac{\partial T_b}{\partial \sigma} = 0 \tag{4}$$

Surface Boundary Condition

At the water surface the temperature is influenced by a number of factors in the environment above. The most important terms in the heat transfer with the environmental can be summarized as follows:

- shortwave solar radiation
- longwave atmospheric radiation
- longwave radiation emitted from the water surface
- convection, (sensible) heat transfer between water and air
- evaporation, (latent) heat transfer between water and air

The net rate of heat transfer with the environment, q_{env} in Eq(2), including the primary forcing factors listed above can be written as:

$$q_{env} = q_{sw} - q_{swr} + q_{lw} - q_{lwr} - q_{lwb} + q_c + q_e \tag{5}$$

where,

q_{sw} = solar short wave radiation, (W/m^2)

q_{swr} = reflected solar short wave radiation, (W/m^2)
q_{lw} = atmospheric long wave radiation, (W/m^2)
q_{lwr} = reflected atmospheric long wave radiation, (W/m^2)
$q_{lw\,b}$ = long wave, (back) radiation, emitted by the water surface, (W/m^2)
q_c = convection, (sensible) heat transfer, (W/m^2)
q_e = evaporation, (latent) heat transfer, (W/m^2)

Each of the terms in the surface heat balance is described below.

Solar shortwave radiation

The solar short wave radiation is often an available, measured quantity, in which case it can be entered directly into the model as data. It can often be obtained from local airport records or from radiation model analyses for example, (DeGaetano et. al., 1993). Local measured radiation data is valued in that it contains information on both the solar radiation and the cloud cover and its influence, and is the actual radiation hitting the water surface at that date and time.

In the absence of data, solar radiation can be predicted following the method as presented by Duffie and Beckman, (1980). Starting with the clear sky radiation, G_{ctot}:

$$G_{ctot} = G_{cb} + G_{cd} \tag{6}$$

where

$$G_{cb} = G_{on}\,\tau_b \cos\theta_z \quad = \text{clear sky beam radiation} \tag{7}$$
$$G_{cd} = G_{on}\,\tau_d \cos\theta_z \quad = \text{clear sky diffuse radiation} \tag{8}$$

and the extraterrestrial, normal radiation, G_{on} is defined as

$$G_{on} = G_{sc}\,[1 + 0.33 \cos(360n / 365)] \tag{9}$$

where

G_{sc} = 1353 (W/m^2) = solar constant

The beam and diffuse atmospheric transmittance coefficients, τ_b and τ_d, respectively, can be defined as:

$$\tau_b = a_0 + a_1 e^{-k / \cos\theta z} \tag{10}$$

where

$$a_0 = r_0\, a^*_0 \quad , \; a^*_0 = 0.4237 - 0.00821\,(6 - A)^2$$
$$a_1 = r_1\, a^*_1 \quad , \; a^*_1 = 0.5055 - 0.00595\,(6.5 - A)^2$$
$$k = r_k\, k^* \quad , \; k^* = 0.2711 - 0.01858\,(2.5 - A)^2$$

and

$r_0 = 0.97$
$r_1 = 0.99$
$r_k = 1.02$
A = altitude, (km)

and the diffuse transmittance is,

$$\tau_d = 0.2710 - 0.2939\ \tau_b \quad (11)$$

The zenith angle, $\cos \theta_z$ is defined as:

$$\cos \theta_z = \cos \delta \cos \varphi \cos \omega + \sin \delta \sin \varphi \quad (12)$$

where,

φ = lattitude, (deg)
δ = declination of the sun, (deg) = $23.45 \sin [360 (284 + n) / 365]$
n = day of the year
ω = hour angle, (deg)

Finally, the hour angle, ω is calculated from the local longitude and solar time as:

$$\omega = (t_s - 12)\ 15\ ^{\circ}/hr$$

where,

t_s = solar time = standard time + 4 (L_{st} - L_{loc}) + E
L_{st} = standard meridian, (deg) (e.g. 75° W for Rhode Island)
L_{loc} = local longitude, (deg)

and E is the equation of time defined by:

$$E = 9.87 \sin 2B - 7.53 \cos B - 1.5\ B$$

where,

$$B = [\ 360 (n - 81) / 364\ ]$$

The total clear sky radiation, G_{ctot} can then be corrected for cloud cover effects with the use of a clearness index, K_T. This value can be defined on an monthly, daily or hourly basis dependent on available data and use and is often available with meteorological data when measured radiation data is not. The clearness index is the ratio of the average radiation on an horizontal surface to the average extraterrestrial radiation at the same latitude and longitude;

$$K_t = \frac{\overline{G}}{G_{on}} \tag{13}$$

The value $\overline{G}$ would then be used in place of G_{on} in equations (7) and (8) to create G_{tot}.

Finally, the net solar shortwave radiation, q_{net} , absorbed through the water surface, can be calculated as;

$$q_{net} = q_{sw} - q_{swr} = \alpha_w (1 - albedo_w) G_{tot} \tag{14}$$

where,

α_w = water absorptivity, (-) $\cong$ 0.97
$albedo_w$ = albedo of the water surface (-), (see below)

Reflected solar short wave radiation

The reflected solar short wave radiation, as included in Equation (14), and can defined as;

$$q_{swr} = albedo_w G_{tot} \tag{15}$$

where the albedo is a measure of the reflective property of the material surface, (water in this case) and can be defined as:

$albedo_w$ = reflected energy / incident energy

Values for the albedo for water are both a function of wave state and strongly of solar altitude, Stull, (1988). They can range from 0.03 when the sun is overhead to near 1.0 at low elevation angles. Stull, (1988) gives an equation for calculating the albedo for varying solar altitudes, (azimuth angle):

$$albedo_w = -0.0139 + 0.0467 \tan\theta_z \tag{16}$$

Atmospheric long wave radiation

In addition to the short wave radiation, the atmosphere and the water surface are also exchanging long wave radiation. The atmospheric long wave radiation is a function of the air temperature and water vapor content and may be calculated from an effective sky temperature, (Duffie & Bechman, 1980). From the Stephan-Bolzmann law long wave radiation to the water surface is

then:

$$q_{lw} = \sigma_{sb} T_{sky}^4 \quad (17)$$

where,

σ_{sb} = Stephan-Bolzmann constant, (5.669×10^{-8} W / $m^2 K^4$)
T_{sky} = effective sky temperature, (K)

Duffie and Beckman suggest that the sky temperature be calculated from an empirical relationship, (Bliss, 1961) as:

$$T_{sky} = [0.8 + \frac{(T_{dp} - 273)}{250}]^{\frac{1}{4}} \quad (18)$$

where

T_{dp} = dew point temperature, (C).

Thomann and Mueller suggest an alternate formulation:

$$q_{lw} = \sigma_{sb} T_{ak}^4 (A + 0.031\sqrt{e_a}) \quad (19)$$

where

T_{ak} = air temperature, (K)
e_a = vapor pressure at air temperature, T_a (mm Hg)
= (relative humidity fraction) x (e_{sat} @ T_a)
e_{sat} = saturation vapor pressure (mm Hg)
T_a = air temperature, (C)
A = coefficient to account for air temperature and clearness index, with a range of 0.5 - 0.7.

The saturation vapor pressure can be calculated from the air temperature (T_a) using the following equation, (List, 1951):

$$e_{sat} = 4.58123 \times 10^{[7.5 T_a / T_{ak}]} \quad (20)$$

Results for the two long wave radiation formulations only vary slightly for a given set of conditions with Equation (19) consistently giving a larger value, by approximately 3%, than (17). No independent confirmation for either formulation has been given to date.

Reflected atmospheric long wave radiation

The reflected long wave radiation over a water body is generally small, about 3% of the incoming long wave, (Thomann & Mueller, 1987) and can be calculated as:

$$q_{lwr} = (1 - \varepsilon_w) q_{lw} \quad (21)$$

where

ε_w = emissivity of water $\cong 0.97$

Long wave radiation, emitted by the water surface

The water surface also emits long wave radiation at a rate proportional to the surface temperature in Kelvins:

$$q_{lw} = \varepsilon_w \sigma_{sb} T_{wk}^4 \quad (22)$$

where

T_{wk} = water surface temperature, (K)

Convection heat transfer

The rate of convective heat transfer between the water surface and the air depends on the temperature difference between the two and is suggested to be proportional to the square of the wind speed, (Thomann and Mueller, 1987; Edinger et. al. 1974). This can be written as,

$$q_c = c_1 (19.0 + 0.95 U_w^2) (T_a - T_w) \quad (23)$$

where

T_w = water surface temperature, (C)
c_1 = Bowen's coefficient = 0.47 mm Hg / °C

Evaporation heat transfer

Similar to the rate of convective heat transfer the evaporative heat transfer between the water and the air can be thought of as depending on the difference between the vapor pressures of the two and is also suggested to be proportional to the square of the wind speed, (Thomann and Mueller, 1987; Edinger et. al. 1974). This can be written as,

$$q_c = (19.0 + 0.95 U_w^2) (e_a - e_w) \quad (24)$$

where

e_w = vapor pressure at water surface temperature, T_w (mm Hg)

REFERENCES

DeGaetano, Arthur T., Keith L. Eggleston and Warren W. Knapp, 1993. Daily Solar Radiation Estimates for the Northeast United States. Northeast Regional Climate Center Research Series, Publication No. RR93-4, May 1993.

Duffie, John A. and William Beckamn, 1980. Solar Engineering of Thermal Processes. John Wiley and Sons, New York.

Edinger, J.E., D.K.Brady and J.C. Geyer, 1974. Heat Exchange and Transport in the Environment. Report No. 14, Electric Power Res. Inst. Pub. No. EA-74-049-00-3, Palo Alto, Ca, Nov. 1974, 125pp.

Huang, W. and M.L. Spaulding, 1995a. Modeling of CSO-induced pollutant transport in Mt. Hope Bay. ASCE J. of Environmental Engineering, Vol. 121, No. 7, July, 1995, 492-498.

Huang, W. and M.L. Spaulding, 1995b. A three dimensional numerical model of estuarine circulation and water quality induced by surface discharges. ASCE Journal of Hydraulic Engineering, 121:(4) April 1995, p. 300-311.

List, R.J. 1951/1984. Smithsonian Meteorological Tables. Smithsonian Institution Press, Washington DC.

Mendelsohn, D.L., E. Howlett and J.C. Swanson, 1995. WQMAP in a Windows Environment. published in proceedings of: 4th International Conference on Estuarine and Coastal Modeling, ASCE, San Diego, October 26-28, 1995.

Muin, M. and M.L. Spaulding, 1997a. A 3-D boundary-fitted circulation model. Journal of Hydraulic Engineering, Vol. 123, No. 1.

Muin, M., M.L. Spaulding, 1997b. Application of Three-Dimensional Boundary-Fitted Circulation Model To Providence River, published in: Journal of Hydraulic Engineering, Vol. 123, No. 1.

Muin, M., 1993. A Three-Dimensional Boundary-Fitted Circulation Model in Spherical Coordinates, Ph.D. Dissertation, Univ. of Rhode Island, Narragansett Bay Campus, Narragansett, RI.

Peene, S., E. Yassuda and D. Mendelsohn, 1998. Development of a Waste Load Allocation Model within Charleston HarborEstuary. Phase I: Barotropic Circulation. published in proceedings of: 5th International Conference on Estuarine and Coastal Modeling. Ed Malcolm L. Spaulding and Alan F. Blumberg. ASCE, Alexandria, Virginia, October 22-24,1997.

Phillips, Norman, 1956. Monthly Weather Review, AGU.

Stull, Roland B., 1988. An Introduction to Boundary Layer Meteorology. Kluwer Academic Publishers, P.O. Box 17, 3300 AA Dordrecht, The Netherlands.

Swanson, J. C. and D. Mendelsohn, 1996. Water Quality Impacts of Dredging and Disposal Operations in Boston Harbor. presented at: ASCE North American Water and Environmental Congress '96 (NAWEC '96), Anaheim, CA, 22-28 June 1996.

Swanson, J.C., D. Mendelsohn, 1993. Application of WQMAP to upper Narragansett Bay, Rhode Island. Estuarine and Coastal Modeling III. Proceedings of the 3rd International Conference, sponsored by the Waterway, Port, Coastal and Ocean Division of the ASCE, Oak Brook, IL, September 8-10, 1993.

Thomann and Mueller, 1987. Principles of Surface Water Quality Modeling and Control. Harper and Row, Publishers Inc., New York, N.Y.